A new ray-tracing scheme for radiation hydrodynamic simulations on highly parallel architectures

A new ray-tracing scheme for radiation hydrodynamic simulations on highly parallel architectures

Satoshi TANAKA
Doctoral Program in Physics

Submitted to the Graduate School of
Pure and Applied Sciences
in Partial Fulfillment of the Requirements
for the Degree of Doctor of Philosophy in
Physics

at the
University of Tsukuba

Graduate School of Pure and Applied Sciences

A new ray-tracing scheme for radiation hydrodynamic simulations on highly parallel architectures

(並列プロセッサに最適化されたレイトレーシング法による輻射流体シミュレーション)

Satoshi TANAKA

Doctoral Program in Physics
Student ID 201230077
Doctor of Philosophy in Physics
Advised by Masayuki Umemura

ABSTRACT

The radiation transfer (RT) is one of the important physical processes for the formations of astrophysical objects such as stars and galaxies, and the reionization in the early universe. However, it had not been incorporated into numerical simulations of such phenomena in a self-consistent manner due to its huge computational cost compared with other physical processes such as gravitational interaction and hydrodynamics. This why the RT had been numerically computed only in a static fluid or snapshots of hydrodynamical simulations in a post-process manner until recently. Rapid increase of available computational power enables us to conduct radiation hydrodynamical simulations, in which hydrodynamical equations are numerically solved in conjunction with the calculations of the RT.

Recent radiation hydrodynamical simulations can handle the transfer of radiation from point sources such as stars in a galaxy and galaxies in the large-scale structure in the universe. On the other hand, the numerical computation of the transfer of radiation emitted by diffuse medium, or the diffuse radiation, is more computationally expensive and has been ignored or only considered in a post-process manner. Thus, in the transfer of ionizing photons in hydrogen medium, for example, one usually adopt the on-the-spot approximation, in which the recombination photons emitted in ionized regions are absorbed in the very vicinity, and hence the transfer of such recombination photons can be neglected. This approximation is justified when the mean free path of the recombination photons is much shorter than the system size. Actually, this condition is not always satisfied in the formations of stars and galaxies. Therefore, we have to consider the transfer of recombination photons to precisely simulate the formations of these objects.

In this thesis, we develop a three-dimensional ray-tracing scheme, ART (Authentic Radiation Transfer) to solve the transfer of diffuse radiation so efficiently that it can be coupled with hydrodynamical simulations. The performance of modern processors is improved by increasing the numberof processing elements or CPU cores integrated on a single processor chip rather than improving the performance of individual processing elements. Therfore, our scheme is designed so that it can achieve good computational performance on processors with such a highly parallel architecture, such as multi-core CPUs and graphics

processing units (GPUs). Specifically, we implement our scheme using `OpenMP` application programming interface for multi-core CPUs and `CUDA` programming platform for GPUs produced by NVIDIA. The performance of our implementation is proportional to the number of CPU cores and GPU boards indicating that it has a good scalability on processors with a highly parallel architecture. It should be noted that the performance on four GPU boards (Tesla M2090) is nearly 10 times better than that on two sockets of Intel Xeon E5-2670 with 8 cores. Furthermore, our scheme to solve the transfer of diffuse radiation is successfully parallelized on a multi-node system by adopting the multiple wave front (MWF) scheme with a reasonable parallel efficiency. This suggests our current implementation of diffuse RT works well on a massively parallel system with highly parallel processors in near future.

Along with the implementation of the ART scheme of diffuse radiation transfer on highly parallel processors, we also implement the efficient RT scheme, ARGOT (Accelerated Radiative Transfer on Grids using Oct-Tree) for the radiation from point sources by Okamoto et al. (2012), which is capable of computing the RT from many point sources quite efficiently by grouping distant raditating point sources into a single bright sources using tree strutures of point sources, and computational cost is proportional to $\log N_{\rm s}$ rather than $N_{\rm s}$, where $N_{\rm s}$ is the number of point sources. With these two RT schemes in combination, we can solve the RT from point sources and spatially extended medium simultaneously and in the case of RT of ionizing photons, one can compute the ionization state photo-heating of gaseous medium without the on-the-spot approximation. Furthermore, we couple these two RT scheme with hydrodynamics shceme to conduct radiation hydrodynamics simulations.

Using the radiation hydrodynamics code we developed, we carried out several test simulations desribed in Iliev et al. (2006) and Iliev et al. (2009) to verify the validity of our code. We also conduct the same test simulations with and without on-the-spot approximation to see the effect of recombination radiation emitted in the ionized regions. It is found that recombination radiation makes an important contribution to the time evolution of ionization and thermal states of irradiated gas in some test simulations.

This thesis is based on Tanaka, Yoshikawa, Okamoto & Hasegawa (submitted to Publications of the Astronomical Society of Japan).

Contents

Chapter 1

Introduction

Radiation transfer (RT) has been long recognized as a indispensable ingredient in numerically simulating many astrophysical phenomena including the reionization of intergalactic medium (IGM) in the early universe, radiative feedback in the galaxy formation, and others. However, it is very recent that we have become able to properly compute the RT and couple it with hydrodynamics in three dimensional numerical simulations of these phenomena, mostly because the computational cost of RT is quite demanding. So far, varieties of numerical schemes for solving the RT in three dimensions are proposed during the last two decades (Iliev et al., 2006), and some of them can be coupled with the hydrodynamic simulations (Iliev et al., 2009) thanks to not only the increase of the available computational resources, but also the improvement of numerical algorithms to solve the RT in many astrophysical conditions.

Most of the numerical schemes for the RT can be divided into two groups: one is the moment-based schemes which solve the moment equation of the RT equation instead of solving the RT equation directly, and the other is the ray-tracing schemes. As for the moment-based schemes, the important advantage is that the computational costs scale with the number of mesh grids, $N_{\rm m}$ and hence can be easily coupled with hydrodynamic simulations. The flux-limited diffusion scheme, which adopts the closure relation valid in the diffusion limit, is the most common among the moment-based schemes, while there are a number of more sophisticated schemes which close the moment equations with the optically thin variable Eddington tensor approximation (Gnedin & Abel, 2001) and the locally evaluated Eddington tensor (González et al., 2007). The accuracy and validity of the moment-based schemes are, however, problem-dependent. Therefore, the ray-tracing schemes are naturally chosen for solving the RT in general situations.

In ray-tracing schemes, emission and absorption of radiation are followed along the light-rays that extend through the computational domain. As for the long-characteristics schemes (Abel et al., 1999; Sokasian et al., 2001) in which light-rays between all radiation sources and all other relevant meshes are considered, the computational cost scales with $N_{\rm m}^2$ in general cases and $N_{\rm m}^{4/3}N_{\rm s}$ when we consider only the RT from point radiating sources, where $N_{\rm s}$ is the number of point sources. On the other hand, for the short-characteristics schemes (Kunasz & Auer, 1988; Stone et al., 1992) which are similar to the long-characteristics schemes but integrate the RT equation only along paths connecting nearby mesh grids, the computational cost scales with $N_{\rm m}^{5/3}$ in general and $N_{\rm m}N_{\rm s}$ for the RT from point sources. Ray-tracing schemes are in principle versatile for any physical settings but computationally more expensive than the moment-based schemes.

Some of the ray-tracing schemes are coupled with hydrodynamical simulations adopting smoothed

particle hydrodynamics (SPH) codes (Susa, 2006; Hasegawa & Umemura, 2010; Pawlik & Schaye, 2011) and mesh-based codes (Rijkhorst et al., 2006; Wise & Abel, 2011), and they can handle the RT and its hydrodynamical feedback in a self-consistent manner. Majority of these radiation hydrodynamics codes, however, consider the transfer of radiation only from point sources and ignore the effect of radiation transfer from spatially extended diffuse sources, such as the recombination radiation emitted from ionized regions and infrared radiation emitted by dust grains, since the computational costs for computing the transfer of diffuse radiation is prohibitively large.

Specifically, in the numerical RT calculations of the hydrogen ionizing radiation, we usually adopt the on-the-spot approximation in which one assumes that the ionizing photons emitted by radiative recombinations in ionized regions are absorbed by neutral atoms in the immediate vicinity of the recombining atoms. However, adopting the on-the-spot approximation can fail to notice the important effects of diffuse recombination radiation in some situations. The roles of ionizing recombination photons in the epoch of cosmic reionization is discussed by a number of works (Ciardi et al., 2001; Miralda-Escudé, 2003; Dopita et al., 2011; Rahmati et al., 2013a). Dopita et al. (2011) proposed the recombination photons produced in the fast accretion shocks in the structure formation in the universe as an possible source of ionizing photons responsible for the cosmic reionization, though Wyithe et al. (2011) showed that its impact on the cosmic reionization is not very significant. It is also reported that the recombination radiation plays an important role at transition regions between highly ionized and self-shielded regions (Rahmati et al., 2013a). As for the effect of recombination photons on the galaxy-size scales, Inoue (2010) showed that the recombination radiation produces the Lyman-'bump' feature in the spectral energy distributions of high-z galaxies, and also that the escaping ionizing photons from high-z galaxies are to some extent contributed by the recombination radiation. Rahmati et al. (2013b) also pointed out that the recombination radiation makes the major contribution to the photo-ionization at regions where the gas is self-shielded from the UV background radiation.

The RT of infrared diffuse radiation emitted by dust grains plays an important roles in the evolution of star-forming galaxies, in which the radiation pressure exerted by multi-scattered infrared photons drives stellar winds. In most of numerical simulations of galaxy formation, however, such momentum transfer is treated only in a phenomenological manner (e.g. Okamoto et al. 2014).

In this thesis, we present a new ray-tracing scheme to solve the RT of diffuse radiation from spatially extended radiating sources efficiently on processors with highly parallel architectures such as graphics processing units (GPUs) and multi-core CPUs which are recently popular or available in near future. The basic idea of the scheme is based on the scheme presented by Razoumov & Cardall (2005) and 'authentic RT' (ART) scheme in Iliev et al. (2006). Generally speaking, development of such numerical schemes with high concurrency is of critical importance because the performance improvement of recent processors are achieved by the increase of the number of processing elements or CPU cores integrated on a single processor chip rather than the improvement of the performance of individual processing elements.

The rest of the these is organized as follows. Chapter 2 is devoted to describe the numerical scheme to simulate the radiation transfer. Chapter 3 is described the hydrodynamics scheme and coupling radiation transfer and hydrodynamics. In Chapter 4, we present our implementation of the scheme suitable to highly parallel architectures such as GPUs and CPUs with multi-core architectures. We present the results of numerical test suits of RT of diffuse radiation in Chapter 5. The computational performance of

our implementation is shown in Chapter 6.

Chapter 2

Ray-Tracing Schemes for Radiation Transfer

In this chapter, we describe ray-tracing schemes for radiation transfer adopted in thies thesis. Generally, radiation field can be decomposed into two components. One is the direct incident radiation from point radiation sources, and the other is the diffuse radiation emerged from spatially extended regions. In our implementation, the RT of photons emitted by point radiation sources is computed separately from that of diffuse radiation. Throughout in this thesis, we consider the RT of hydrogen ionizing photons emitted by point radiation sources, and recombination photons emerged from the ionized regions as the diffuse radiation.

2.1 Radiation Transfer Equation

Photons emitted by point sources or spatially extend regions travel in the ambient gaseous medium subject to the influence of absorption and emission. We use the steady state RT equation for a given frequency ν:

$$\frac{dI_\nu}{d\tau_\nu} = -I_\nu + \mathcal{S}_\nu, \tag{2.1}$$

where I_ν, τ_ν and $\mathcal{S}_\nu$ are the specific intensity, the optical depth and the source function, respectively. The source function is given by $\mathcal{S}_\nu = \varepsilon_\nu/\kappa_\nu$, where κ_ν and ε_ν are the absorption and emission coefficients, respectively. The optical depth is defined by the path length of photon s and κ_ν,

$$\tau_\nu = \int_0^s \kappa_\nu ds'. \tag{2.2}$$

where s' is the path length at a position along the ray. The formal solution of equation equation (2.1) is given by

$$I_\nu(\tau_\nu) = I_\nu(0)\, e^{-\tau_\nu} + \int_0^{\tau_\nu} \mathcal{S}_\nu(\tau'_\nu) e^{-(\tau_\nu - \tau'_\nu)} d\tau'_\nu, \tag{2.3}$$

where τ'_ν is the optical depth at a position along the ray. When we adopt the "on-the-spot" approximation in which recombination photons emitted in ionized regions are assumed to be absorbed where they are emitted, we neglect the source function, $\mathcal{S}_\nu$, and the formal solution is simply reduced to

$$I_\nu(\tau_\nu) = I_\nu(0)\, e^{-\tau_\nu}. \tag{2.4}$$

In this formulation, we consider only the absorption process in the gaseous medium.

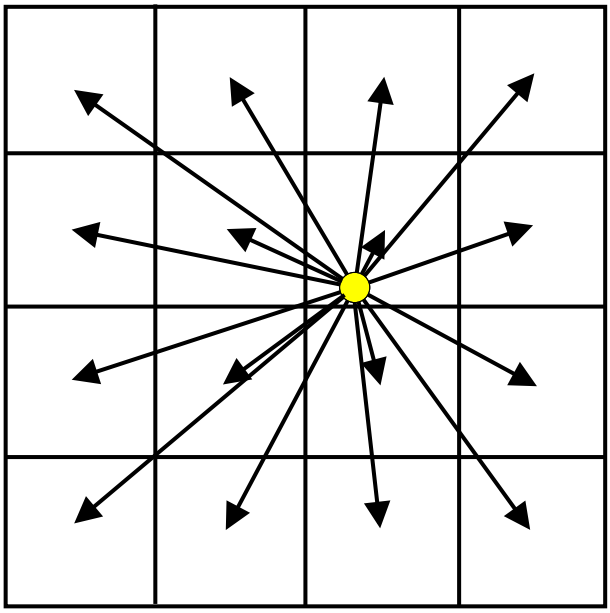

Figure 2.1: Schematic illustration of the ray-tracing method for the radiation emitted by a point radiation source in the two-dimensional mesh grids.

2.2 RT from point radiation sources

To solve the RT from point radiation sources, we compute the optical depth between each pair of a point radiation source and a target mesh grid, i.e. an end point of each light-ray (see Figure 2.1). Instead of solving equation (2.4), we compute the radiation flux density at the target mesh grid as

$$f_\alpha(\nu) = \frac{L_\alpha(\nu)}{4\pi r_\alpha^2} \exp\left[-\tau_\alpha(\nu)\right], \tag{2.5}$$

where $L_\alpha(\nu)$ is the intrinsic luminosity of the α-th point radiation source, and r_α and $\tau_\alpha(\nu)$ are the distance and the optical depth between the point radiation source and the target mesh grid, respectively. Then, the photo-ionization and photo-heating rates of the i-th species contributed by the α-th point radiation source are computed by

$$\Gamma_{i,\gamma}^\alpha = \int_{\nu_i}^\infty \frac{f_\alpha(\nu)}{h\nu}\sigma_i(\nu)\, d\nu, \tag{2.6}$$

and

$$\mathcal{H}_{i,\gamma}^\alpha = \int_{\nu_i}^\infty \frac{f_\alpha(\nu)}{h\nu}(h\nu - h\nu_i)\sigma_i(\nu)\, d\nu \tag{2.7}$$

respectively, where $\sigma_i(\nu)$ and ν_i is the ionization cross section and the threshold frequency of the i-th species.

For a single point radiation source, the number of rays to be calculated is N_m, and the number of mesh grids traveled by a single light-ray is in the order of $N_\mathrm{m}^{1/3}$. Thus, the computational cost for a single point radiation source is proportional to $N_\mathrm{m}^{4/3}$. Therefore, the total computational cost scales as $N_\mathrm{m}^{4/3}N_\mathrm{s}$, where N_s is the number of point radiation sources. For a large number of point radiation sources, we can reduce the computational costs by using more sophisticated schemes such as the ARGOT scheme (Okamoto et al., 2012) in which a distant group of point radiation sources is treated as a bright point

source located at the luminosity center with a luminosity summed up for all the sources in the group to effectively decrease the number of radiation sources. In ARGOT scheme, we contruct a oct-tree structure of all the point radiation sources and if an angular size of a group of point sources seen from a target mesh is smaller than a critical value $\theta_{\rm cirt}$, the group is treated as a single point radiating source. Therefore the computational cost is proportional to $\log N_{\rm s}$ rather than $N_{\rm s}$.

2.3 RT of the diffuse radiation

We solve the equation (2.3) to compute the RT of the diffuse radiation. The numerical scheme we adopt in this thesis is based on the method developed by Razoumov & Cardall (2005) and 'authentic RT' (ART) by Nakamoto et al. presented in Iliev et al. (2006), which is as accurate as the long characteristics methods though its computational cost is proportional to $N_{\rm m}^{5/3}$ similarly to that of the short characteristic method. In this scheme, we solve the equation (2.3) along equally spaced parallel rays as schematically shown in Figure 2.2.

For a given incoming radiation intensity $I_\nu^{\rm in}$ along a direction $\hat{\mathbf{n}}$, the outgoing radiation intensity $I_\nu^{\rm out}$ after getting through a path length ΔL of a single mesh is computed by integrating equation (2.3) as

$$I_\nu^{\rm out}(\hat{\mathbf{n}}) = I_\nu^{\rm in}(\hat{\mathbf{n}})\, e^{-\Delta\tau_\nu} + \mathcal{S}_\nu(1 - e^{-\Delta\tau_\nu}), \tag{2.8}$$

where $\Delta\tau_\nu$ is the optical depth of the path length ΔL (i.e. $\Delta\tau_\nu = \kappa_\nu \Delta L$), and $\mathcal{S}_\nu$ and κ_ν are the source function and the absorption coefficient of the mesh grid, respectively. $\mathcal{S}_\nu$ is assumed to be a constant between this path length.

The intensity of the incoming radiation averaged over the path length ΔL across a single mesh grid can be calculated as

$$\bar{I}_\nu^{\rm in}(\hat{\mathbf{n}}) = \frac{1}{\Delta L}\int_0^{\Delta L} I_\nu^{\rm in}(\hat{\mathbf{n}}) e^{-\kappa_\nu l}\, dl = I_\nu^{\rm in}(\hat{\mathbf{n}})\frac{1 - e^{-\Delta\tau_\nu}}{\Delta\tau_\nu}. \tag{2.9}$$

In addition to this, we have a contribution to the radiation intensity from the source function which we set constant in each mesh grid, and the total intensity averaged over the path length is given by

$$\bar{I}_\nu(\hat{\mathbf{n}}) = \bar{I}_\nu^{\rm in}(\hat{\mathbf{n}}) + \mathcal{S}_\nu = I_\nu^{\rm in}(\hat{\mathbf{n}}_i)\frac{1 - e^{-\Delta\tau_\nu}}{\Delta\tau_\nu} + \mathcal{S}_\nu \tag{2.10}$$

For those mesh grids through which multiple parallel light-rays pass, the averaged intensity can be given by

$$\bar{I}_\nu^{\rm ave}(\hat{\mathbf{n}}) = \frac{\sum_j \Delta\tau_{\nu,j}\bar{I}_{\nu,j}(\hat{\mathbf{n}})}{\sum_j \Delta\tau_{\nu,j}} = \bar{I}_\nu^{\rm ave,in}(\hat{\mathbf{n}}) + \mathcal{S}_\nu, \tag{2.11}$$

where $\bar{I}_{\nu,i}$ and $\Delta\tau_{\nu,i}$ are the intensity averaged over the i-th light-ray and the optical depth of i-th light-ray in the mesh grids, respectively, $\bar{I}_\nu^{\rm ave,in}$ is a contribution from the incoming radiation given by

$$\bar{I}_\nu^{\rm ave,in}(\hat{\mathbf{n}}) = \frac{\sum_j \Delta\tau_{\nu,j}\bar{I}_{\nu,j}^{\rm in}(\hat{\mathbf{n}})}{\sum_j \Delta\tau_{\nu,j}}, \tag{2.12}$$

and the summation is over all the parallel light-rays in the same mesh grid. Then, the mean intensity can be computed by averaging $\bar{I}_\nu^{\rm ave}$ described above over all the directions as,

$$J_\nu = \frac{1}{N_{\rm d}}\sum_{i=1}^{N_{\rm d}} \bar{I}_\nu^{\rm ave}(\hat{\mathbf{n}}_i) = J_\nu^{\rm in} + \mathcal{S}_\nu, \tag{2.13}$$

where $\hat{\mathbf{n}}_i$ describes a vector toward the i-th direction and N_d is the number of directions of light-rays to be considered, $\bar{I}_\nu^\mathrm{ave}(\hat{\mathbf{n}}_i)$ is the averaged intensity along the i-th direction calculated with equation (2.11), and J_ν^in is given by

$$J_\nu^\mathrm{in} = \frac{1}{N_\mathrm{d}} \sum_{i=1}^{N_\mathrm{d}} \bar{I}_\nu^\mathrm{ave,in}(\hat{\mathbf{n}}_i). \tag{2.14}$$

Then, the photo-ionization and photo-heating rates of the i-th species contributed by the diffuse radiation in each mesh grid can be computed as

$$\Gamma_{i,\gamma}^\mathrm{diff} = 4\pi \int_{\nu_i}^{\infty} \frac{J_\nu}{h\nu} \sigma_i(\nu)\, d\nu \tag{2.15}$$

and

$$\mathcal{H}_i^\mathrm{diff} = 4\pi \int_{\nu_i}^{\infty} \frac{J_\nu}{h\nu} (h\nu - h\nu_i) \sigma_i(\nu)\, d\nu \tag{2.16}$$

As for the recombination radiation of ionized hydrogen (HII) regions, the number of recombination photons to the ground state per unit time per unit volume, $\dot{N}^\mathrm{rec}$, can be expressed in terms of the emissivity coefficient ε_ν as

$$\dot{N}^\mathrm{rec} = 4\pi \int_{\nu_i}^{\nu_i+\Delta\nu} \frac{\varepsilon_\nu}{h\nu}\, d\nu = [\alpha_\mathrm{A}(T) - \alpha_\mathrm{B}(T)] n_\mathrm{e} n_\mathrm{HII}, \tag{2.17}$$

where $\alpha_\mathrm{A}(T)$ and $\alpha_\mathrm{B}(T)$ are the recombination rates of HII as functions of temperature T in the case-A and case-B approximations, respectively, and n_e and n_HII are the number densities of the electrons and HII, respectively. $\Delta\nu$ is the frequency width of the spectra of the recombination radiation estimated with the temperature of the gas, T as $\Delta\nu = k_\mathrm{B}T/h$. In this work, we adopt the rectangular functional form of $\varepsilon_\nu/(h\nu)$ as

$$\frac{\varepsilon_\nu}{h\nu} = \begin{cases} \dfrac{\Delta\alpha(T) n_\mathrm{e} n_\mathrm{HII}}{4\pi\Delta\nu} & (\nu_0 \le \nu \le \nu_0 + \Delta\nu) \\ 0 & (\text{otherwise}), \end{cases} \tag{2.18}$$

where $\Delta\alpha(T) = \alpha_\mathrm{A}(T) - \alpha_\mathrm{B}(T)$. Thus, the source function is given by

$$\mathcal{S}_\nu = \frac{\varepsilon_\nu}{\kappa_\nu} = \begin{cases} \dfrac{\Delta\alpha(T) n_\mathrm{e} n_\mathrm{HII} h\nu}{4\pi n_\mathrm{HI} \sigma_\mathrm{HI}(\nu)\Delta\nu} & (\nu_0 \le \nu \le \nu_0 + \Delta\nu) \\ 0 & (\text{otherwise}). \end{cases} \tag{2.19}$$

Therefore, the photo-ionization and photo-heating rates of neutral hydrogen can be rewritten as

$$\Gamma_{\mathrm{HI},\gamma}^\mathrm{diff} = 4\pi \int_{\nu_0}^{\nu_0+\Delta\nu} \frac{J_\nu^\mathrm{in}}{h\nu} \sigma_\mathrm{HI}(\nu) d\nu + \frac{\Delta\alpha(T) n_\mathrm{e} n_\mathrm{HII}}{n_\mathrm{HI}}, \tag{2.20}$$

and

$$\mathcal{H}_{\mathrm{HI},\gamma}^\mathrm{diff} = 4\pi \int_{\nu_0}^{\nu_0+\Delta\nu} \frac{J_\nu^\mathrm{in}}{\nu} (\nu - \nu_0)\, \sigma_\mathrm{HI}(\nu)\, d\nu + \frac{\Delta\alpha(T) n_\mathrm{e} n_\mathrm{HII}}{2 n_\mathrm{HI}} h\Delta\nu, \tag{2.21}$$

respectively.

The number of light-rays to be computed along a specific direction is proportional to $N_\mathrm{m}^{2/3}$, and the number of mesh grids traversed by a single light-ray is in the order of $N_\mathrm{m}^{1/3}$. Therefore, the total computational cost is proportional to $N_\mathrm{m} N_\mathrm{d}$.

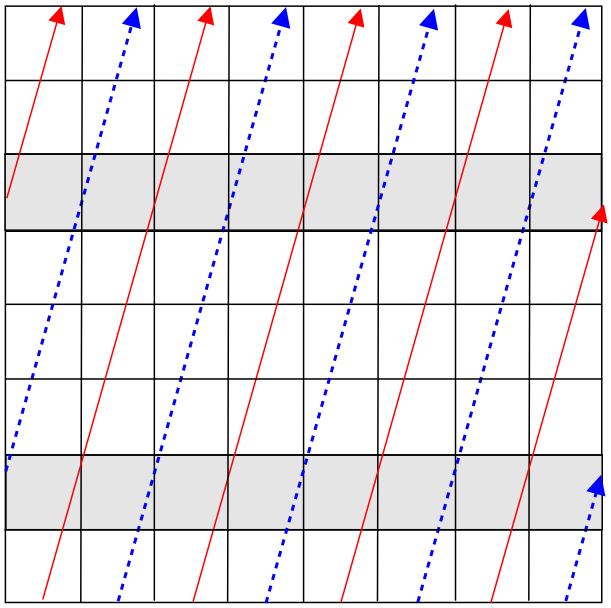

Figure 2.2: Schematic illustration of the ray-tracing scheme for the diffuse radiation in the two-dimensional mesh grid. For a given direction, equally-spaced parallel light-rays are cast from boundaries of the simulation volume and travel to the other boundaries. Note that gray mesh grids are traversed by multiple parallel light-rays, while the subsets of light-rays depicted by solid or dotted lines get through them only once.

2.4 Angular resolution for RT of the diffuse radiation

The number of the directions of light-rays, $N_{\rm d}$, determines angular resolution of the RT of the diffuse radiation. In order to guarantee that light-rays from a mesh grid on a face of the simulation box reach all the mesh grids on the other faces, $N_{\rm d}$ should be in the order of $N_{\rm m}^{2/3}$. In the case that the mean free path of the diffuse photons is sufficiently shorter the simulation box size, however, such a large $N_{\rm d}$ is redundant because only a small fraction of diffuse photons reach the other faces, and we can reduce the total computational cost by decreasing the number of directions, $N_{\rm d}$, while keeping the reasonable accuracy of the diffuse RT. Thus, the number of directions should be flexibly changed depending on the physical state.

To achieve this, we use the HEALPix (Hierarchical Equal Area isoLatitude Pixelization) software package (Gorski et al., 2005) [1] to set up the directions of the light-rays. The HEALPix is suitable to our purposes in the sense that each direction corresponds to exactly the same solid angle and that the directions are nearly uniformly sampled. Furthermore, it can provide a set of directions with these properties in arbitrary resolutions, each of which contains $12N_{\rm side}^2$ directions, where $N_{\rm side}$ is an angular resolution parameter. Since it is larger than the number of mesh grids on six faces of a cube with a side length of $N_{\rm side}$ mesh spacings, $6N_{\rm side}^2$, it is expected that a set of light-rays originated from a single point with directions generated by the HEALPix with an angular resolution parameter of $N_{\rm side}$ get through all the mesh grids within a cube centered by the point with a side length of $N_{\rm side}$ mesh spacings. Thus, the optimal number of directions should be chosen so that the mean free path of the recombination photons

[1] `http://healpix.jpl.nasa.gov/`

Table 2.1: Rates of chemical reactions and radiative cooling processes adopted in this thesis. Reference for radiative recombination rates (RR) of HII, HeII and HeIII in the case-A and case-B approximation; collisional ionization rates (CIR) of HI, HeI, and HeII; recombination cooling rates (RCR) of HII, HeII and HeIII in the case-A and case-B approximation; collisional ionization cooling rates (CICR) of HI, HeI and HeII; collisional excitation cooling rates (CECR) of HI, HeI and HeII; bremsstrahlung cooling rate; inverse Compton cooling rate (CCR); photoionization cross sections (CS) of HI, HeI and HeII.

physical process	literature
RR (case-A)	(1), (1), (2)
RR (case-B)	(3), (3), (3)
CIR	(7), (7), (1)
RCR (case-A)	(2), (2), (2)
RCR (case-B)	(3), (5), (3)
CICR	(2), (2), (2)
CECR	(2), (2), (2)
BCR	(4)
CCR	(6)
CS	(8), (8), (8)

(1) Abel et al. (1997); (2) Cen (1992); (3) Hui & Gnedin (1997); (4) Hummer (1994); (5) Hummer & Storey (1998); (6) Ikeuchi & Ostriker (1986); (7) Janev et al. (1988); (8) Osterbrock (2006);

is sufficiently shorter than $N_{\rm side}\Delta H$, where ΔH is the mesh spacing.

2.5 Chemical reaction and cooling rates

The chemical reaction rates and radiative cooling rates adopted in this thesis are identical to those adopted in Okamoto et al. (2012), and the literatures from which we adopt these rates are summarized in Table 2.1.

2.6 Ionization Balance

The time evolution of the number density of the i-th chemical species can be schematically described by

$$\frac{dn_i}{dt} = C_i(T, n_j) - D_i(T, n_j)n_i, \tag{2.22}$$

where $C_i(T, n_j)$ is the collective production rate of the i-th species and $D_i(T, n_j)n_i$ is the destruction rate of the i-the species. For example, in the case of atomic hydrogen, $C_{\rm HI}$ and $D_{\rm HI}$ is given by

$$C_{\rm HI} = \alpha_{\rm HII}\, n_{\rm e} n_{\rm HII} \tag{2.23}$$

$$D_{\rm HI} = \Gamma_{\rm HI,c} n_{\rm e} + \Gamma_{\rm HI,\gamma} \tag{2.24}$$

where $\alpha_{\rm HII}(T)$ is the radiative recombination rate of HII, $\Gamma_{\rm HI,c}$ is the collisional ionization rate and $\Gamma_{\rm HI,\gamma} = \sum_\alpha \Gamma^\alpha_{\rm HI,\gamma} + \Gamma^{\rm diff}_{\rm HI,\gamma}$ is the photoionization rate of HI.

These equations are numerically solved using the backward difference formula (BDF) (Anninos et al., 1997; Yoshikawa & Sasaki, 2006), in which the number densities of the i-th chemical species at a time $t + \Delta t$, $n_i^{t+\Delta t}$, is computed as

$$n_i^{t+\Delta t} = \frac{C_i \Delta t + n_i^t}{1 + D_i \Delta t}, \tag{2.25}$$

where, C_i and D_i are estimated with the number densities of each species at the advanced time, $n_j^{t+\Delta t}$. However, the number densities in the advanced time step are not available for all the chemical species in evaluating C_i due to the intrinsic non-linearity of equation 2.22. Thus, we sequentially update the number densities of each chemical species in the increasing order of ionization levels rather than updating all the species simultaneously. It is confirmed that this scheme is stable and accurate (Anninos et al., 1997; Yoshikawa & Sasaki, 2006).

2.7 Photo-heating and radiative cooling

The specific energy change for each mesh by the photo-heating and radiative cooling is followed by the energy equation

$$\frac{du}{dt} = \frac{\mathcal{H} - \mathcal{C}}{\rho}, \tag{2.26}$$

where u is the specific internal energy and $\mathcal{H}$ and $\mathcal{C}$ are the photo-heating and cooling rate, respectively and $\mathcal{H}$ is given by

$$\mathcal{H} = \sum_i n_i \left(\sum_\alpha \mathcal{H}_i^\alpha + \mathcal{H}_i^{\rm diff} \right). \tag{2.27}$$

The specific internal energy for each mesh is updated implicitly by solving the equation

$$u^{t+\Delta t} = u^t + \frac{\mathcal{H}^{t+\Delta t} - \mathcal{C}^{t+\Delta t}}{\rho^t} \Delta t \tag{2.28}$$

for $u^{t+\Delta t}$, where the photo-heating $\mathcal{H}^{t+\Delta t} = \mathcal{H}(n^{t+\Delta t})$ and cooling rates $\mathcal{C}^{t+\Delta t} = \mathcal{C}(n^{t+\Delta t}, u^{t+\Delta t})$ are evaluated at the advanced time $t + \Delta t$.

2.8 Timestep constraints

Since we solve the static RT equation (2.1), equations (2.22) for chemical reactions and (2.26) for photo-heating and radiative cooling have to be solved iteratively until the electron number density and specific internal energy in each mesh grid converges: $|n_{\rm e}^{(i)} - n_{\rm e}^{(i-1)}| < \epsilon n_{\rm e}^{(i)}$ and $|u^{(i)} - u^{(i-1)}| < \epsilon u^{(i)}$, where ϵ is an accuracy parameter, and $u^{(i)}$ and $n_{\rm e}^{(i)}$ indicate the specific internal energy and the electron number density after the i-th iteration, respectively.

The timestep in solving chemical reactions and energy equation, $\Delta t_{\rm chem}$, is set to

$$\Delta t_{\rm chem} = \epsilon_{\rm e} \left| \frac{n_{\rm e}}{\dot{n}_{\rm e}} \right| + \epsilon_{\rm HI} \left| \frac{n_{\rm HI}}{\dot{n}_{\rm HI}} \right|, \tag{2.29}$$

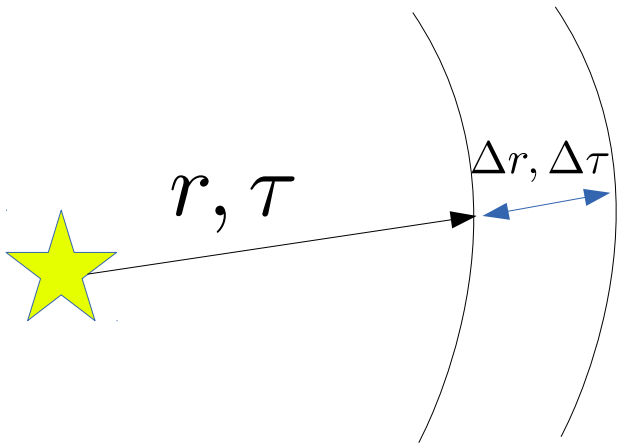

Figure 2.3: Schematic illustration of the photon-conserving method. The number of photo-ionization in the shell is equal to the number of absorped in the shell.

where $\epsilon_{\rm e}$ is 0.1 and $\epsilon_{\rm HI}$ is 0.0001, so that the maximum fractional change in the electron number density is less than 10% and the neutral hydrogen number density is less than 0.01% per time step.

The timestep, Δt, with which we update the radiation field can be larger than the chemical timestep, $\Delta t_{\rm chem}$ by subcycling the rate and energy equations (2.22) and (2.26). Throughout in this thesis, the timestep for the RT calculation is set to

$$\Delta t = F \min_i \Delta t_{{\rm chem},i}, \tag{2.30}$$

where $\Delta t_{{\rm chem},i}$ is the chemical timestep for the i-th mesh grid, and we typically set $F = 1 \sim 10$ so that the radiation field successfully converges with a reasonable number of iterations.

In solving ionization and thermal states of gaseous medium iteratively, the solutions converge prohibitively slowly when we have mesh grids which are very optically thick. To avoid such slow convergence, we spatially smooth ionization and heating rates of each mesh grids over the adjacent 27 mesh grids.

2.9 Photon-Conserving Method

To remedy the slow convergence of the interation described above, we also adopt the photon-conserving method Abel et al. (1999), in which the photo-ionization and photo-heating rates are calculated so that the numbers of absorped photons and photo-ionization events balance exactly.

We consider a spherical shell centered by a point radiating source as shown in Figure 2.3, where the volume and radial optical depth of the shell are $V_{\rm s}$ and $\Delta\tau_\nu$, respectively. The incoming photon number per unit time $\dot{N}_{{\rm in},\nu}$ is given by

$$\dot{N}_{{\rm in},\nu} = \frac{L_\nu \exp(-\tau_\nu)}{h\nu}, \tag{2.31}$$

where L_ν is the luminosity density at a frequency ν, and τ_ν is the optical depth between the point source and the inner side of the shell. The outgoing photon number per unit time from the outer side of the shell is written as

$$\dot{N}_{{\rm out},\nu} = \frac{L_\nu \exp(-(\tau_\nu + \Delta\tau_\nu))}{h\nu}. \tag{2.32}$$

Then, the number of absorped photons per unit time $\dot{N}_{\rm abs}$ is given by

$$\dot{N}_{{\rm abs},\nu} = \dot{N}_{{\rm out},\nu} - \dot{N}_{{\rm in},\nu} = \frac{L_\nu \exp(-\tau_\nu)}{h\nu} \left[1 - \exp(-\Delta\tau_\nu)\right]. \tag{2.33}$$

When we consider multiple chemical components, the absoption rate of the i-th species is rewritten as

$$\dot{N}^i_{{\rm abs},\nu} = \frac{\Delta\tau^i_\nu}{\Delta\tau_\nu} \frac{L_\nu \exp(-\tau_\nu)}{h\nu} \left[1 - \exp(-\Delta\tau_\nu)\right], \tag{2.34}$$

where $\Delta\tau^i_\nu$ is a optical depth contributed by the i-th component, and $\Delta\tau_\nu = \sum_i \Delta\tau^i_\nu$ is the total optical depth. Since $\dot{N}^i_{{\rm abs},\nu}$ is equal to the number of ionization of the i-th species, the photo-ionization rate of the i-th component can be written as

$$\Gamma_i \equiv \frac{1}{N_i} \int_{\nu_i}^{\infty} \dot{N}^i_{{\rm abs},\nu} d\nu, \tag{2.35}$$

where ν_i is the threshold frequecy of the i-th species and N_i is the number of i-th species in the shell. The photo-heating is similarly calculated in terms of $\dot{N}_{{\rm abs},\nu}$ as

$$\mathcal{H}_i = \frac{1}{V_{\rm s}} \int_{\nu_i}^{\infty} \dot{N}_{{\rm abs},\nu} (h\nu - h\nu_i) d\nu. \tag{2.36}$$

We find that the photon conserving scheme reduce the number of interation to converge the ionization and thermal states even without smoothing the ionization and heating rates. However, combination of photon conserving scheme and smoothing of the ionization and heating rates requires the smallest number of interation to achieve the convergence of the ionization and thermal states.

Chapter 3

Coupling of Radiation Transfer and Hydrodynamics

In this chapter, we describe the hydrodynamics scheme AUSM+ (Advection Upstream Splitting Method) (Liou, 1996) and its coupling with the radiation transfer schemes described in the previous chapter to develop a radiation hydrodynamic code, `ARGOT`.

3.1 Numerical Hydrodynamics scheme : AUSM+

Equations of hydrodynamics are given by

$$\frac{\partial \rho}{\partial t} + \nabla \cdot (\rho \mathbf{v}) = 0, \tag{3.1}$$

$$\frac{\partial \mathbf{v}}{\partial t} + (\mathbf{v} \cdot \nabla)\mathbf{v} = -\frac{1}{\rho}\nabla p + \mathbf{g}, \tag{3.2}$$

$$\frac{\partial E}{\partial t} + \nabla \cdot (E + p)\mathbf{v} = \rho \mathbf{v} \cdot \mathbf{g}, \tag{3.3}$$

where ρ is density, $\mathbf{v}$ is velocity, p is pressure, E is total energy and $\mathbf{g}$ is external force. In this section, we do not consider any external force term $\mathbf{g} = 0$.

These equations (3.1) $\sim$ (3.3) can be written in a conservation form as

$$\frac{\partial \mathbf{U}}{\partial t} + \nabla \cdot \mathbf{F} = 0, \tag{3.4}$$

where $\mathbf{U}$ and $\mathbf{F}$ are given by

$$\mathbf{U} = \begin{pmatrix} \rho \\ \rho \mathbf{v} \\ \rho e_t \end{pmatrix} = \begin{pmatrix} \rho \\ \rho \mathbf{v} \\ \rho u + \frac{1}{2}\rho \mathbf{v}^2 \end{pmatrix}, \tag{3.5}$$

$$\mathbf{F} = \begin{pmatrix} \rho \mathbf{v} \\ p + \rho \mathbf{v}^2 \\ (\rho e_t + p)\mathbf{v} \end{pmatrix} = \begin{pmatrix} \rho \mathbf{v} \\ p + \rho \mathbf{v}^2 \\ \rho \mathbf{v} h_t \end{pmatrix}, \tag{3.6}$$

where u is an internal energy per unit mass, $e_t = u + \mathbf{v}^2/2 = E/\rho$ is a total energy per unit mass, $h_t = p/\rho + e_t$ is an enthalpy per unit mass.

Among many schemes to simulate hydrodynamic equations, we adopt AUSM+ (Advection Upstream Splitting + Method) (Liou, 1996) as a computational fluid scheme that split the numerical flux $\mathbf{F}$ into a convection term $\mathbf{F}^{(c)}$ and a pressure term $\mathbf{P}$.

$$\mathbf{F} = \mathbf{F}^{(c)} + \mathbf{P}, \tag{3.7}$$

where each term is defined as

$$\mathbf{F}^{(c)} = Ma \begin{pmatrix} \rho \\ \rho \mathbf{v} \\ \rho h_t \end{pmatrix} \equiv Ma\mathbf{\Phi}, \qquad \mathbf{P} = \begin{pmatrix} 0 \\ p \\ 0 \end{pmatrix}, \tag{3.8}$$

where M is a Mach number, a is a sound speed. In the AUSM+ scheme, the numerical flux at interface of the j-th and $j+1$-th mesh is given by

$$\begin{aligned} \mathbf{F}_{j\pm1/2} &= \mathbf{F}^{(c)}_{j\pm1/2} + \mathbf{P}_{j\pm1/2} \\ &= M_{j\pm1/2} a_{j\pm1/2} \frac{\mathbf{\Phi}_j + \mathbf{\Phi}_{j\pm1}}{2} - \frac{a_{j\pm1/2}}{2} \left| M_{j\pm1/2} \right| (\mathbf{\Phi}_{j\pm1} - \mathbf{\Phi}_j) + p_{j\pm1/2}, \end{aligned} \tag{3.9}$$

where

$$M_{j+1/2} = M^+(M_j) + M^-(M_{j+1}), \qquad M^\pm(M) \equiv \begin{cases} \frac{1}{2}(M + |M|) & (|M| \geq 1) \\ \pm\frac{1}{4}(M \pm 1)^2 \pm \beta(M^2-1)^2 & (\text{otherwise}) \end{cases}, \tag{3.10}$$

$$p_{j+1/2} = P^+(M_j) p_j + M^-(M_{j+1}) p_{j+1}, \qquad P^\pm(M) \equiv \frac{1}{4}(M \mp 1)^2 (2 \mp M) \pm \alpha M (M^2-1)^2, \tag{3.11}$$

$$a_{j+1/2} = \frac{a^*_j}{u_j}. \tag{3.12}$$

The interface value at $j - 1/2$ can be calculated similarly. a^* is the critical speed of sound via the isoenergetic condition for ideal gas, and given by

$$\frac{(\gamma+1)a^{*2}}{2(\gamma-1)} = \frac{a^2}{\gamma-1} + \frac{1}{2}u^2 = h_t. \tag{3.13}$$

The parameter α and β are free parameters within ranges of $-3/4 \leq \alpha \leq 3/16$ and $-1/16 \leq \beta \leq 1/2$. In the followings, we set the $\alpha = 3/16$, $\beta = 1/8$.

3.2 Time-step of Hydrodynamics

The time-step for the integration of the hydrodynamic equations is determined by the CFL condition. The time-step in the i-th mesh is

$$dt^i_{\rm mesh} = \min\left(\frac{\Delta x}{|v_{i,x}| + a_i}, \frac{\Delta y}{|v_{i,y}| + a_i}, \frac{\Delta z}{|v_{i,z}| + a_i} \right), \tag{3.14}$$

where Δx, Δy and Δz are mesh spacings in each direction, $v_{i,x}$, $v_{i,y}$ and $v_{i,z}$ are velocity components in each direction, and a is a sound speed in the mesh, respectively. The time-step for the hydrodynamic step $dt_{\rm hy}$ is given by the smallest of $dt^i_{\rm mesh}$ as

$$dt_{hy} = \mathcal{C} \times \min\left(dt_{mesh}\right), \tag{3.15}$$

where $\mathcal{C}$ is CFL parameter, which is set to 0.2 throughout in this thesis.

The interface values of physical quantities in the j-th mesh grid at $j+1/2$ and $j-1/2$ are computed using the MUSCL (Monotonic Upstream-Centered Scheme for Conservation Laws) scheme (Van Leer, 1979) which has second order accuracy and assures the TVD (Total Variation Diminishing) property. As for the time integration, we adopt the second order TVD Runge-Kutta scheme to equalize the order of accuracy in space and time.

3.3 Coupling of Radiation Transfer and Hydrodynamics

The equations of hydrodynamics coupled with radiation transfer are given by

$$\frac{\partial \rho}{\partial t} + \nabla \cdot (\rho \mathbf{v}) = 0, \tag{3.16}$$

$$\frac{\partial \mathbf{v}}{\partial t} + (\mathbf{v} \cdot \nabla)\mathbf{v} = -\frac{1}{\rho}\nabla p \tag{3.17}$$

$$\frac{\partial E}{\partial t} + \nabla \cdot (E + p)\mathbf{v} = \mathcal{H} - \Lambda \tag{3.18}$$

where $\mathcal{H}$ and Λ are photo-heating and radiative cooling rates, respecitvely. We do not consider the effect radiation pressure in this thesis. This photo-heating and radiative cooling rates are obtained as outcomes of the radiation transfer calculations. The photo-heating and radiative cooling terms are updated by using a semi-implicit scheme described in equation (2.28).

The time-step for radiative transfer $dt_{\rm rad}$ given by equation (2.30) is usually smaller than that of hydrodynamics $dt_{\rm hy}$ given by (3.15). Therefore we adopt the global time-step dt defined as the smaller of $dt_{\rm rad}$ and $dt_{\rm hy}$,

$$dt = \min(dt_{rad}, dt_{hy}). \tag{3.19}$$

Figure 3.1 shows the flow chart of radiation hydrodynamic simulation. The left panel (a) indicate the entire program integrated by the global time-step. The right panel (b) depicts the details of the radiation transfer calculation, which includes the calculations of radiation transfer using ARGOT and ART schemes and chemical reactions. In the chemical reaction step, time-step is set to $dt_{\rm chem} = 0.1 \times dt_{\rm rad}$, and we sub-cycle the chemical reactions with $dt_{\rm chem}$.

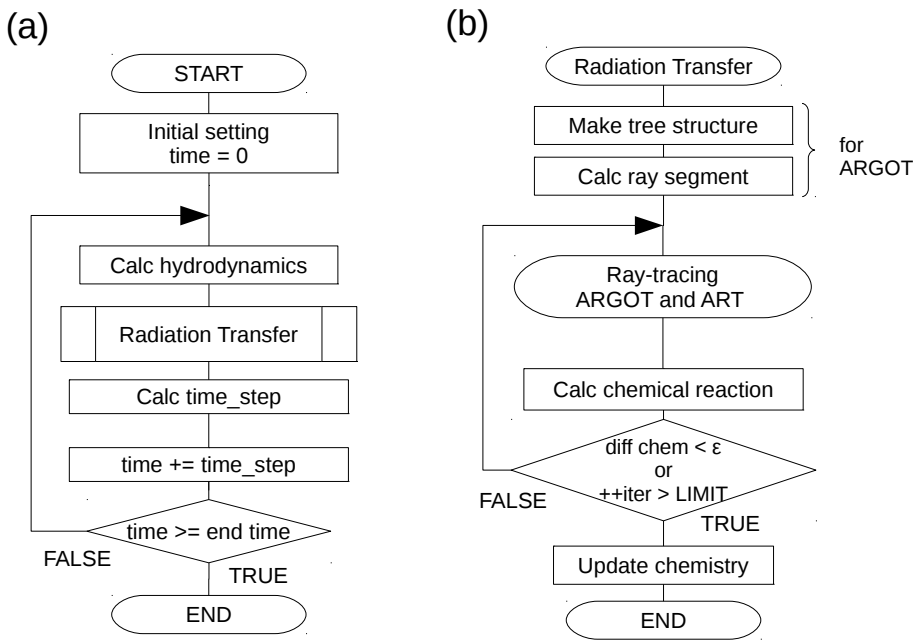

Figure 3.1: Flow chart of radiation hydrodynamic simulation. (a) is the entire program. (b) is the radiation transfer part.

Chapter 4

Implementation on Multi-Core System

In this chapter, we describe the details of the implementation of the RT calculation of the diffuse radiation and point source radiation which performs effectively on recently popular processors with highly parallel architecture, such as Graphics Processing Units (GPUs), multi-core CPUs, and many-core processors. Throughout this thesis, we present the results using the implementation with the `OpenMP` and `CUDA` technologies. The former is supported by most of the recent multi-core processors, and the many-core processors such as the Intel Xeon-Phi processor, while the latter is the parallel programming platform for GPUs producted by NVIDIA.

In the implementation on GPUs with the `CUDA` platform, the fluid dynamical and chemical data in all the mesh grids are transferred from the memory associated with CPUs to those of GPUs prior to the RT calculations. After the RT calculations, ionization rates and heating rates in all the mesh grids computed on GPUs are sent back to the CPU memory.

4.1 Ray Grouping for ART

In the calculations of the transfer of the diffuse radiation described in the section 2.3, many parallel light-rays travel from boundaries of the simulation volume until they reach the other boundaries. On processors with highly parallel architecture, a straightforward implementation is to assign a single thread to compute the RT along each light-ray and calculate the RT along multiple light-rays in parallel. Such a simple implementation, however, does not work because some mesh grids are traversed by multiple parallel light-rays (see gray mesh grids in Figure 2.2), and in computing equation (2.11), multiple computational threads write data to the identical memory addresses. Thus, equation (2.11) has to be computed not in parallel but in a exclusive manner using the "atomic operations". The use of the atomic operations, however, significantly degrade the parallel efficiency and computational performance in many architectures. Figure 4.1 is a schematic illustration of parallel thread flows with and without atomic operations.

To avoid such use of atomic operations and the deterioration of the parallel efficiency, we split the parallel light-rays into several groups so that parallel light-rays in each group do not traverse any mesh grid more than once. For example, in two-dimensional mesh grids in Figure 2.2, parallel light-rays are split into two groups each of which are depicted by solid and dotted lines. One can see that light-rays in each groups do not intersect any mesh grids more than once. We can extend this technique to the three-dimensional mesh grids by splitting the parallel light-rays into four groups, where the light-rays in

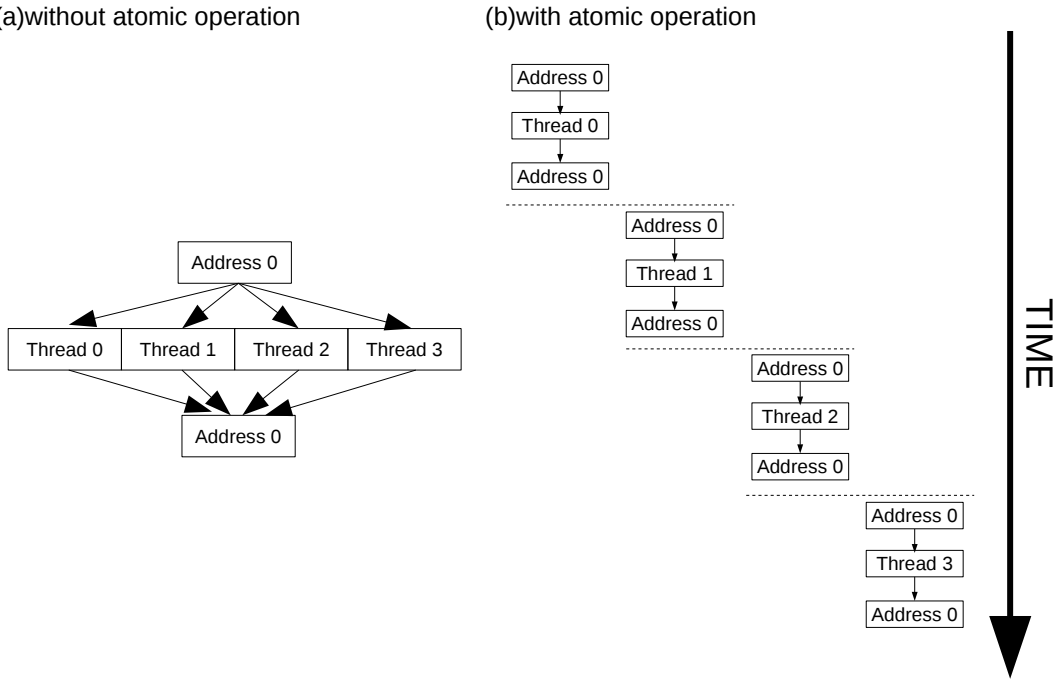

Figure 4.1: Schematic illustrations of thread parallelization with and without atomic operations. In the left panel, the results of each parallel thread are written in the memory address "Address 0" after all the thread finish. On the other hand, in the right panel, a read from and a write to the identical memory address "Address 0" take place in each thread, where atomic operations are required.

each group are cast from the two-dimensionally interleaved mesh grids as depicted by the same color in Figure 4.2. If compute each group in order, the same number of light rays as the original, it is possible to exclusion the atomic operations.

4.2 Efficient Use of Multiple External Accelerators for ART

Many recent supercomputers are equipped with multiple external accelerators such as GPUs on a single computational node, each of which has an independent memory space. To attain the maximum benefit of the multiple accelerators, we decompose calculations of the diffuse radiation transfer according to the directions of the light-rays, and assign the decomposed RT calculation to the multiple accelerators. After carrying out the RT calculation for the assigned set of directions, and computing the mean intensity with equation (2.13) averaged over the partial set of directions on each external accelerator, the results are transferred to the memory on the hosting nodes. Then, we obtain the mean intensity averaged over all directions.

4.3 Node Parallelization for ART

In addition to the thread parallelization within processors, we implement the inter-node parallelization using the Message Passing Interface (MPI). In the inter-node parallelization, the simulation box is evenly decomposed into smaller rectangular blocks with equal volumes along the Cartesian coordinate.

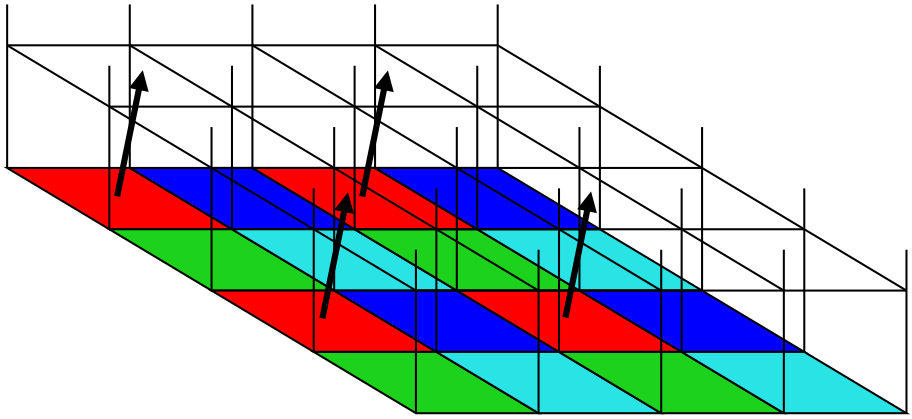

Figure 4.2: Schematic illustration of light-ray grouping for the three-dimensional mesh grids. Light-rays in each group start from boundary faces of mesh grids painted with the same color. Only the light-rays in one group are shown in this figure.

For the inter-node parallelization of the calculations of the diffuse RT, we adopt the multiple wave front (MWF) scheme developed by Nakamoto et al. (2001), in which light-ray directions are classified into eight groups according to signs of their three direction cosines, and for each group of light-ray directions, the RT calculations along each direction are carried out in parallel on a "wave front" in the node space, while the RT for different directions are computed on the other wave fronts simultaneously. By transferring the radiation intensities at the boundaries from upstream nodes to downstream ones, one can sequentially compute the RT of diffuse radiation along all the directions in each group of light-ray directions. Fig 4.3 illustrates the step-by-step procedures of MWF scheme in the two-dimensional case.

The theoretical parallelization efficiency f of the MWF scheme for the three-dimensional is estimated as

$$f = \frac{N_\theta N_\phi/8}{N_\theta N_\phi/8 + N_x + N_y + N_z - 3} \tag{4.1}$$

where, $N_\theta N_\phi$ is the number of directions determined by the direction parameter N_{side} of HEALPix and N_x, N_y, and N_z are number of MPI processes along each axis. For example, in our test simulations, we nominally adopt $N_{\rm side} = 8$ indicating that $N_\theta N_\phi = 768$, and $N_x N_y N_z = 8$ $(N_x = 2, N_y = 2, N_z = 2)$, and have theoretical efficiency of $f = 0.9697$. This formula is modified when the ray-tracing calculations along light-rays with multiple directions are carried out simultaneously. In our implementation on GPUs, we can compute the ray-tracing along four different directions simultaneously with four GPU boards in one computational nodes, then the efficiency is given by

$$f = \frac{N_\theta N_\phi/(8 \times N_A)}{N_\theta N_\phi/(8 \times N_A) + N_x + N_y + N_z - 3} \tag{4.2}$$

where, N_A is the number of external accelerator devices, or GPUs in our implementation. Since we have four GPUs in a single node, the theoretical efficiency is $f = 0.8889$, and slightly decreases because the number of directions is reduced by the number of accelerators.

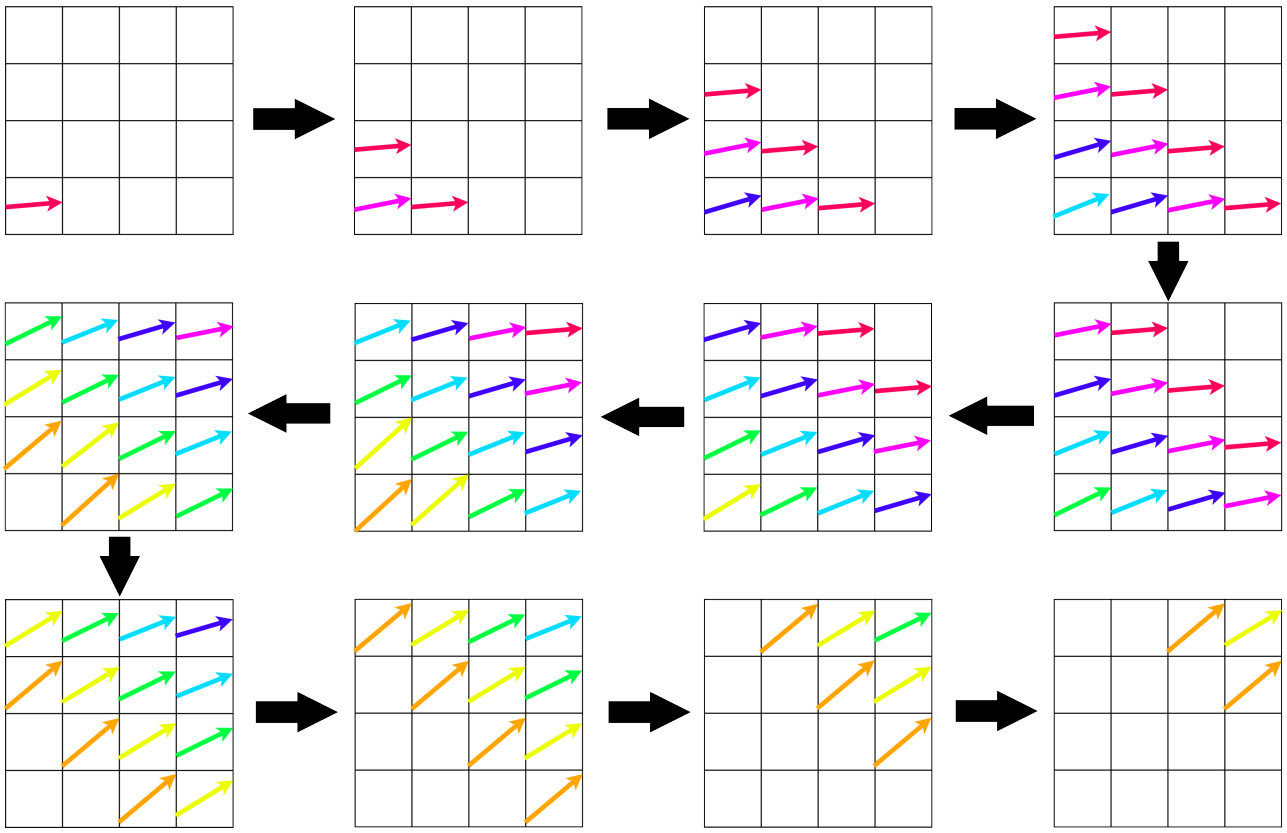

Figure 4.3: Conceptual diagram of Multiple Wave Front Method in two-dimensional. Each mesh grids represents the computational node. The ray direction from bottom left is propagated from the lower left corner of the node. While the occupancy rate of nodes is low in only first and last stage of the calculation, the total efficiency is high when the number of direction is sufficiently larger than number of nodes.

Chapter 5

Numerical Simulations

In this chapter, we present a series of test simulations to validate our RT code and show the effect of diffuse radiation transfer. Test-1 to Test-4 are radiation transfer simulations with static density field, while Test-5 to Test-7 are radiation hydrodynamic simulations. Test-1 computes an expansion of the ionization front in hydrogen gas with a uniform density field by a monochromatic point source. Test-2 is the same as Test-1 except that the spectrum of the radiation is the blackbody rather than the monochromatic one, and the effect of photo-heating is incorporated. Test-3 simulates the the expansion of the ionization front by the one-side incident radiation and show the shadowing effect by dense clump. Test-4 shows the ionization of cosmological density field by multiple ionization point sources. The initial conditions of Test-5 and Test-7 are the same as those of Test-2 and Test-3, respectively but they incorporate the hydrodynamic calculations.

Actually, these tests are identical to those in Cosmological Radiative Transfer Codes Comparison Project [1] described in Iliev et al. (2006) and Iliev et al. (2009), which compares several algorithm and implementation of RT code and radiation-hydridynamic code. All the tests in this project adopt the on-the-spot approximation, and ignore the effect of recombination radiation, and the results in Iliev et al. (2006) and Iliev et al. (2009) can be directly compared with our results with on-the-spot approximation. Among the codes preseted in Iliev et al. (2006) and Iliev et al. (2009), RSPH code which is an SPH code coupled with the radiation transfer scheme described in Susa (2006) is the most close to the first-princple calculation and thus reliable. Therefore, in the followings, we primarily compare our results with those by RSPH code as reference results.

5.1 Test-1 : HII region expansion in a static homogeneous gas

The first test is the simple problem of a HII region expansion in a static homogeneous gas which consists of only hydrogen around a single monochromatic ionizing source. We adopt the same initial condition as that of Test-1 in Cosmological Radiative Transfer Codes Comparison Project I (Iliev et al., 2006), where the static hydrogen number density is $n_{\rm H} = 10^{-3}\,{\rm cm}^{-3}$ and the static gas temperature is $T = 10^4\,{\rm K}$. The ionizing source emits $\dot{N}_\gamma = 5\times10^{48}$ s^{-1} ionizing photons per second with a photon energy of $h\nu = 13.6$ eV, and is located at a corner of simulation box with a side length of 6.6 kpc. The initial ionization fraction $f_{\rm HII} = n_{\rm HII}/n_{\rm H} = 1.2\times10^{-3}$ under the collisional ionization equilibrium. In this test, RT simulations are

[1] `http://www.phys.susx.ac.uk/~cs390/RT_comparison_project/index.html`

carried out with 256^3 mesh grids and the angular resolution parameter of $N_{\rm side} = 8$.

The recombination time is defined by

$$t_{\rm rec} = \frac{1}{\alpha_{\rm B}(T) n_{\rm HI}}, \tag{5.1}$$

and the Strömgren radius is

$$r_{\rm s} = \left[\frac{3\dot{N}_\gamma}{4\pi\alpha_{\rm B}(T) n_{\rm HI} n_{\rm e}} \right]^{1/3}, \tag{5.2}$$

where $\alpha_{\rm B}(T)$ is the Case-B recombination rate that depends on the temperature T, and $n_{\rm e}$ and $n_{\rm HI}$ are the electron and neutral hydrogen number density, respectively. The Strömgren radius is the maximum expanding radius of the HII region in the Case-B condition around the epoch of the recombination time after the ignition of the point radiating source. In this initial condition, the recombination time is $t_{\rm rec} = 122.4\,{\rm Myr}$ and the Strömgren radius is estimated to be 5.4 kpc at $T = 10^4\,{\rm K}$ where the Case-B recombination rate is given by $\alpha_{\rm B}(T) = 2.59 \times 10^{-13} (T/10^4\,{\rm K})^{-3/4}$.

Figure 5.1 shows the radial profiles of ionized and neutral fractions at $t = 30\,{\rm Myr}$, $100\,{\rm Myr}$ and $500\,{\rm Myr}$. The red solid and blue solid lines indicate the results with and without the effect of recombination radiation, respectively. In the runs without the effect of recombination radiation, we do not incorporate the transfer of diffuse radiation and adopt the Case-B recombination rates. The black dashed lines depict the result of RSPH (Susa, 2006) and is consistet with our results without the effect of recombination radiation. The result without the effect of recombination radiation at $t = 500\,{\rm Myr}$, the position of ionization front is in good agreement with the analytical Strömgren radius. On the other hand, in the runs with the effect of recombination radiation, we adopt the Case-A recombination rates and the transfer of reombination radiation is turned on. The results with the effect of the recombination radiation indicate that the ionization fronts are more extended than those in the runs without the effect of recombination radiation, especially at later stages, because of the additional ionizing photons emitted in the ionized region.

In Figure 5.2, maps of the neutral fraction of hydrogen in the source-plane of the simulation volume at $t = 30\,{\rm Myr}, 100\,{\rm Myr}$ and $500\,{\rm Myr}$ are shown. In the run with the recombination radiation, the ionized region is more extended than that in the run without the recombination radiation. The maps of with diffuse photon RT at later stage deviate from spherical symmetry since the transfer of recombination photons from the outer regions is not considered in our implementaion.

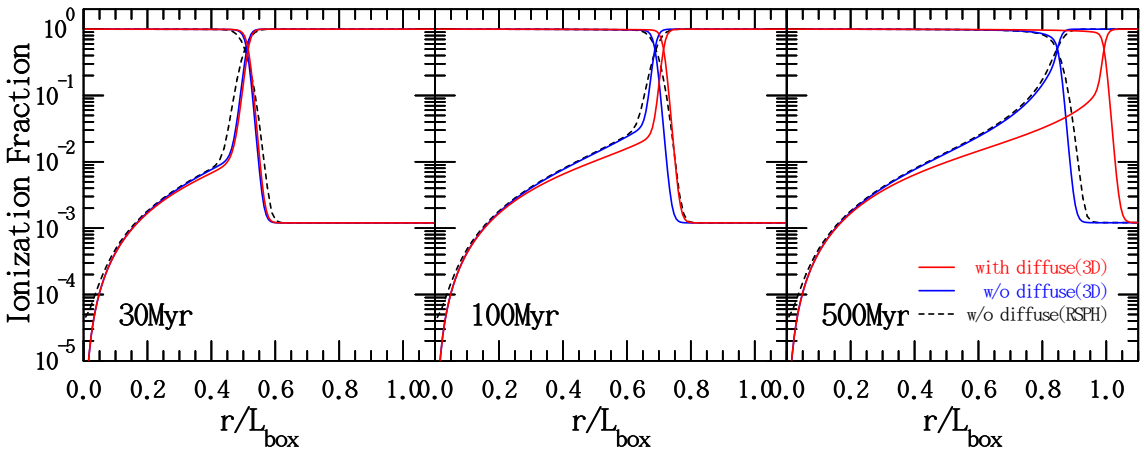

Figure 5.1: Test-1: Radial profiles of ionization fraction of hydrogen at $t = 30\,\mathrm{Myr}$, 100 Myr and 500 Myr. Red and blue solid lines indicate the results with and without the effect of recombination radiation, respectively. Black dashed lines show the results without recombination radiation computed by RSPH (Susa, 2006).

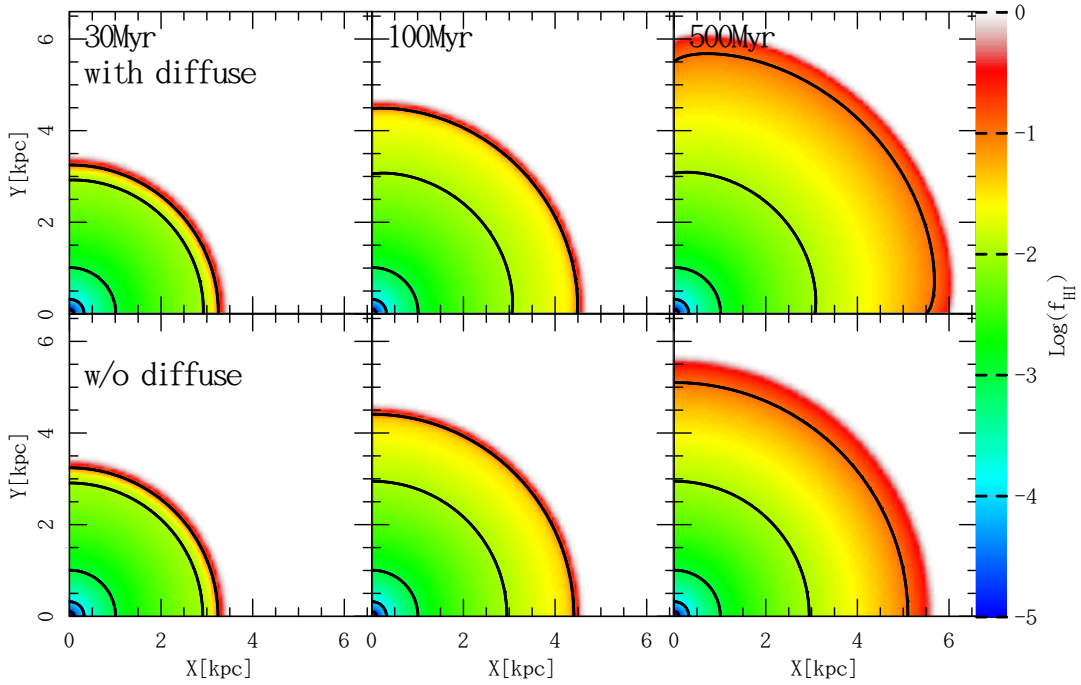

Figure 5.2: Test-1: Maps of neutral fraction of hydrogen in the source-plane of the simulation box at $t = 30\,\mathrm{Myr}$, 100 Myr and 500 Myr. The upper and lower panels show the results with and without the recombination radiation, respectively.

5.2 Test-2 : HII region expansion with the temperature state

The second test is almost the same as Test-1 but the point source has the blackbody spectrum emission and thus we incorporate photo-heating in the thermal evolution. We adopt the same initial condition as that of Test-2 in Iliev et al. (2006). The initial gas temperature is $T = 100\,\mathrm{K}$. The ionizing source emits the blackbody radiation with an effective temperature of $10^5\,\mathrm{K}$, and 5×10^{48} ionizing photons per second. The initial ionization state of hydrogen is almost neutral.

Figure 5.3 and 5.4 show the radial profiles of ionized fraction and gas temperature at $t = 30\,\mathrm{Myr}$, 100 Myr and 500 Myr. The red solid and blue solid lines indicate the results with and without the effect of recombination radiation, respectively. The black-dashed lines are the results obtained with RSPH code Susa (2006) and in good agreement with the blue solid lines as expected. In this test, we compare our results with the effect of recombination photons with the ones obtained with the one-dimensional spherically symmetric RT code by Kitayama et al. (2004), which also incorporates the RT of recombination photons emitted by the ionized hydrogen using the impact-parameter method and are indicated with magenta dashed lines. We find that the one-dimensional results with the effect of recombination radiation show a good agreement with our three-dimensional results (red solid lines), which support the validity of our implementation of diffuse radiation transfer. On the other hand, since the spectrum of the point radiating source is relatively "hard" and the energy of each recombination photon is close to the Lyman limit energy, the recombination photons does not make strong impact on the temperature profiles.

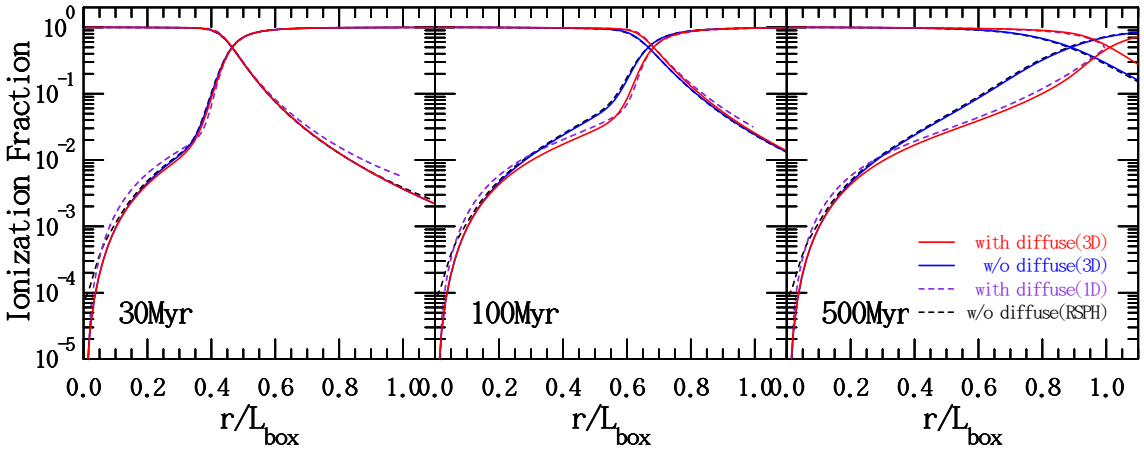

Figure 5.3: Test-2: Radial profiles of ionization fraction of hydrogen at $t = 30\,\mathrm{Myr}$, 100 Myr and 500 Myr. Red and blue solid lines indicate the results with and without the recombination radiation, respectively. Magenta bashed lines show the results obtained with one-dimensional spherically symmetric code with the effect of recombination radiation presented in (Kitayama et al., 2004). Black dashed lines indicate the results without the recombination radiation computed by RSPH.

5.2.1 Shadowing by a dense gas clump

As a variant of this test, we conduct RT simulation with modified initial condition in which we place a dense gas clump near the point radiating source. The radius of the clump is 0.54 kpc and it is located at 0.8 kpc apart from the point radiation source along the x-direction, and its density is 200 times higher than that of the ambient gas, and the initial temperature is set to 100 K. The spectrum and luminosity

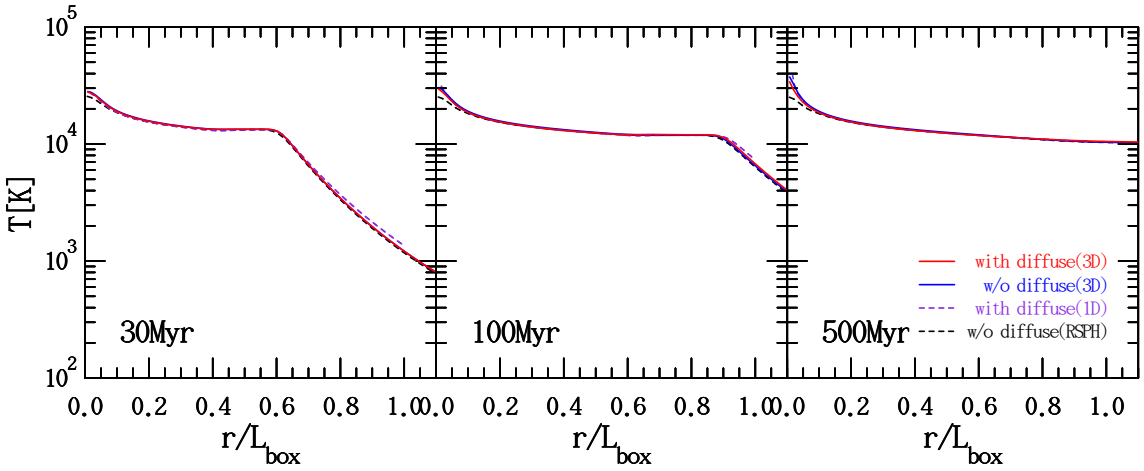

Figure 5.4: Test-2: Same as Figure 5.3 but shows the gas temperature profiles.

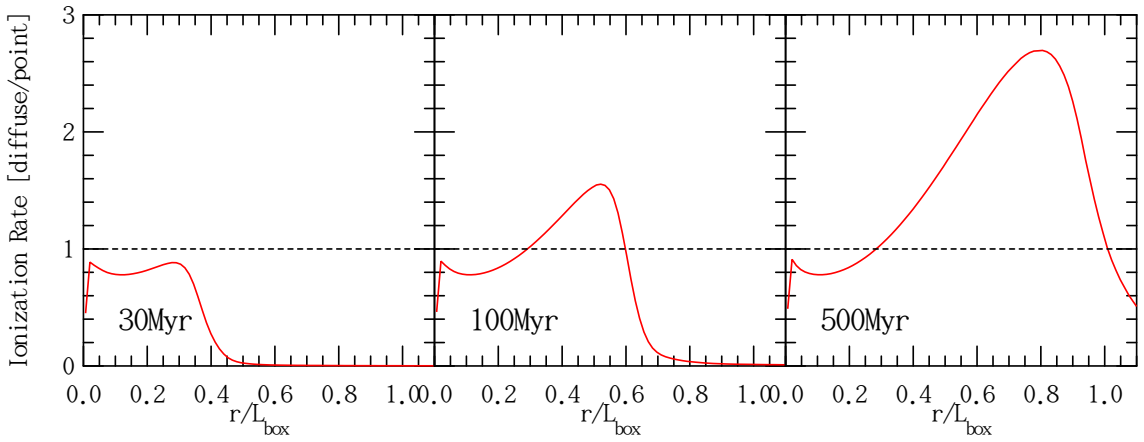

Figure 5.5: Test-2: Radial profiles of the ratio of the ionization rate by the diffuse source RT and the point source RT at $t = 30\,\mathrm{Myr}$, 100 Myr and 500 Myr. The dotted lines indicate the same ratio of Γ by the diffuse and point source RT.

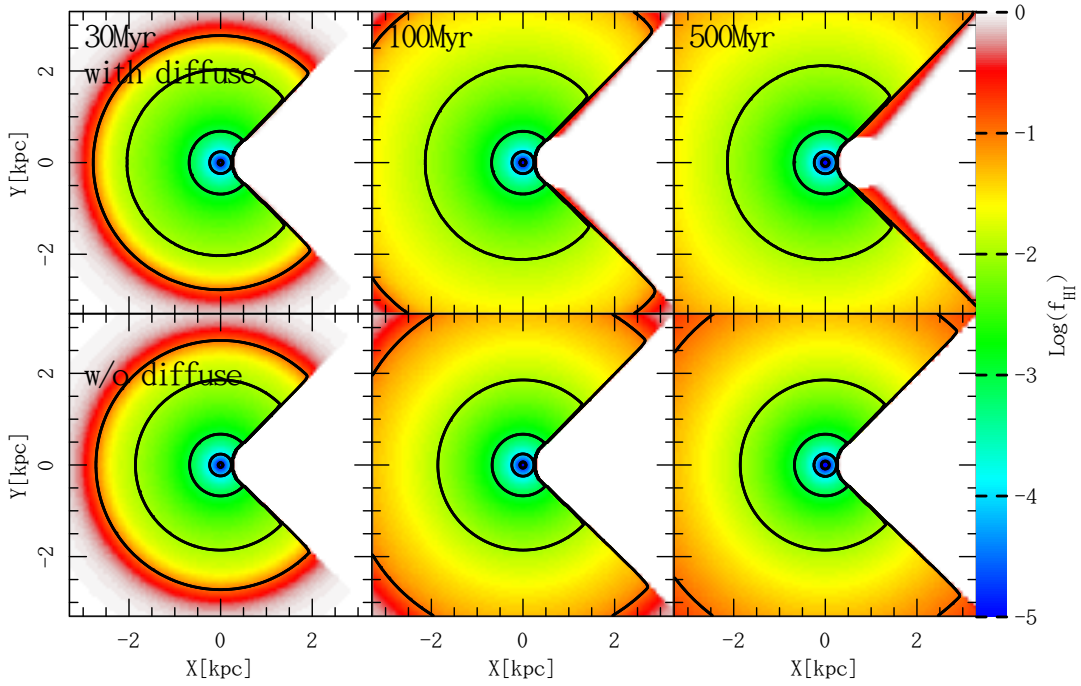

Figure 5.6: Test-2: Maps of neutral fraction of hydrogen in the mid-plane of the simulation box at $t = 30\,\mathrm{Myr}$, 100 Myr and 500 Myr. The lower and upper panels show the results without and with the diffuse RT, respectively. The ambient and clump gas density is $n_\mathrm{H} = 10^{-3}\,\mathrm{cm}^{-3}$ and $n_\mathrm{c} = 2.0\times10^{-1}\,\mathrm{cm}^{-3}$, respectively.

of the point radiation source is also the same as that in Test-2. In this test, we set 256^3 mesh grids and $N_\mathrm{side} = 8$.

Figure 5.6 and 5.7 show maps of the neutral fraction of hydrogen and the temperature in the source-plane of the simulation volume at $t = 30\,\mathrm{Myr}$, 100 Myr and 500 Myr. One can see that the ionizing photons are strongly absorbed by the dense gas clump and conical shadows are formed behind the gas clump in the both runs with and without the effect of recombination RT. In the run with the diffuse RT (upper panels of Figure 5.6), the recombination photons emitted by the ionized gas gradually ionize the neutral gas behind the dense gas clump. On the other hand, in the run without the diffuse RT, the boundaries of neutral and ionized regions are kept distinct because of the lack of recombination photons.

We also conduct a RT simulation with the same initial condition except that the number density of the ambient gas is 10 times lower than the previous run, $n_\mathrm{H} = 10^{-4}\ \mathrm{cm}^{-3}$. In this run, the mean free path of recombination photons is longer than that in the previous run. Therefore, as shown in Figures 5.8 and 5.9, the recombination radiation can be transfered much deeper from the interface of the conical shadow compared with the results in the previous run.

5.2.2 Angular Resolution

In this test, we also perform runs with various angular resolution parameter N_side in the RT calculation of diffuse photons to see the effect of angular resolution. Figure 5.10 shows shadowing test maps of neutral fraction of hydrogen in the mid-plane of the simulation box at $t = 30\,\mathrm{Myr}$ with angular resolution parameter N_side of 16, 4 and 1. The results with $N_\mathrm{side} = 16$ and 4 are in good agreement with each other,

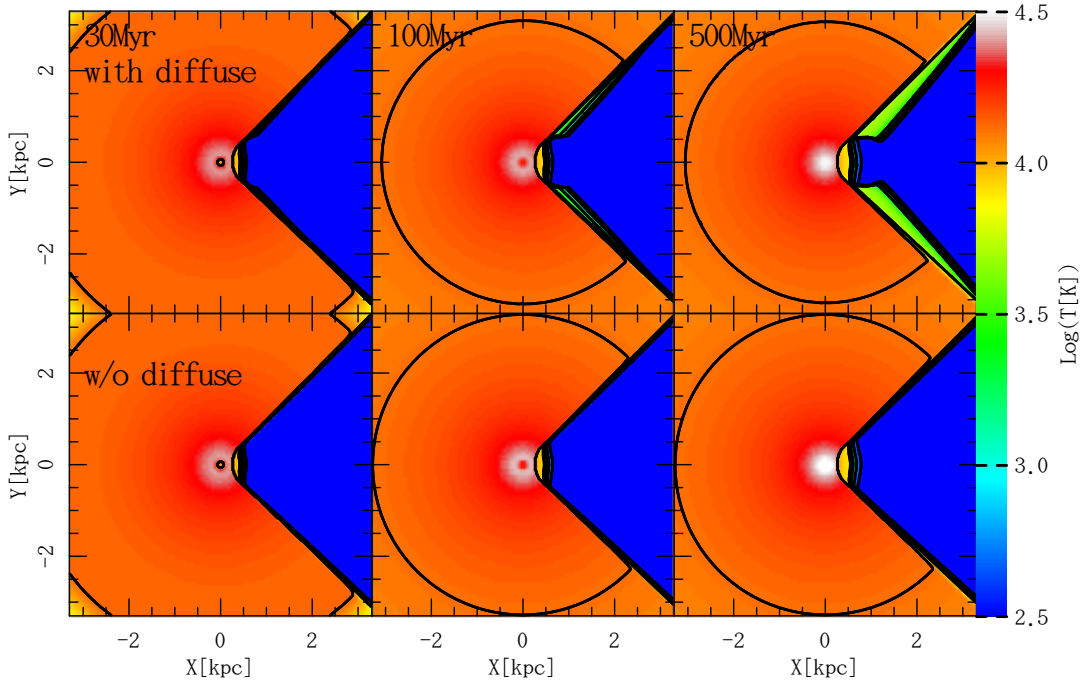

Figure 5.7: Test-2: Same as Figure 5.6 but shows the gas temperature maps in the mid-plane of the simulation box. The initial ambient and clump gas temperature are set to $T = 100\,\mathrm{K}$.

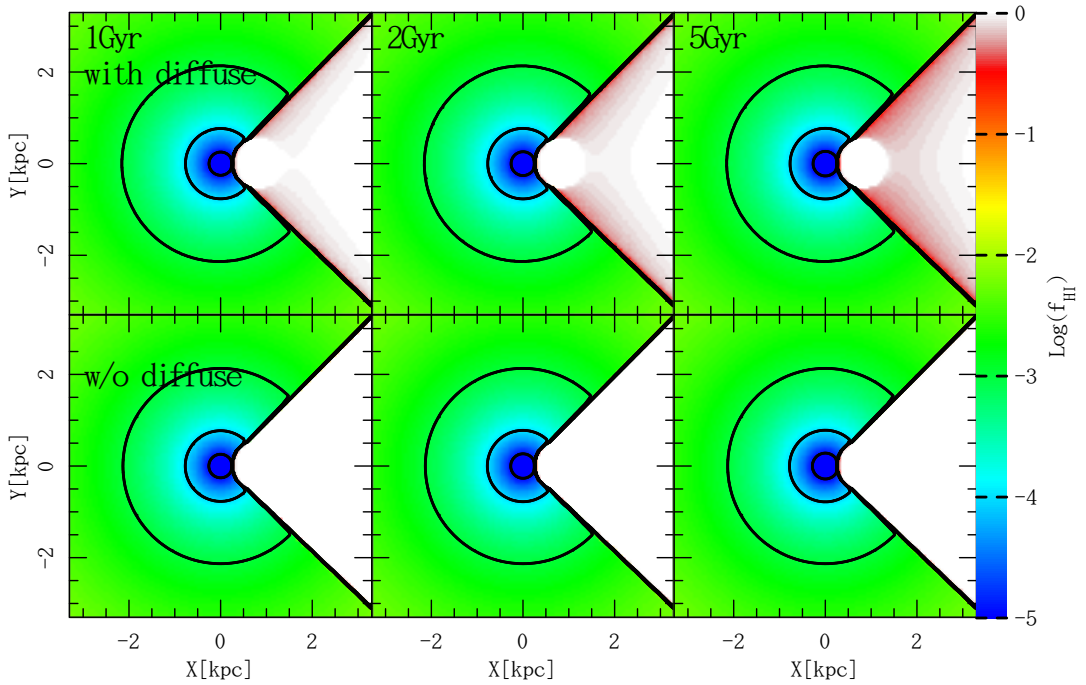

Figure 5.8: Test-2: Same as Figure 5.6 but shows the results with the ambient gas density of $n_{\mathrm{H}} = 10^{-4}\,\mathrm{cm}^{-3}$.

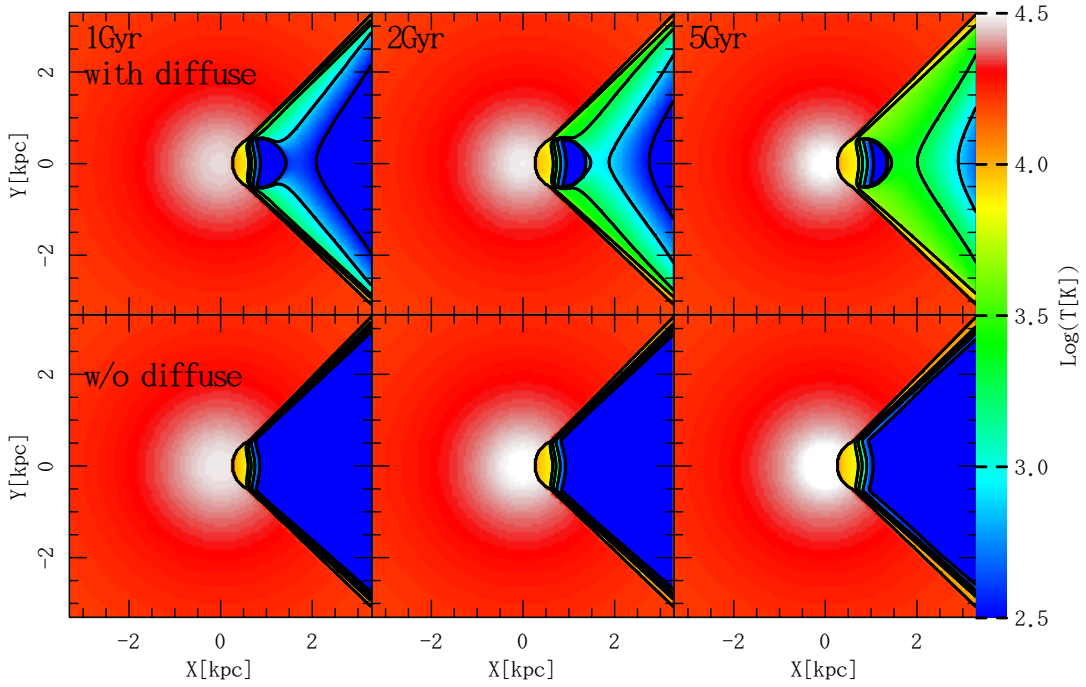

Figure 5.9: Test-2: Same as Figure 5.8 but shows the gas temperature maps in the mid-plane of the simulation box. The initial ambient and clump gas temperature is $T = 100\,\mathrm{K}$.

indicating that the angular resolution with $N_{\rm side} = 4$ is sufficient for the current RT calculations. The results with $N_{\rm side} = 1$, however, have spurious features in the map of neutral fraction. These numerical artifacts can be ascribed to the low angular resolution of light-rays by the comparison of the mean free path of the diffuse recombination photons and $N_{\rm side}\Delta H$. As described in § 5.2.1, the mean free path of the diffuse photons should be sufficiently smaller than $N_{\rm side}\Delta H$ to compute the RT of diffuse photons accurately. For the recombination photons emitted by ionized hydrogens in the current setup, the mean free path in the neutral ambient gas is estimated as

$$\lambda_{\rm mfp} = \frac{1}{n_{\rm HI}\sigma_{\rm HI}(\nu_0)} = 51.4 \left(\frac{n_{\rm HI}}{10^{-3}{\rm cm}^{-3}}\right)^{-1} {\rm pc}, \tag{5.3}$$

and the mesh spacing is $\Delta H = 6.6\,{\rm kpc}/128 = 51.5\,{\rm pc}$. Thus, it is quite natural to have strong numerical artifacts in the results with $N_{\rm side} = 1$, because the mean free path is almost equal to $N_{\rm side}\Delta H$, and the condition for the accurate RT calculation ($\lambda_{\rm mfp} \ll N_{\rm side}\Delta H$) is not satisfied.

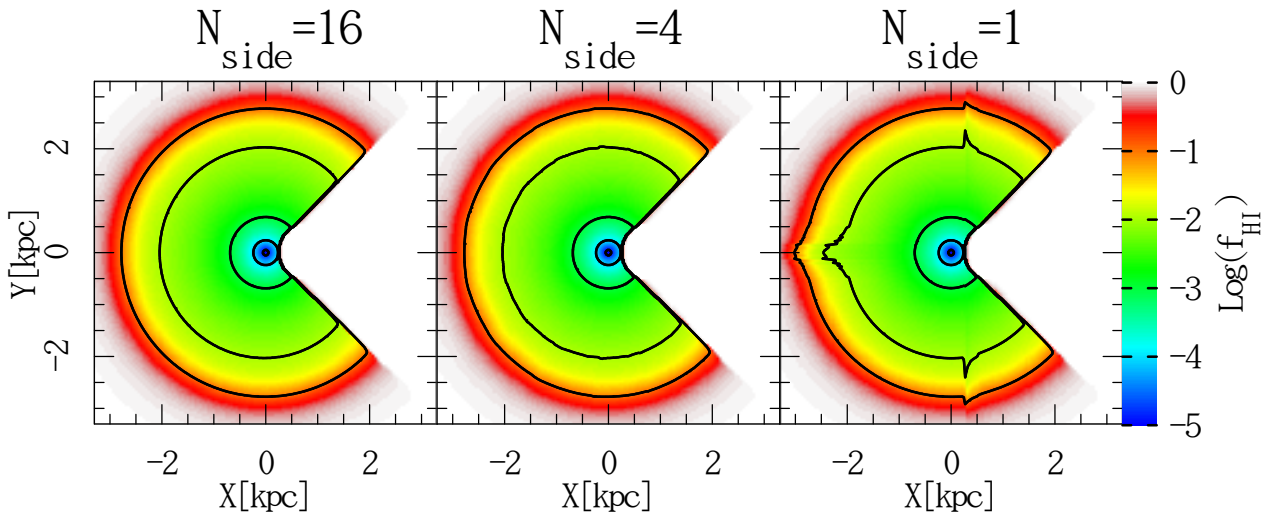

Figure 5.10: Test-2: Maps of neutral fraction of hydrogen in the mid-plane of the simulation box at $t = 30\,\mathrm{Myr}$ for different angular resolution parameter, $N_{\mathrm{side}} = 16$, 4 and 1 from left to right.

5.3 Test-3 : Ionization front trapping and shadowing by a dense clump

The third test computes the transfer of ionizing radiation incident to a face of the rectangular simulation box and the propagation of ionized region into a spherical dense clump. This test is indentical to the Test-3 in Iliev et al. (2006). The size of the simuation box is 6.6 kpc, and hydrogen number density and initial temperature are set to $n_{\rm H} = 2 \times 10^{-4}\,{\rm cm}^{-3}$ and $T = 8000\,{\rm K}$, except that a spherical dense clump with a radius of 0.8 kpc located at 1.7 kpc apart from the center of the simulation volume has a uniform hydrogen number density of $n_{\rm H,c} = 200\,n_{\rm H} = 0.04\,{\rm cm}^{-3}$ and a temperature of $T_c = 40\,{\rm K}$. The ionizing radiation has the blackbody spectrum with a tempearature of $T = 10^5\,{\rm K}$ and constant ionizing photon flux of $F = 10^6\,{\rm s}^{-1}{\rm cm}^{-2}$ at a boundary of the simulation box. The number of mesh grids and angler resolution are set $N_m = 128^3$ and $N_{\rm side} = 16$.

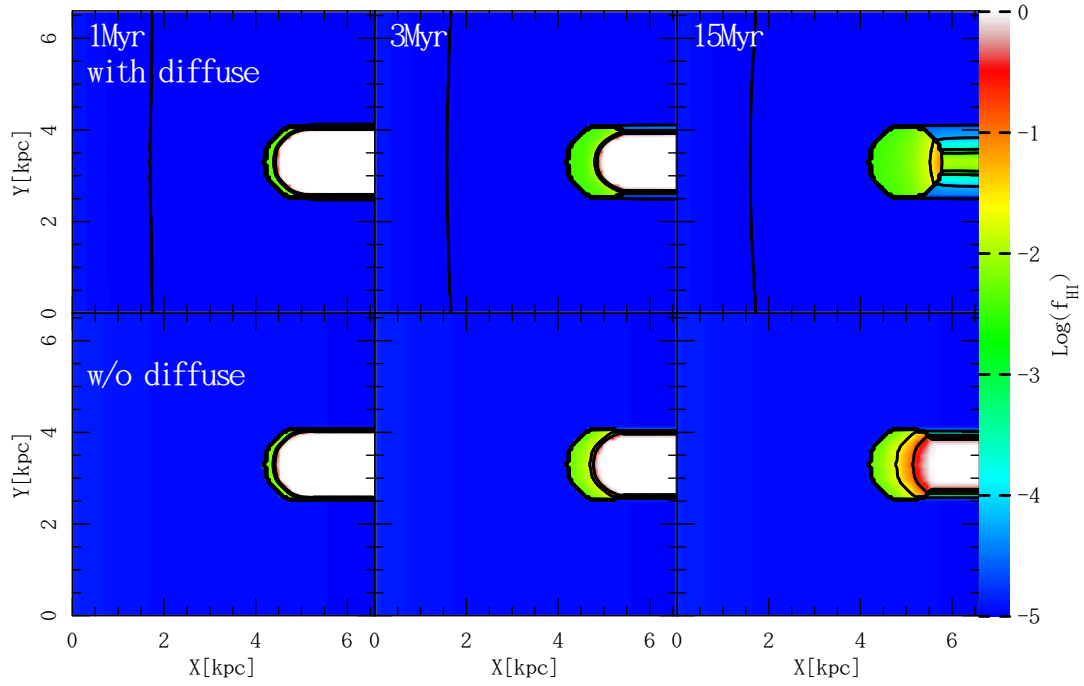

Figure 5.11: Test-3: Maps of neutral fraction of hydrogen in the mid-plane of the simulation box at $t = 1\,{\rm Myr}, 3\,{\rm Myr}$ and $15\,{\rm Myr}$. The upper and lower panels show the results with and without the diffuse RT, respectively.

Figures 5.11 and 5.12 shows the maps of hydrogen neutral fraction and gas temperature in the mid-plane of the simulation volume at $t = 1\,{\rm Myr}, 3\,{\rm Myr}$ and $15\,{\rm Myr}$ from left to right, where the ionizing photons enter from the left boundary of the figures. We show the results with and without the diffuse RT in the upper and lower panels, respectively.

At $t = 1\,{\rm Myr}$, the ionization front enters the spherical clump and a cylindrical shadow is formed behind the clump. At $t = 3\,{\rm Myr}$ and $15\,{\rm Myr}$, the spherical clump is slightly ionized and the boundary of the shadow is ionized and photo-heated by the hard photons which penetrate the edge of the clump. These overall ionization and temperature structures without the diffuse RT are consistent with the ones presented in Iliev et al. (2006). The effect of the recombination radiation is clearly seen in the results at $15\,{\rm Myr}$, in which the cylindrical shadow is significantly ionized and heated by the recombination photons

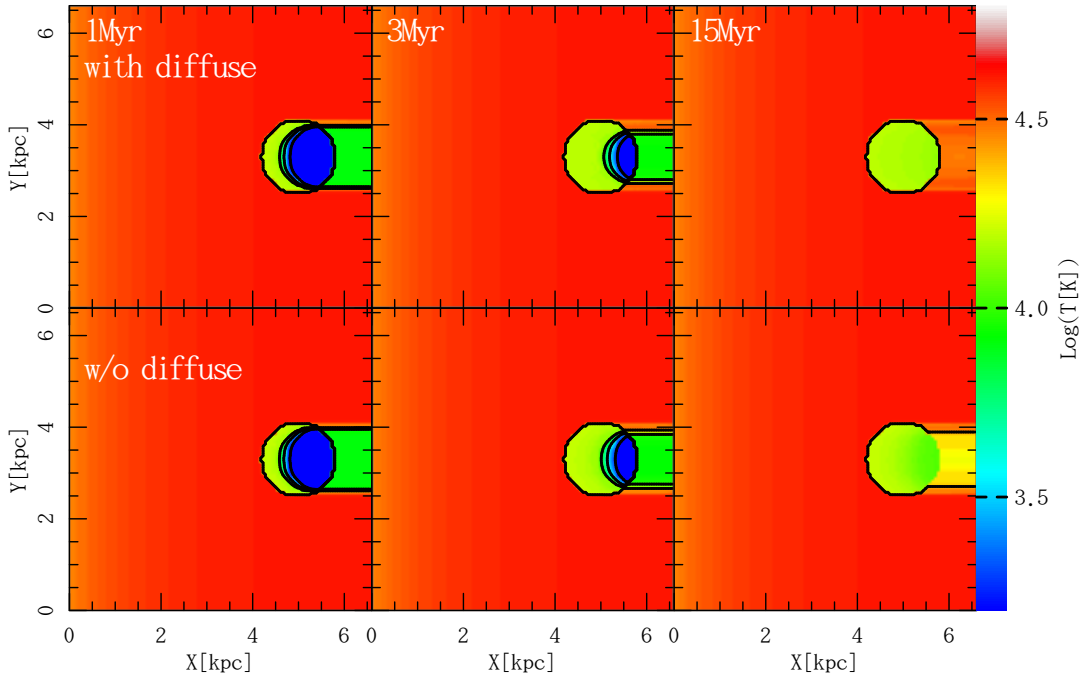

Figure 5.12: Test-3: Same as Figure 5.11 but shows the gas temperature maps in the mid-plane of the simulation box.

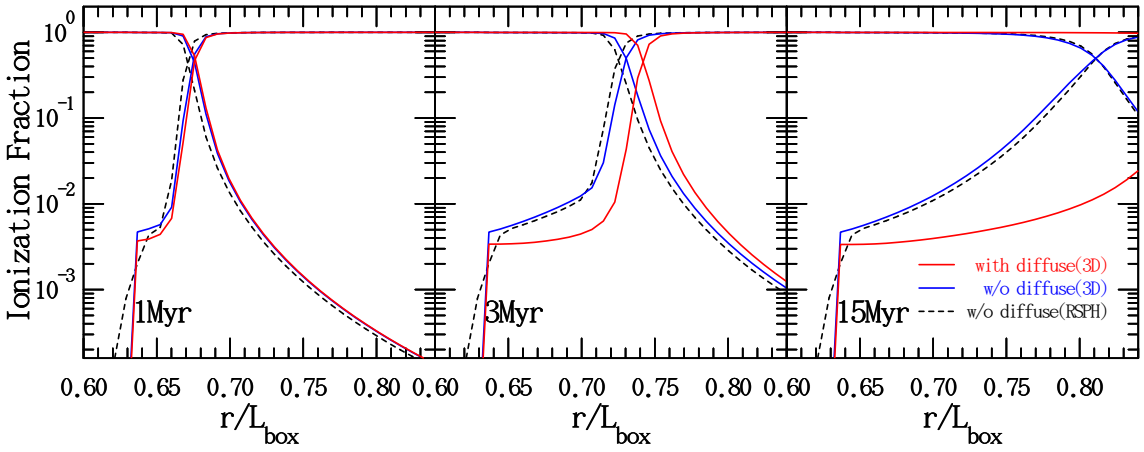

Figure 5.13: Test-3: Profiles of hydrogen neutral and ionized fractions along the axis of symmetry at $t = 1\,\mathrm{Myr}$, $3\,\mathrm{Myr}$ and $15\,\mathrm{Myr}$. Red (ARGOT+ART, Case-A) and blue (ARGOT, Case-B) solid lines indicate the results with and without the diffuse RT, respectively. Black dashed lines indicate result without the diffuse RT by RSPH (Susa, 2006).

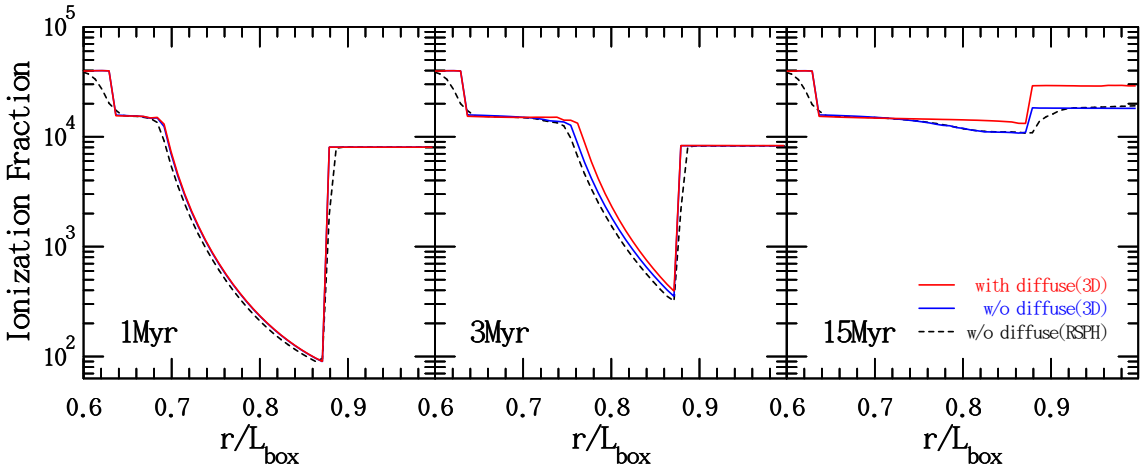

Figure 5.14: Test-3: Same as Figure 5.13 but shows the gas temperature profiles.

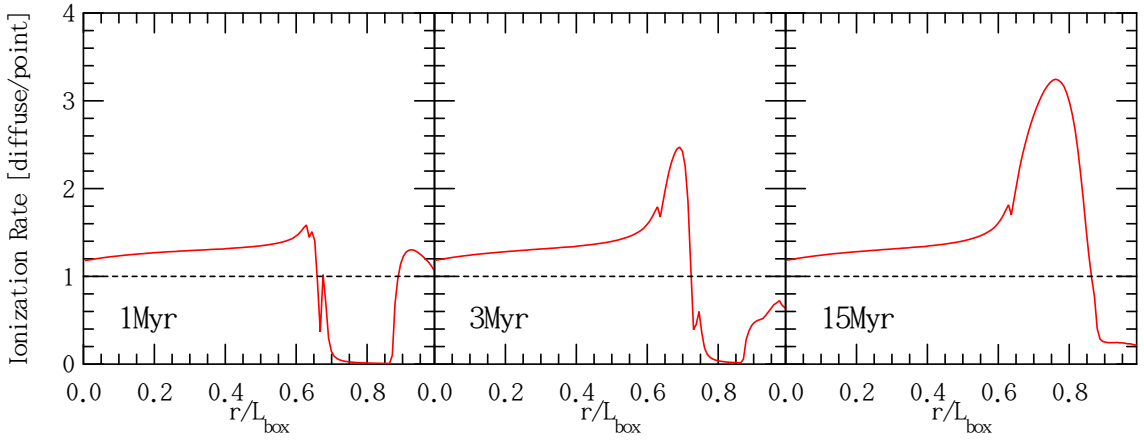

Figure 5.15: Test-3: Profiles of the ratio of the ionization rate by the diffuse and point source RT along the axis of symmetry at $t = 1\,\mathrm{Myr}$, $3\,\mathrm{Myr}$ and $15\,\mathrm{Myr}$. The dotted lines indicate the same ratio of Γ by the diffuse and point source RT.

emitted at the ambient ionized region.

Figures 5.13 and 5.14 shows the profiles of ionized fraction and gas temperature along the axis of symmetry at $t = 1\,\mathrm{Myr}, 3\,\mathrm{Myr}$ and $15\,\mathrm{Myr}$, which is compared with Figures 27 and 28 in Iliev et al. (2006). The results without the diffuse RT are consistent with the ones in Iliev et al. (2006). The effect of the recombination radiation is siginificant at $t = 3\,\mathrm{Myr}$ and $15\,\mathrm{Myr}$ in the ionized fraction profiles, in which the recombination photons accelerate the propagation of the ionization front in the run with the diffuse RT.

5.4 Test-4 : HII region expansion in cosmological static density field by multiple ionization sources

The fourth test shows the ionization front of multiple point radiating sources in a cosmological static density field. We adopt the same initial condition as that of Test-4 in Iliev et al. (2006). The initial condition is made by N-body and gasdynamic simulation performed using the cosmological PM+TVD code by Ryu et al. (1993). We use this initial condition data provided by the official Cosmological Radiative Transfer Codes Comparison Project site. The initial gas temperature is uniformly set to $T = 100\,\mathrm{K}$. The initial ionization state is computed assuming the collisional ionization equilibrium. The ionizing sources are located at the centers of the 16 most massive haloes and have spectra with the effective temperature of $T = 10^5\,\mathrm{K}$, and emit radiation with ionizing photon rate computed as

$$\dot{N}_\gamma = f_\gamma \frac{M\Omega_b}{\Omega_0 m_p t_s}, \tag{5.4}$$

where $f_\gamma = 250$ is the ionizing photons emission per atom during its lifetime, M is the total halo mass, m_p is the proton mass, $t_s = 3\,\mathrm{Myr}$ is the life time of the point sources. We assume the cosmological parameters of $\Omega_0 = 0.27, \Omega_b = 0.043, \Omega_v = 0.73, h = 0.7$. For simplicity, all the sources are assumed to be ignited at the same time. The simulation box size is $0.5h^{-1}$ comoving Mpc. The boundary condition is transmissive. We set up 128^3 mesh grids and adopt $N_{\mathrm{side}} = 16$. The simulation is started from redshift $z = 8.85$.

Figures 5.16 and 5.17 shows the mid-plane of the simulation box of the neutral fraction of hydrogen and the gas temperature at $t = 0.05\,\mathrm{Myr}, 0.2\,\mathrm{Myr}$ and $0.4\,\mathrm{Myr}$ from redshift $z = 8.85$. The upper and lower panels indicate the results with and without the effect of recombination raidation, respectively. One can see that the difference between the runs with and without recombination radiation is little. This is because the hydrogen number density in this test is in the order of $n_{\mathrm{H}} = 10^{-4} - 10^{-7}\mathrm{cm}^{-3}$, and thus the recombination time is around the order of 100 Gyr for $n_{\mathrm{H}} = 10^{-6}\ \mathrm{cm}^{-3}$, which means that the amount of the recombination photons is considerably small compared with direct ionizing photons from point radiating sources.

Figure 5.18 and 5.19 show the histograms of the neutral fraction and the gas temperature at $t = 0.05\,\mathrm{Myr}, 0.2\,\mathrm{Myr}$ and $0.4\,\mathrm{Myr}$. The red solid and blue solid lines indicate the results with and without the effect of recombination radiation, respectively. Since the results by RSPH is not available in this test, we compare our results with ones obtained by C^2-Ray and `CRASH` codes. The magenta dashed lines show the results by C^2-Ray code which is the grid-based short-characteristics ray-tracing method (Mellema et al., 2006). The green dashed lines indicate the results of the CRASH code which is the grid-based RT using the Monte Carlo technique for sampling distribution functions (Maselli et al., 2003). One can see that our results are consistent with those obtained by C^2-Ray and CRASH codes, irrespective of whether the effect of recombination radiation is incorporated.

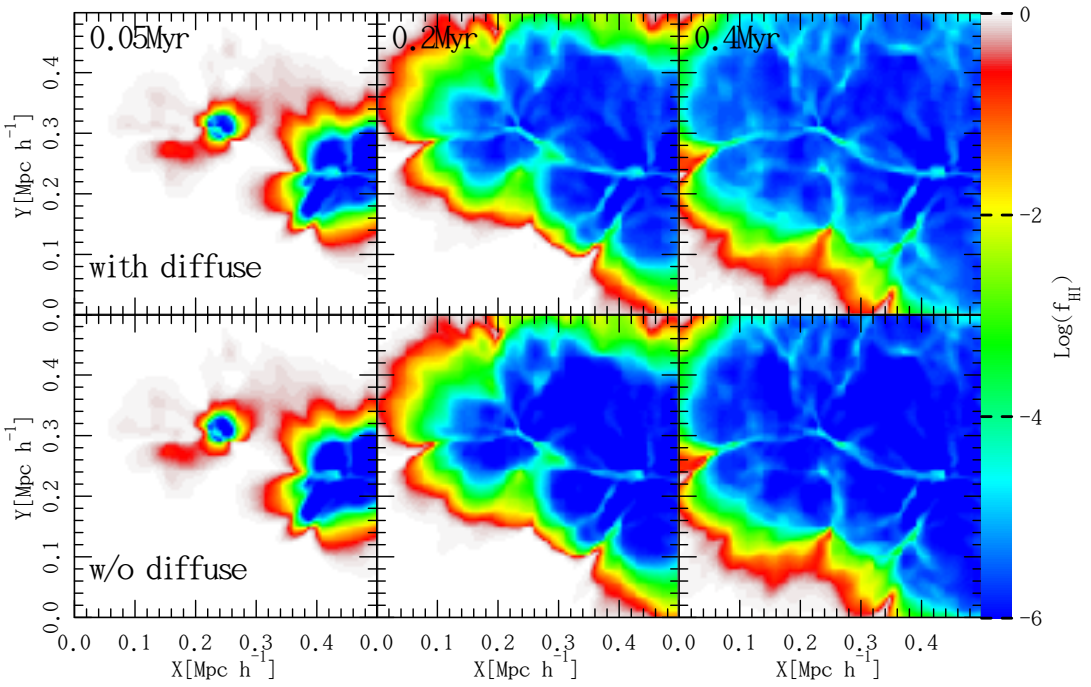

Figure 5.16: Test-4: Maps of neutral fraction of hydrogen in the mid-plane of the simulation box at $t = 0.05\,\mathrm{Myr}$, $0.2\,\mathrm{Myr}$ and $0.4\,\mathrm{Myr}$ from redshift $z = 8.85$. The upper and lower panels show the results with and without the recombination radiation, respectively.

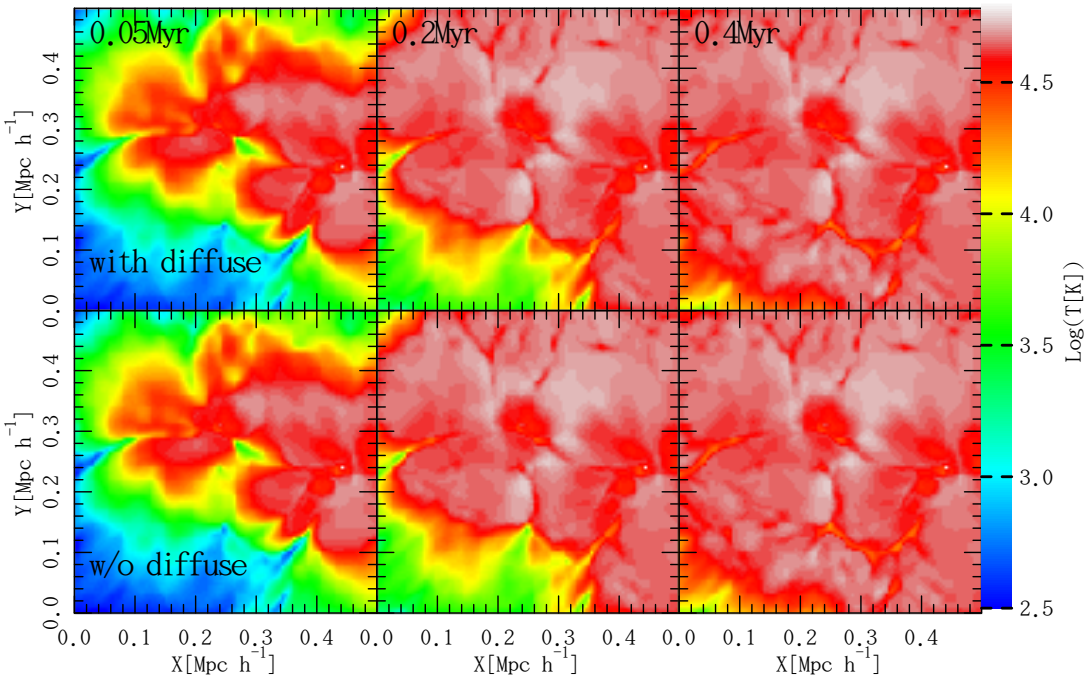

Figure 5.17: Test-4: Same as Figure 5.16 but shows the gas temperature maps in the mid-plane of the simulation box. The initial gas temperature is uniformly set to $T = 100\mathrm{K}$.

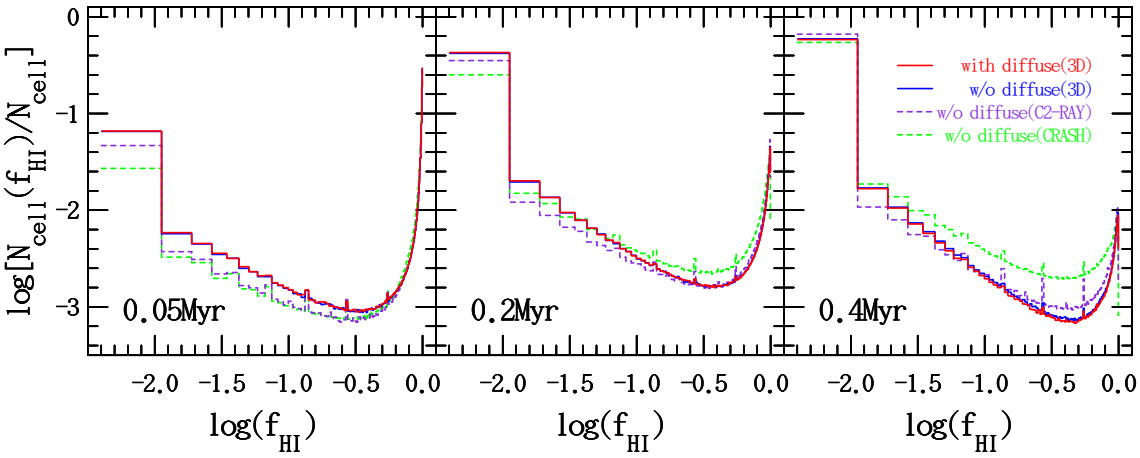

Figure 5.18: Test-4: Histogram of neutral fraction of hydrogen at $t = 0.05$ Myr, 0.2 Myr and 0.4 Myr from redshift $z = 8.85$. Red and blue solid lines indicate the results with and without recombination radiation, respectively. Magenta dashed lines are the reuslts with the short-characteristics code, C^2-Ray, and the green dashed lines are obtained by the CRASH code.

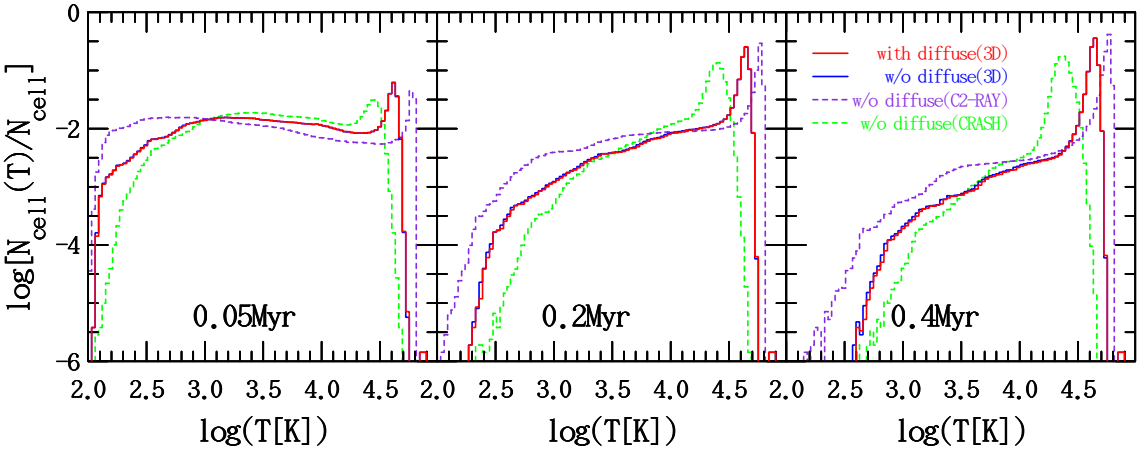

Figure 5.19: Test-4: Same as Figure 5.18 but shows the gas temperature histogram.

5.5 Test-5 : HII region expansion with the Hydrodynamics

This test is the almost same as Test-2 but incorporate the hydrodynamic effect. We adopt the same initial condition as that of Test-5 in Cosmological Radiative Transfer Codes Comparison Project II(Iliev et al., 2009).

The hydrogen number density is uniformly set to $n_{\rm H} = 10^{-3}\,{\rm cm}^{-3}$ and the initial gas temperature is $T = 10^2\,{\rm K}$. The ionizing source emits 5×10^{48} ionizing photons per second and located at a corner of simulation box with a side length of 15 kpc. The initial ionization state is under the collisional ionization equilibrium. This test simulations are carried out with 256^3 mesh grids and the angular resolution parameter of $N_{\rm side} = 8$.

In this test, we have the R-type (rarefied gas) and D-type (dense gas) of ionization fronts (Kahn, 1954). These front structures have two critical speeds which depends on the sound speed in the ionized and neutral regions. The R-type ionization front propagates much faster than the sound speed. The R-type critical speed is given by $v_{\rm R} = 2a_2 - a_1^2/2a_2 \approx 2a_2$. On the other hand, the D-type front propagates slowly. The D-type critical speed is given by $v_{\rm D} = a_2 - (a_2^2 - a_1^2)^{1/2} \approx a_1^2/2a_2$, where $a_1 = (p_1/\rho_1)^{1/2}$ and $a_2 = (p_2/\rho_2)^{1/2}$ are the sound speeds in HI and HII regions, respectively. Since typical sound speeds in HI and HII region are $a_1 \approx 1\,{\rm km/s}$ and $a_2 \approx 10\,{\rm km/s}$, respectivly, we have $v_R \approx 20\,{\rm km/s}$ and $v_D \approx 0.05\,{\rm km/s}$. When $v_{\rm I} \geq v_{\rm R}$, the ionization front is R-type and propagate supersonically in neutral gas region, where $v_{\rm I}$ is given by the $F/n_{\rm H}$, F is the ionization flux of the central source and $n_{\rm H}$ is the number density of hydrogen. When $v_{\rm I} \leq v_{\rm D}$, the ionization front is D-type and propagates in a subsonic speed. These types are determined by the strength of the ionization flux F. Inevitably around the point source the ionization front is always R-type front because the ionization flux is large. As the ionization front propagates, the ionization flux is attenuated due to geometrical and absorption effect and the front transits to the D-type front. When $v_{\rm R} < v_I < v_{\rm D}$, the ionization type is M-type, in which we have a shock front in the HI region and the ionization front is the critical D-type front.

Figure 5.20, 5.21, 5.22, 5.23 and 5.24 show the radial profiles of ionization fraction, gas temperature, hydrogen number density, pressure and Mach number at $t = 10\,{\rm Myr}$, $200\,{\rm Myr}$ and $500\,{\rm Myr}$, respectively. The red solid and blue solid lines indicate the results with and without the effect of recombination radiation, respectively. The black dashed lines depicts the results obtained by RSPH code and are in good agreement with our results without the effect of recombination radiation. The ionization front type at early stage is R-type, and then transits to D-type. The difference between the results with and without recombination radiation is small even at $t = 200\,{\rm Myr}$ and $t = 500\,{\rm Myr}$ compared with the results in Test-2. This can be explained as foloows: the recombination photons come from high ionization regions around point source both in Test-2 and this test. In Test-2, however, the number density around the point source is constant, and thus the eimssion rate of recombination photons corresponding is also nearly constant. On the other hand, in this test, the hydrogen number density in the inner region decreases due to the hydrodynamical effect. As a result, the amount of recombination photons in inner region is about 20% of that in Test-2.

Figure 5.26, 5.27, 5.28, 5.29 and 5.30 show the map of ionization fraction, gas temperature, hydrogen number density, pressure and Mach number at $t = 10\,{\rm Myr}$, $200\,{\rm Myr}$ and $500\,{\rm Myr}$ of the source-plane in the simulation box, respectively. The upper and lower panels show the results with and without the recombination radiation, respectively. This result shows that the difference between the runs with and

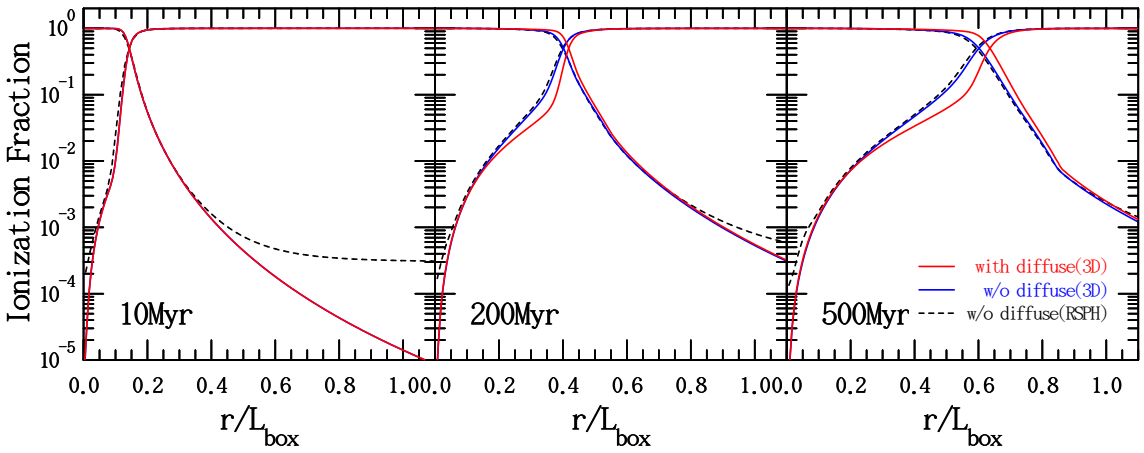

Figure 5.20: Test-5: Radial profiles of ionization fraction of hydrogen at $t = 10\,\mathrm{Myr}$, 200 Myr and 500 Myr. Red and blue solid lines indicate the results with and without the recombination radiation, respectively. Black dashed lines indicate results without diffuse RT by RSPH (Susa, 2006).

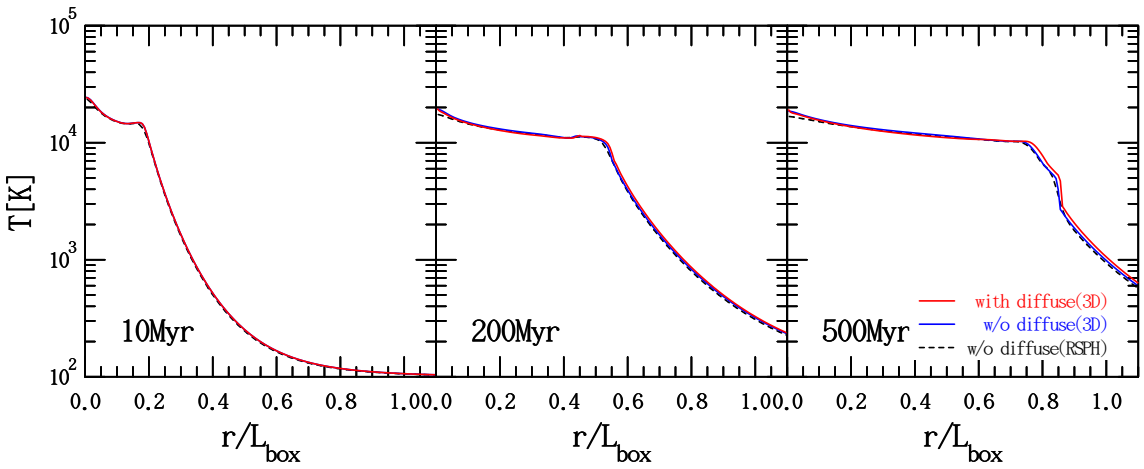

Figure 5.21: Test-5: Same as Figure 5.20 but shows the gas temperature profiles.

without the recombination radiation is small.

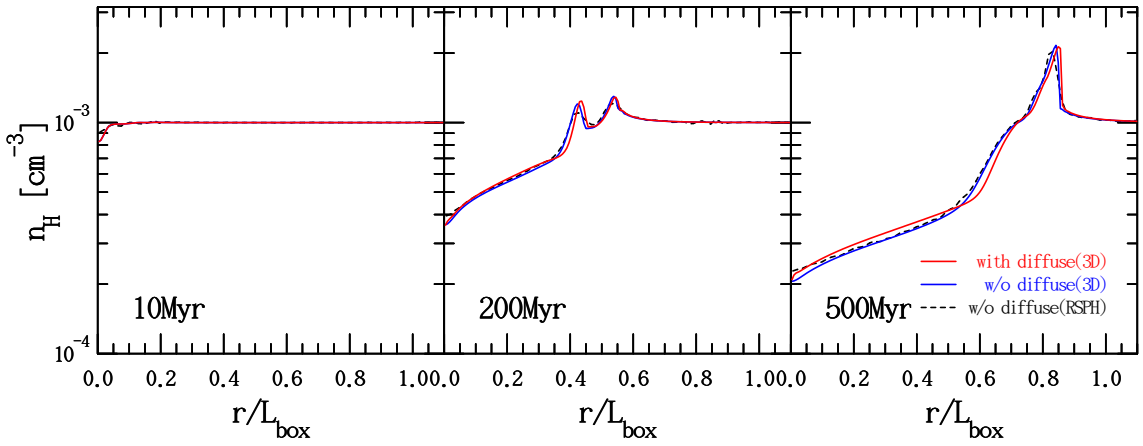

Figure 5.22: Test-5: Same as Figure 5.20 but shows the number density of hydrogen profiles.

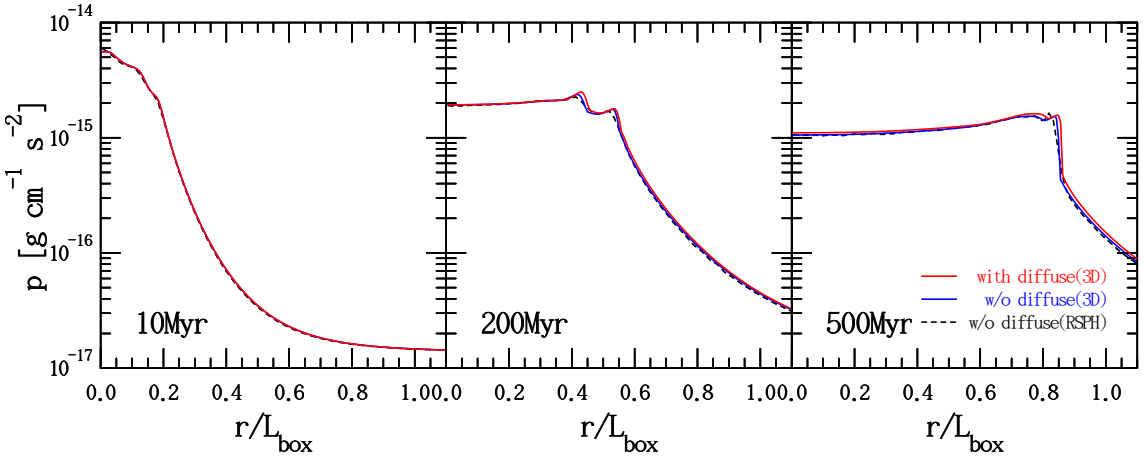

Figure 5.23: Test-5: Same as Figure 5.20 but shows the gas pressure profiles.

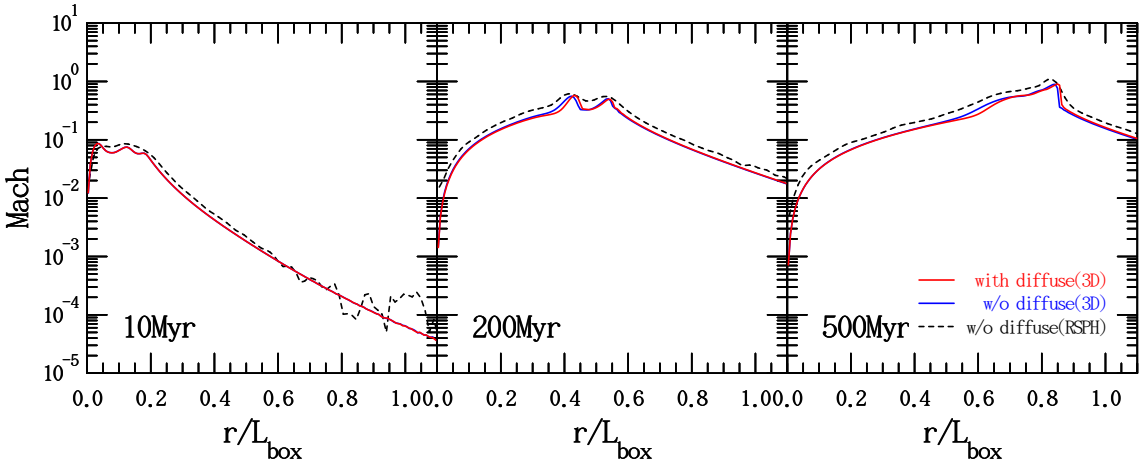

Figure 5.24: Test-5: Same as Figure 5.20 but shows the Mach number profiles.

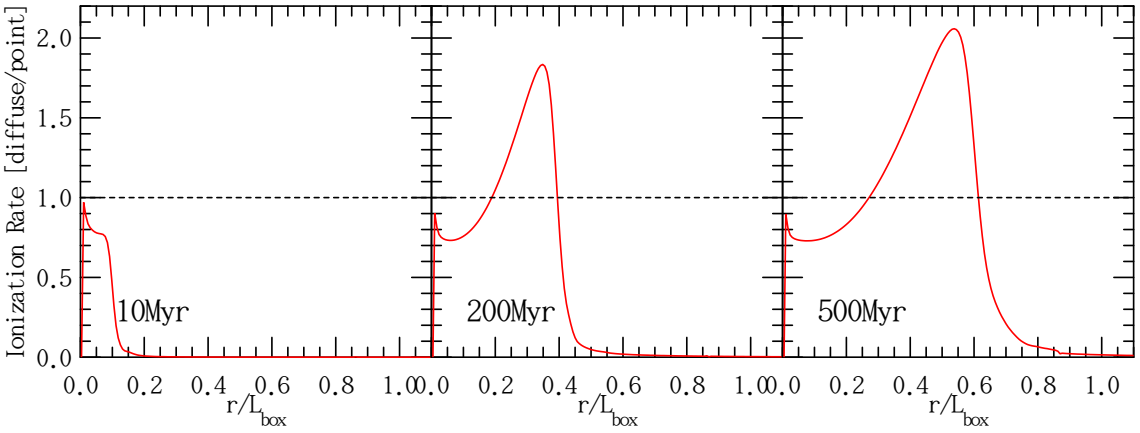

Figure 5.25: Test-5: Radial profiles of the ratio of the ionization rate by the diffuse and point source RT at $t = 10\,\mathrm{Myr}$, $200\,\mathrm{Myr}$ and $500\,\mathrm{Myr}$. The dotted lines indicate the same ratio of Γ by the diffuse and point source RT.

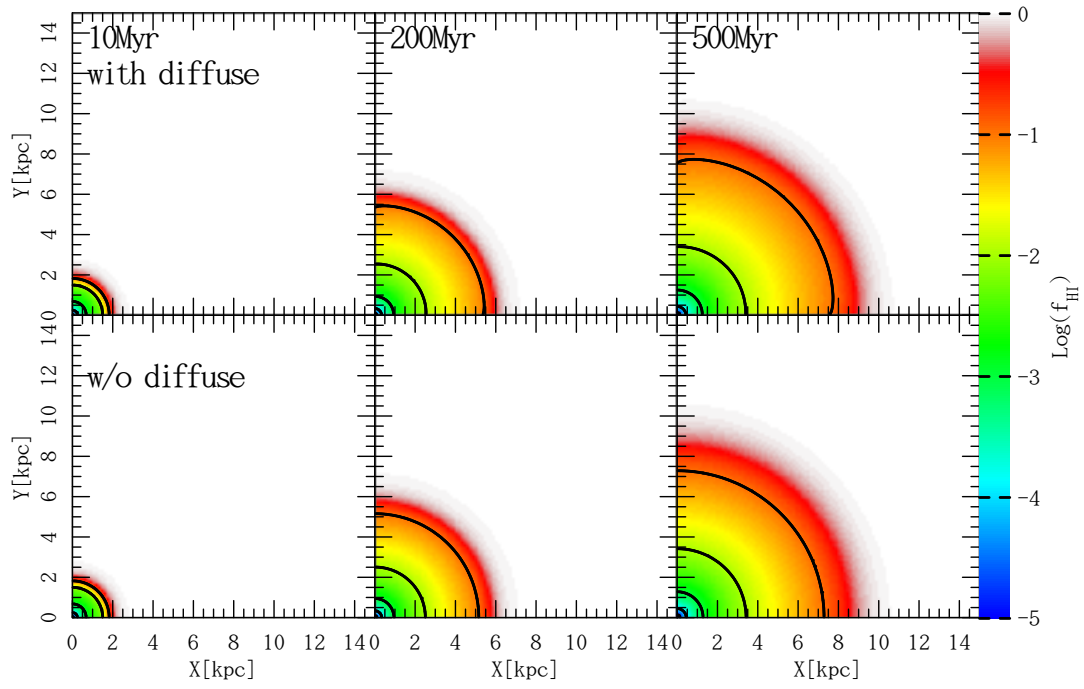

Figure 5.26: Test-5: Maps of neutral fraction of hydrogen in the mid-plane of the simulation box at $t = 10\,\mathrm{Myr}$, $200\,\mathrm{Myr}$ and $500\,\mathrm{Myr}$. The upper and lower panels show the results with and without the recombination radiation, respectively.

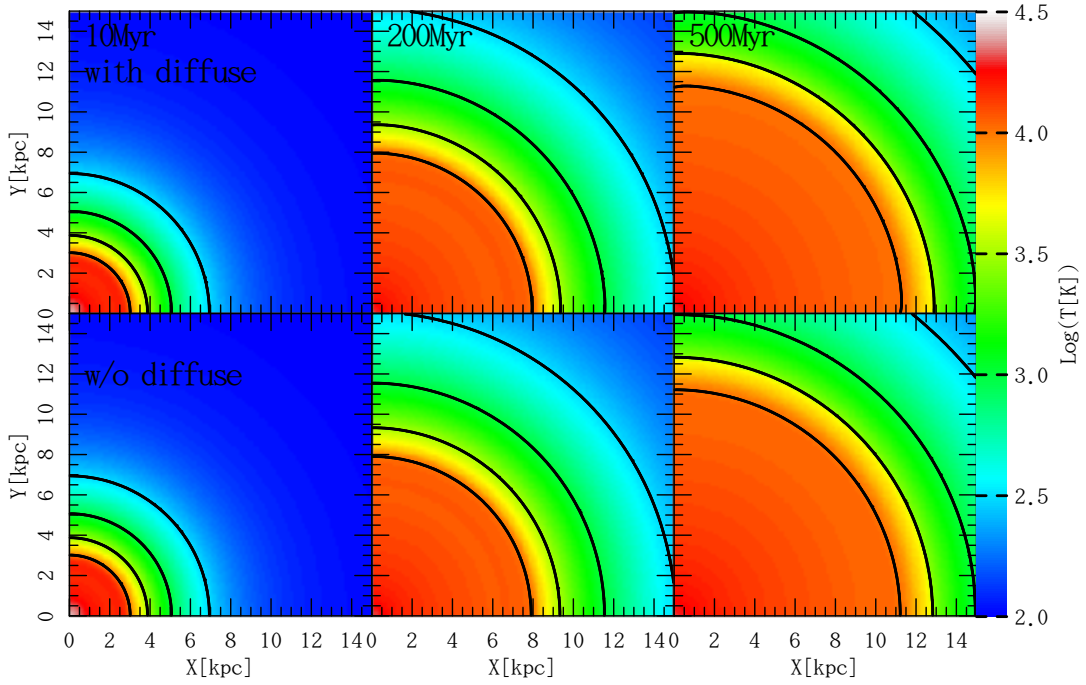

Figure 5.27: Test-5: Same as Figure 5.26 but shows the gas temperature maps in the mid-plane of the simulation box. The initial gas temperature is $T = 100\,\mathrm{K}$.

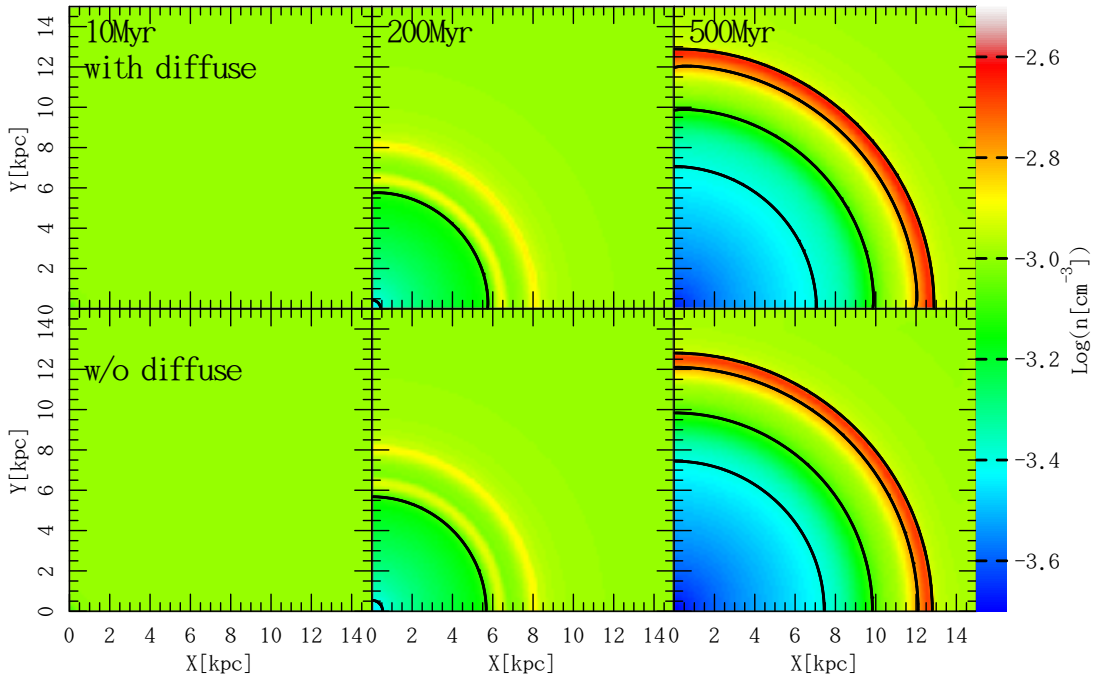

Figure 5.28: Test-5: Same as Figure 5.26 but shows the hydrogen number density maps in the mid-plane of the simulation box.

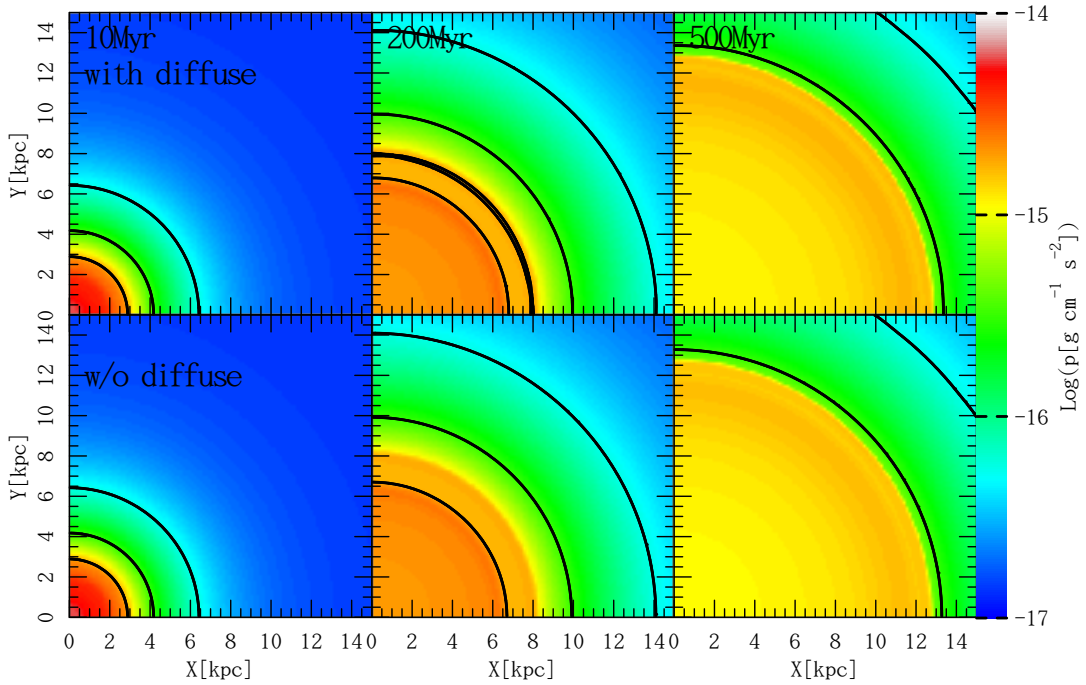

Figure 5.29: Test-5: Same as Figure 5.26 but shows the pressure maps in the mid-plane of the simulation box.

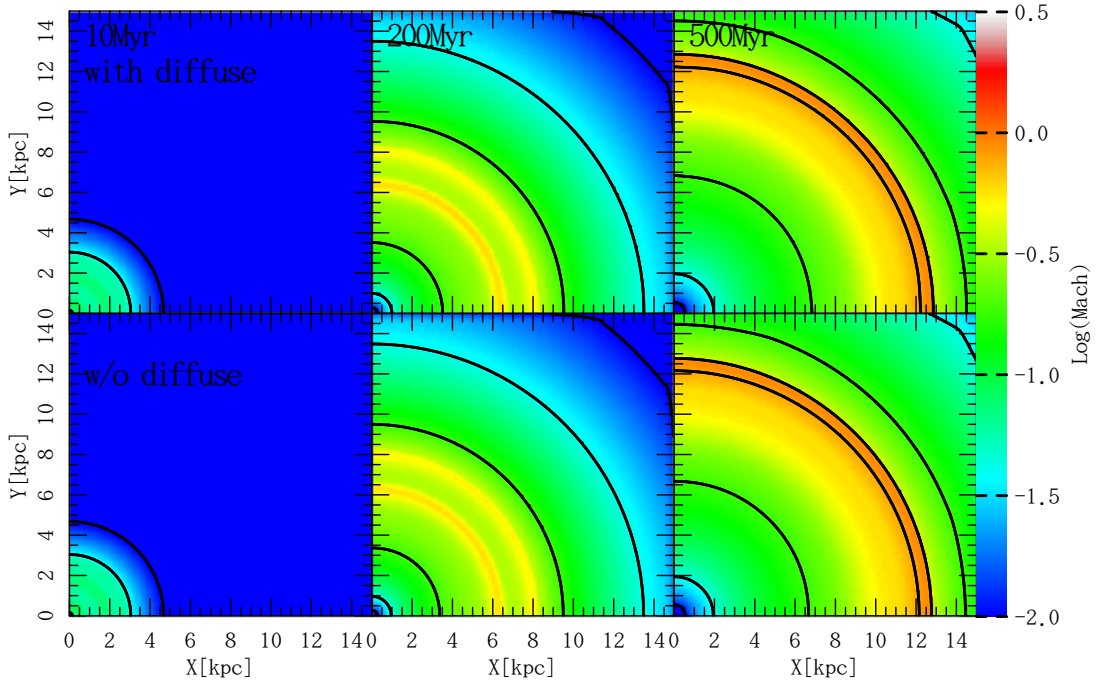

Figure 5.30: Test-5: Same as Figure 5.26 but shows the Mach number maps in the mid-plane of the simulation box.

5.6 Test-6 : HII region expansion in a r^{-2} density profile with the Hydrodynamics

The sixth test is same as Test-5 but density profile is r^{-2} profile and core clump region around the point source. We adopt the same initial condition as that of Test-6 in Iliev et al. (2009).

The hydrogen number density is given by

$$n_{\rm H} = \begin{cases} n_{\rm c} & (r \le r_{\rm c}) \\ n_{\rm c}\,(r/r_{\rm c})^{-2} & (r > r_{\rm c}), \end{cases} \tag{5.5}$$

where $n_{\rm c}$ is the hydrogen number density of a core, $r_{\rm c}$ is a core radius, respectively. And we set these parameter is $n_{\rm c} = 3.2\,{\rm cm}^{-3}$ and $r_{\rm c} = 91.5$ pc. The initial gas temperature is $T = 100\,{\rm K}$ everywhere. The ionizing source emits the blackbody radiation with an effective temperature of $10^5\,{\rm K}$, and 1×10^{50} ionizing photons per second and located at a corner of simulation box with a side length of 0.8 kpc. The core Strömgren radius is 67.3 pc with static gas in $T = 10^4{\rm K}$.

In this test simulations are carried out with 256^3 mesh grids and the angular resolution parameter of $N_{\rm side} = 4$. This simulation test appears the effect of boundary of diffuse RT and spread of HII region expansion can not be represented in spherical. Thus, we calculate with 256^3 mesh grids in twice box scale, and the point source position is a centra of simulation box, and a display of result is 128^3 mesh grids as a source position is a corner of simulation box. Boundary conditions are transmissive for all grid boundaries, practically, the boundary of source plane behave as reflect boundary in diffuse RT.

Figure 5.31 shows the radial profiles of ionization fraction of hydrogen at $t = 0.001\,{\rm Myr}$, $0.005\,{\rm Myr}$ and $0.01\,{\rm Myr}$. This figure is early stage of this simulation and the ionization front within the core yet. The red-solid and blue-solid lines indicate the results with and without the effect of recombination RT, respectively. The initial core radius is about 0.11 in a scale that is normalized by 0.8 kpc. The ionization front with and without diffuse RT coincide because the effect of diffuse RT do not appear yet at $t = 0.001\,{\rm Myr}$. At $t = 0.005\,{\rm Myr}$ and $t = 0.01\,{\rm Myr}$, however, the effect of diffuse RT appears because of the inner region nearby point source is high dense and high ionized. The absolute number of recombination photons emitted from inner region is several hundred larger than Test-5, so the emitted photons from ionized region are expanded the ionization front.

Here, we deform equation 2.19,

$$\mathcal{S}_\nu = \frac{n_{\rm e} n_{\rm HII}}{n_{\rm HI}} \times \frac{\Delta\alpha(T) h\nu}{4\pi\sigma_{\rm HI}\Delta\nu} = n_{\rm H}\frac{f_{\rm HII}^2}{f_{\rm HI}} \times A_{\rm s} \;\; (\nu_0 \le \nu \le \nu_0 + \Delta\nu) \tag{5.6}$$

where we use $n_{\rm HII} = n_{\rm e}$ in a pure hydrogen gas, $n_H, f_{\rm HI}, f_{\rm HII}$ and $A_{\rm s}$ is the number density of hydrogen, neutral, ionization fraction and the factor of $\Delta\alpha(T)h\nu/4\pi\sigma_{\rm HI}\Delta\nu$. Thus, the source function is limit by the hydrogen number density only, if ionization fraction and temperature is a same region. A crucial difference between the Test-5 and Test-6, the number density of around point source region attention to uniform initial number density region. Each tests are little difference in the ionization fraction and temperature around point source region. The effect of the difference of number density of ionized region has appeared larger.

Figures 5.32, 5.33, 5.34, 5.35 and 5.36 show the radial profiles of the ionization fraction of hydrogen, the gas temperature, the hydrogen number density, the gas pressure and Mach number at $t = 3\,{\rm Myr}$, $10\,{\rm Myr}$ and $25\,{\rm Myr}$, respectively. These figure display the stage of ionization front escaped the

core. The black-dashed lines are the results obtained with RSPH code Susa (2006). In the run of our code without diffuse RT and RSPH are a little difference due to the different of chemical reaction rate. In dense region especially, the difference of the reaction rate changes significantly ionization front position. In the run with diffuse RT, the ionization front is expanded more than without diffuse RT due to addition the recombination transfer from the interior of the core. Outer core region, the number of density is decreasing by density slope, so the optical depth become thin too. When the ionization front reaching edge of the core, ionized region expanded rapidly than inner core region. The effect of the recombination photon emission from dense core is large, so the ionization front with diffuse RT is expanded than the run without diffuse RT at later stage.

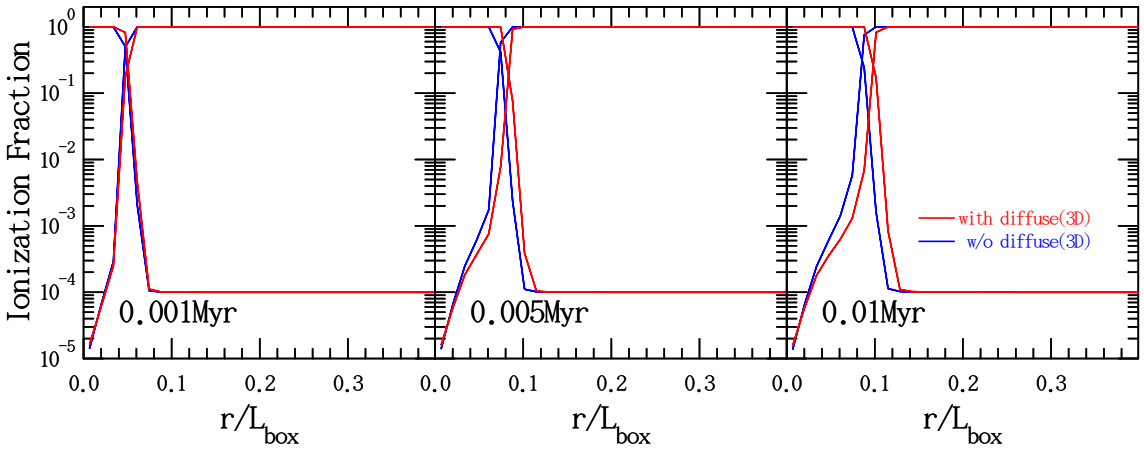

Figure 5.31: Test-6: Radial profiles of ionization fraction of hydrogen at very early stage $t = 0.001$ Myr, 0.005 Myr and 0.01 Myr. Red-solid (ARGOT+ART,Case-A) and blue-solid (ARGOT,Case-B) lines indicate the results with and without the diffuse photon RT, respectively. The horizontal axis is normalized by 0.8 kpc.

Figures 5.38, 5.39, 5.40, 5.41 and 5.42 show the map of the ionization fraction of hydrogen, the gas temperature, the hydrogen number density, the gas pressure and Mach number at $t = 3$ Myr, 10 Myr and 25 Myr of the source-plane in the simulation box, respectively. The upper panels are the results with diffuse RT and lower panels are the results without diffuse RT, respectively. In the run with diffuse RT, fronts has expanded faster than the run without diffuse RT in all figure. This test is appeared the instability of something, see contour of figures. The cause seems to be coupled with the shape of the mesh grid and the D-type instability. Currently, we compute with Cartesian mesh, and the optical depth is changed by the direction in a mesh. For example, the light-ray of the diagonal direction of the mesh is $\sqrt{3}$ times longer than the parallel direction. This problem disappears when the light-ray pass through a several of mesh, but appears when the light-ray pass through few of mesh in the mesh close to the point source. In addition, D-type instability appears too. This is the instability with respect to the shock wave front and ionization front. In this test, the ionization front wave is distorted by shape of mesh and shock front also be distorted by ionization front. If using Cartesian mesh, it is no fundamental solution, however, these figures are able to hide instability by using the photon conserving method or Γ and $\mathcal{H}$ smoothing. If no using these technique, the instability appears more violently. In generally, this D-type instability is generating a real physical phenomenon by the perturbation of density in the shock wave and ionization front. However this non perturbation test should not be appearing the D-type instability.

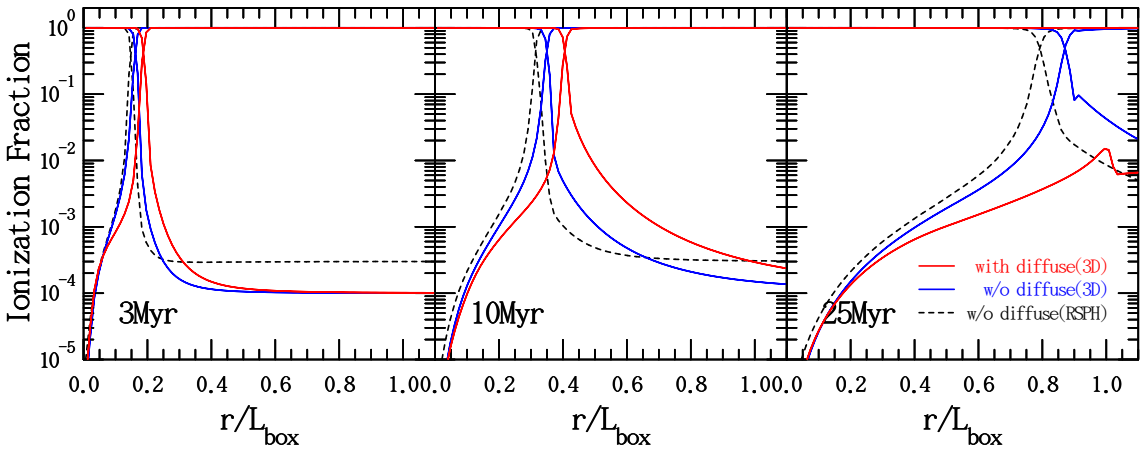

Figure 5.32: Test-6: Radial profiles of ionization fraction of hydrogen at $t = 3\,\mathrm{Myr}$, 10 Myr and 25 Myr. Red (ARGOT+ART,Case-A) and blue (ARGOT,Case-B) solid lines indicate the results with and without the diffuse RT, respectively. Black dashed lines indicate result without diffuse RT by RSPH (Susa, 2006).

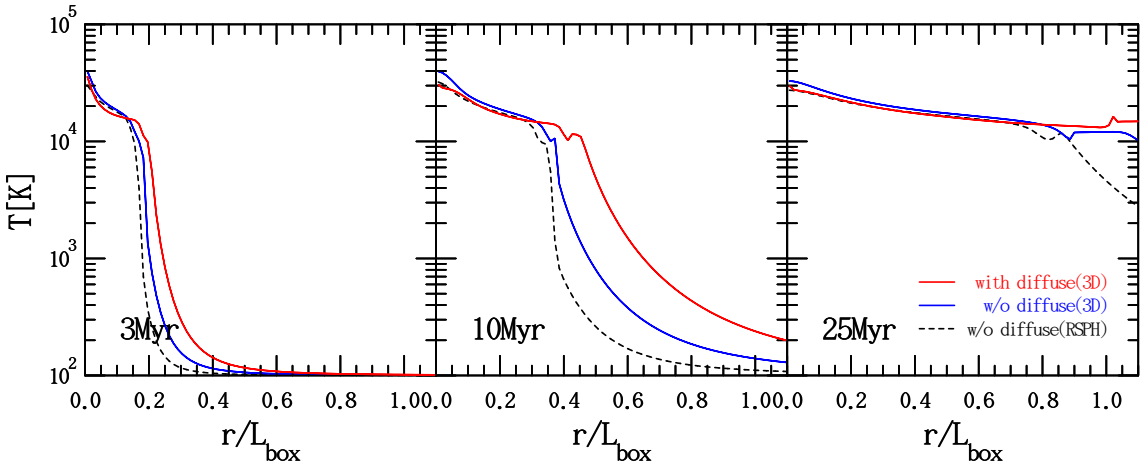

Figure 5.33: Test-6: Same as Figure 5.32 but shows the gas temperature profiles.

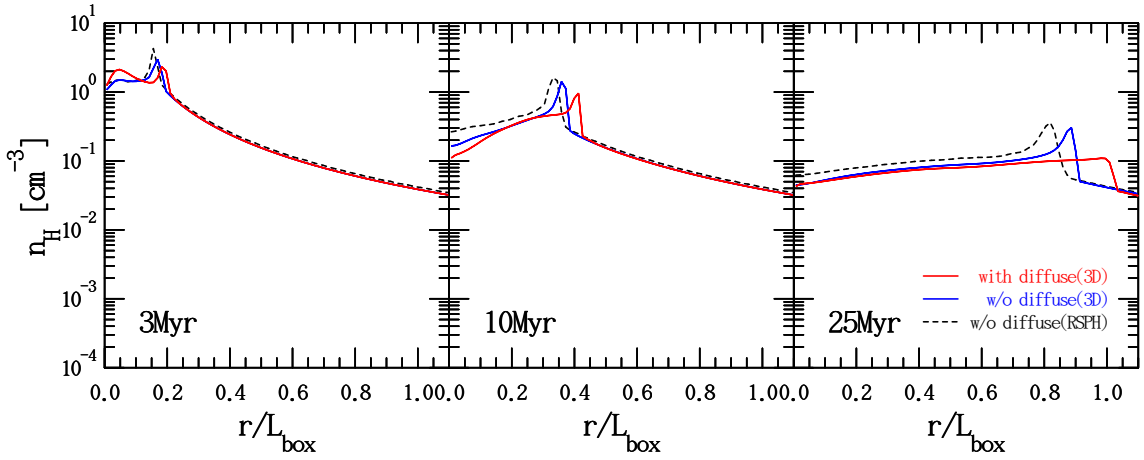

Figure 5.34: Test-6: Same as Figure 5.32 but shows the number density of hydrogen profiles.

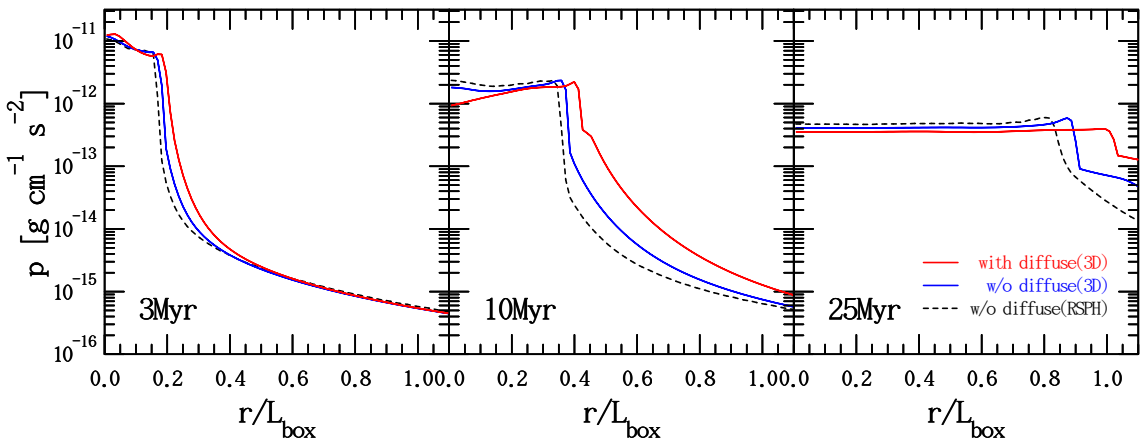

Figure 5.35: Test-6: Same as Figure 5.32 but shows the gas pressure profiles.

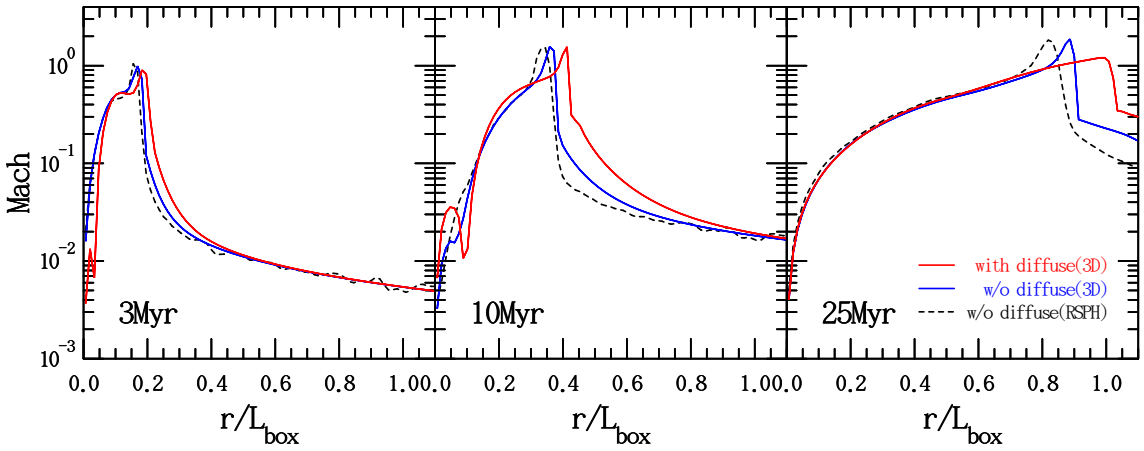

Figure 5.36: Test-6: Same as Figure 5.32 but shows the Mach number profiles.

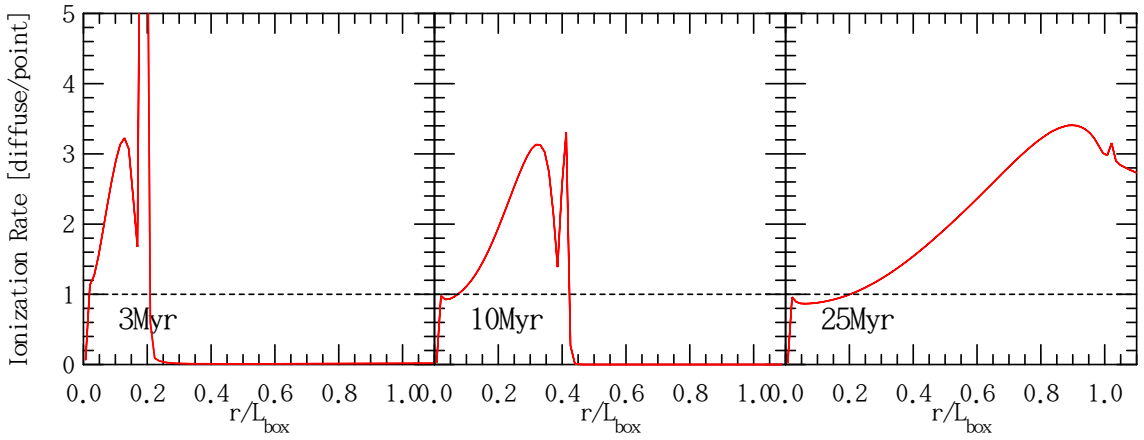

Figure 5.37: Test-6: Radial profiles of the ratio of the ionization rate by the diffuse source RT and the point source RT at $t = 3\,\mathrm{Myr}$, $10\,\mathrm{Myr}$ and $25\,\mathrm{Myr}$. The dotted lines indicate the same ratio of Γ by the diffuse and point source RT.

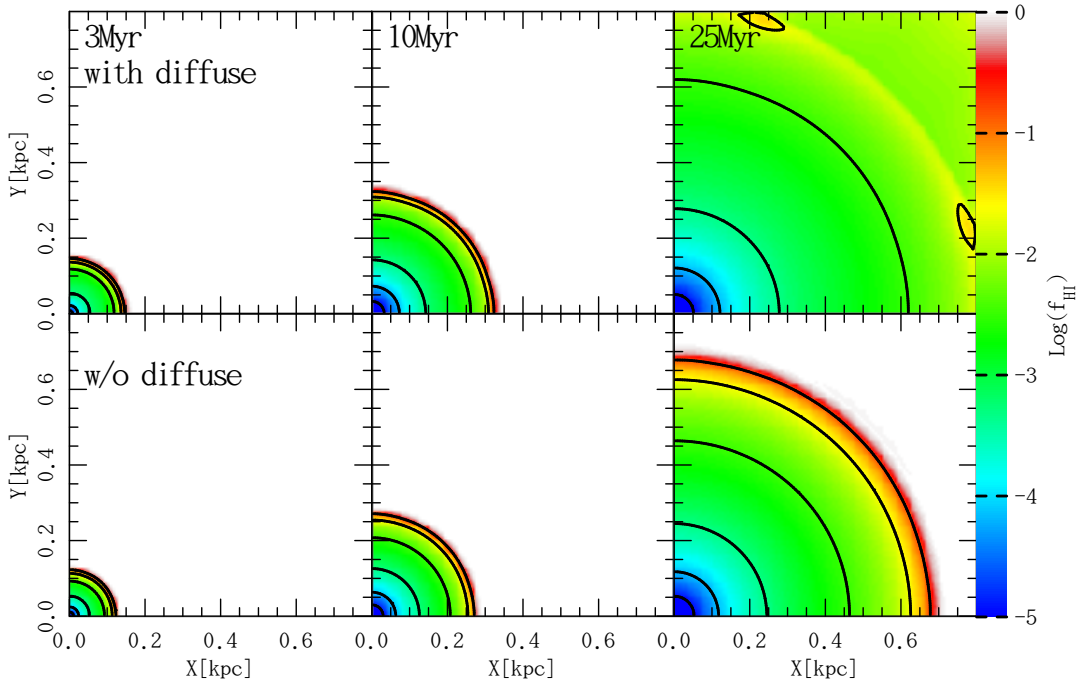

Figure 5.38: Test-6: Maps of neutral fraction of hydrogen in the mid-plane of the simulation box at $t = 3\,\mathrm{Myr}$, 10 Myr and 25 Myr. The lower and upper panels show the results without and with the diffuse photon RT, respectively.

The on-the-spot approximation using Case-B condition calculation can not express to the recombination photon RT from dense and high ionized region. On-the-spot approximation calculation correct only in the situation of optical thick as dense and almost neutrally region. Such calculations have gone to underestimate the ionization effect without diffuse photon RT.

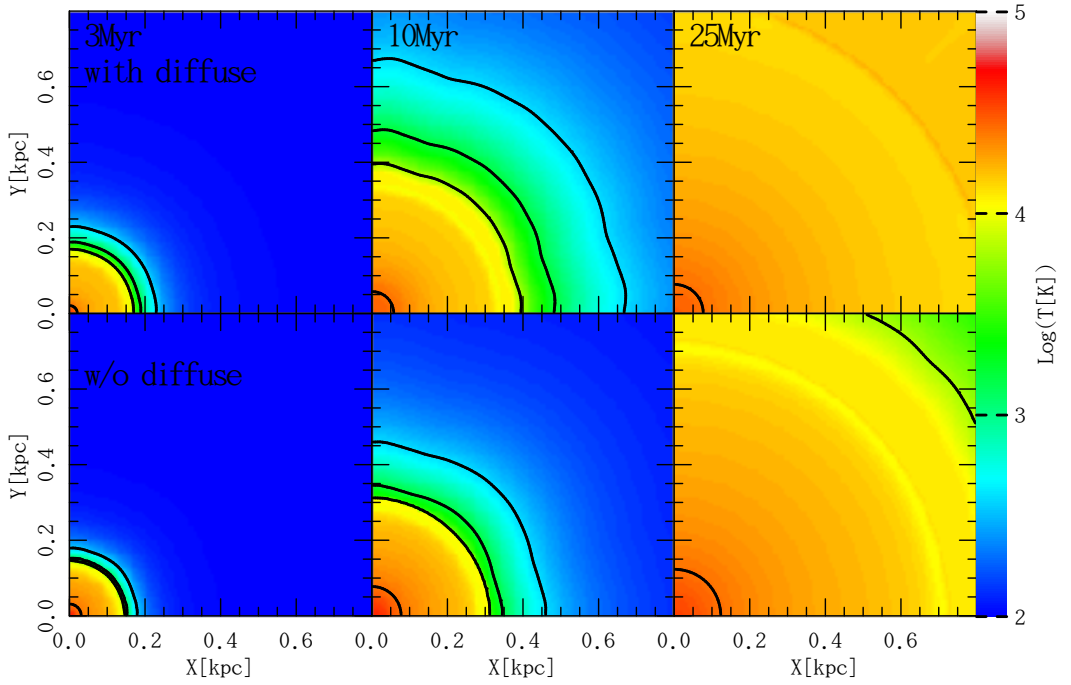

Figure 5.39: Test-6: Same as Figure 5.38 but shows the gas temperature maps in the mid-plane of the simulation box. The initial gas temperature is $T = 100\,\mathrm{K}$.

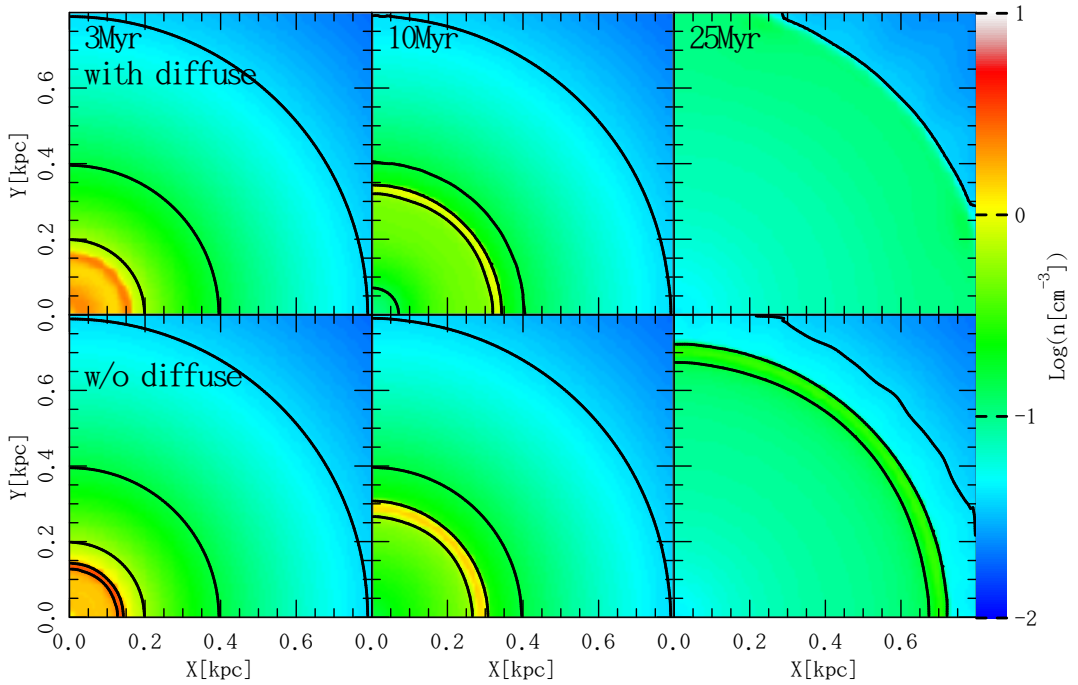

Figure 5.40: Test-6: Same as Figure 5.38 but shows the hydrogen number density maps in the mid-plane of the simulation box.

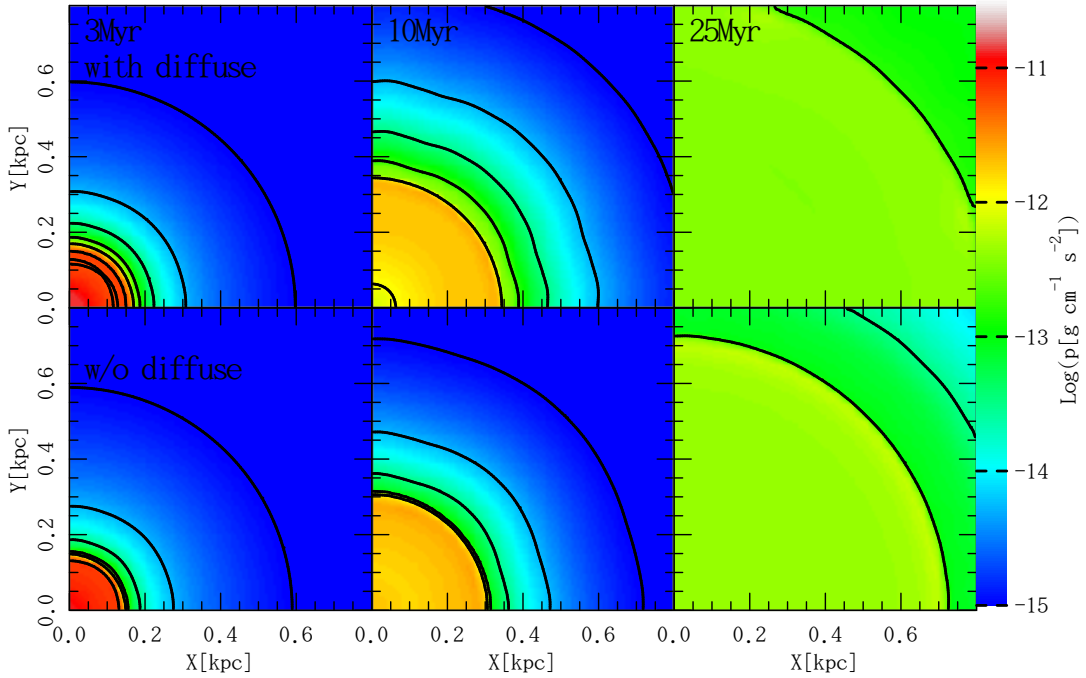

Figure 5.41: Test-6: Same as Figure 5.38 but shows the pressure maps in the mid-plane of the simulation box.

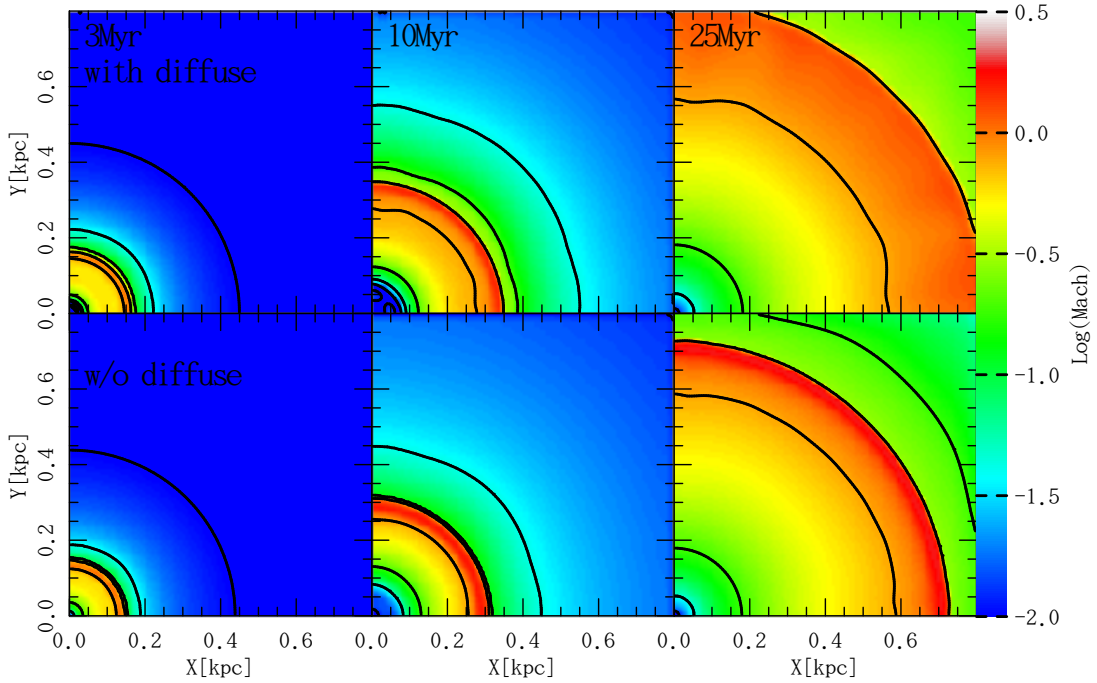

Figure 5.42: Test-6: Same as Figure 5.38 but shows the Mach number maps in the mid-plane of the simulation box.

5.7 Test-7 : HII region expansion in One side incident radiation with the Hydrodynamics

The seventh test is the propagation of a plane-parallel ionization front and its trapping by a dense, uniform, spherical clump with hydrodynamic calculation. We adopt the same initial condition as that of Test-7 in (Iliev et al., 2009). The simulation setting is same as Test-3. In this test, the basic behavior of radiation effect is the same as Test-3. However, the dense core is extended due to number density difference between core and ambient region.

Figures 5.43, 5.44, 5.45, 5.46 and 5.47 show the axis of symmetry through the centre profiles of the ionization fraction of hydrogen, the gas temperature, the hydrogen number density, the gas pressure and Mach number at $t = 1\,\mathrm{Myr}$, $10\,\mathrm{Myr}$ and $50\,\mathrm{Myr}$, respectively. The red-solid and blue-solid lines indicate the results with and without the effect of recombination RT, respectively. The black-dashed lines are the results obtained with RSPH code Susa (2006) and in good agreement with the blue solid lines as expected. Figure 5.49, 5.50, 5.51, 5.52 and 5.53 show the map of the ionization fraction of hydrogen , the gas temperature, the hydrogen number density, the gas pressure and Mach number of the mid-plane in the simulation box, respectively. The upper panels are the result with diffuse photon RT and lower panels are the result without diffuse photon RT, respectively. In the run without diffuse RT, the high number density and fully neutral clump is remind until the $t = 10\,\mathrm{Myr}$ and $t = 50\,\mathrm{Myr}$. This region is not heating by ionization photon, so gas clump is become flow easily state. In the run with diffuse RT, on the other hand, the dense clump is ionized quickly by emitted recombination photons from itself. The incident light-ray erodes behind clump region and that is ionized and heated at $t = 10\,\mathrm{Myr}$. Therefore, the preferentially flow easily direction is eliminated, and the gas clump is extended while almost keeping the spherical shape. In addition, the ionization and heating of behind clump region is promoted by the recombination RT from shadowing edge. The wave shape of boundary of the extended gas clump is caused to the hydrodynamics calculation.

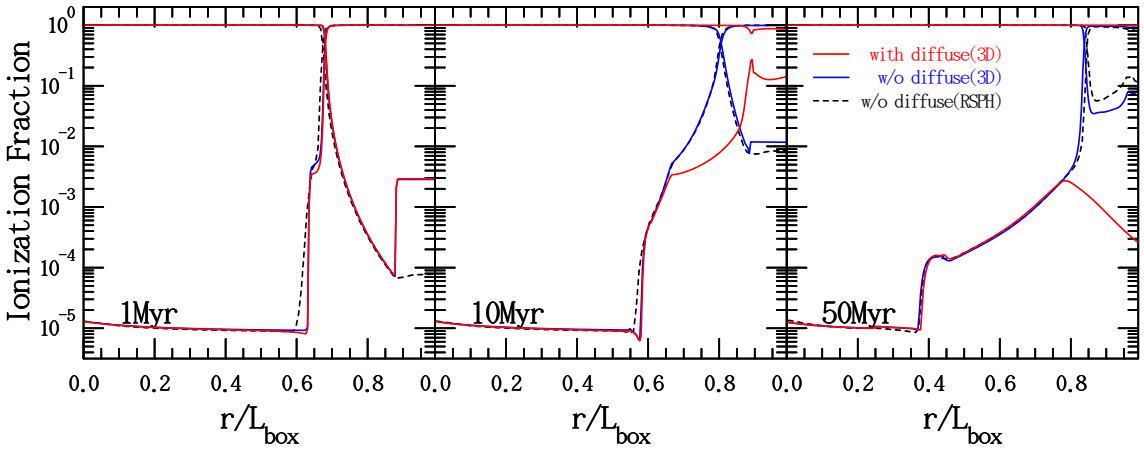

Figure 5.43: Test-7: The axis of symmetry through the centre profiles of ionization fraction at $t = 1\,\mathrm{Myr}$, $10\,\mathrm{Myr}$ and $50\,\mathrm{Myr}$. Red-solid (ARGOT+ART,Case-A) and blue-solid (ARGOT,Case-B) indicate the results with and without the diffuse photon RT, respectively. Black-dashed lines (RSPH,Case-B) are the particle base code without the diffuse photon RT. The horizontal axis is normalized by 6.6 kpc.

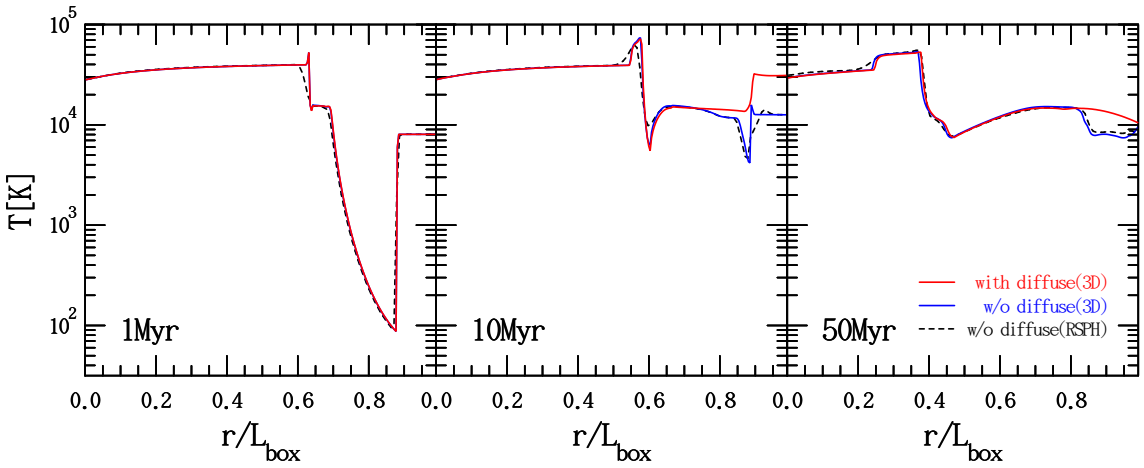

Figure 5.44: Test-7: The axis of symmetry through the centre profiles of the gas temperature. Line colors and type are same as Figure 5.43.

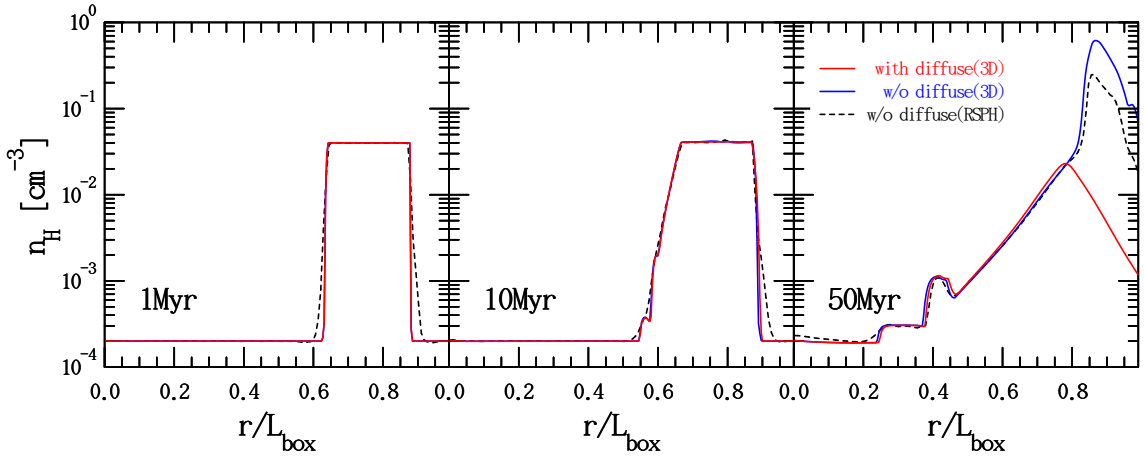

Figure 5.45: Test-7: The axis of symmetry through the centre profiles of the hydrogen number density. Line colors and type are same as Figure 5.43.

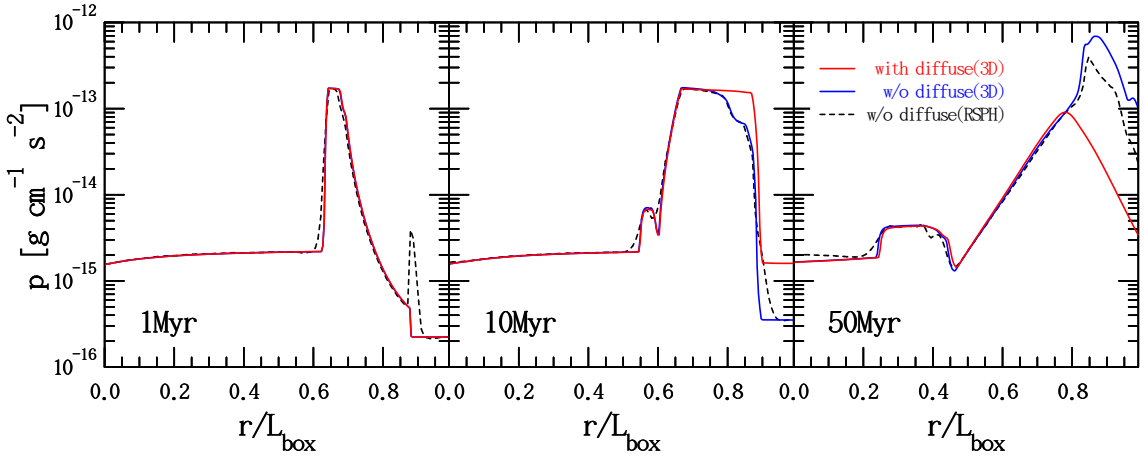

Figure 5.46: Test-7: The axis of symmetry through the centre profiles of pressure. Line colors and type are same as Figure 5.43.

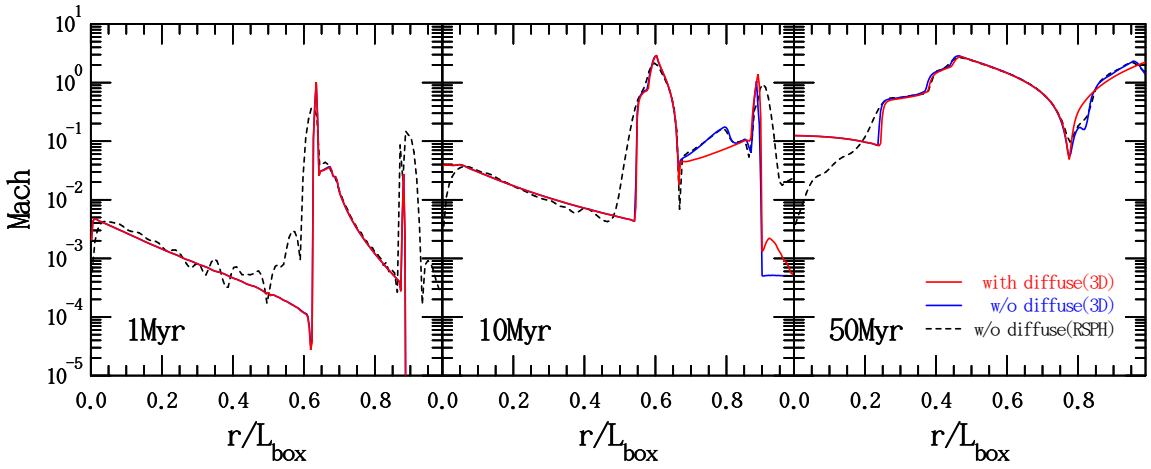

Figure 5.47: Test-7: The axis of symmetry through the centre profiles of Mach number. Line colors and type are same as Figure 5.43.

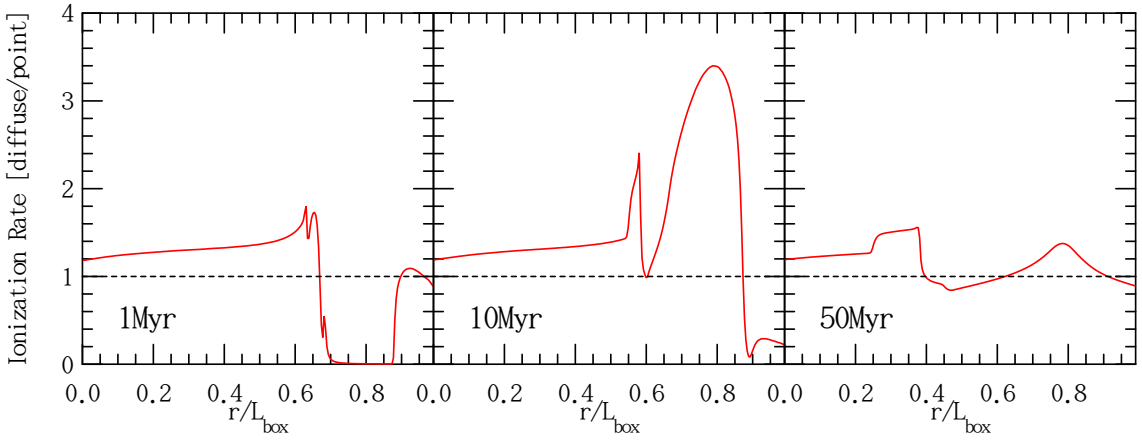

Figure 5.48: Test-7: Profiles of the ratio of the ionization rate by the diffuse and point source RT along the axis of symmetry at $t = 1\,\mathrm{Myr}$, 10 Myr and 50 Myr. The dotted lines indicate the same ratio of Γ by the diffuse and point source RT.

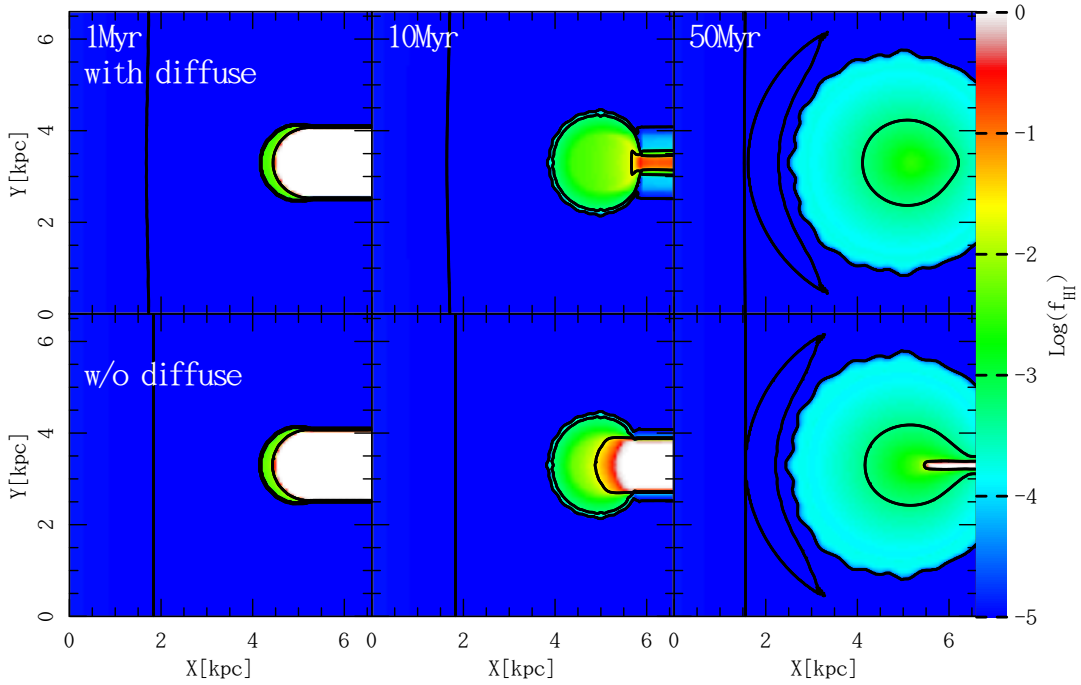

Figure 5.49: Test-7: Maps of neutral fraction of hydrogen in the mid-plane of the simulation box at $t = 1\,\mathrm{Myr}$, $10\,\mathrm{Myr}$ and $50\,\mathrm{Myr}$. The lower and upper panels show the results without and with the diffuse photon RT, respectively. The ambient and clump gas density is $n_H = 2.0\times10^{-4}\,\mathrm{cm}^{-3}$ and $n_c = 0.04\,\mathrm{cm}^{-3}$, respectively.

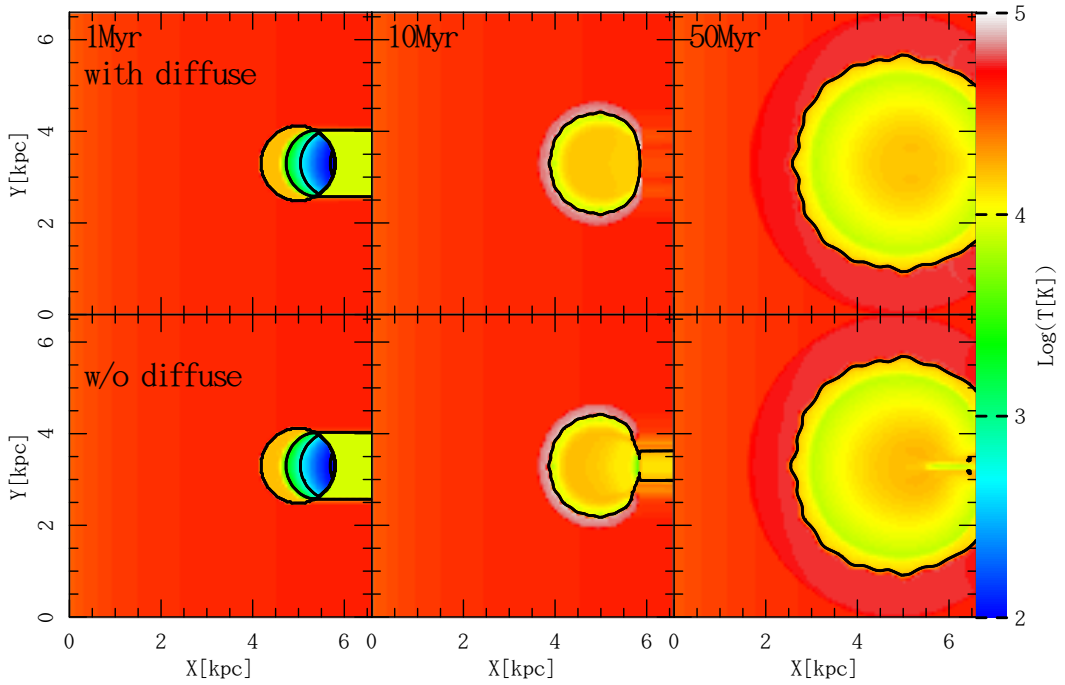

Figure 5.50: Test-7: Same as Figure 5.49 but shows the gas temperature maps in the mid-plane of the simulation box. The initial ambient and clump gas temperature is $T = 8000\,\mathrm{K}$ and $T_c = 40\,\mathrm{K}$, respectively.

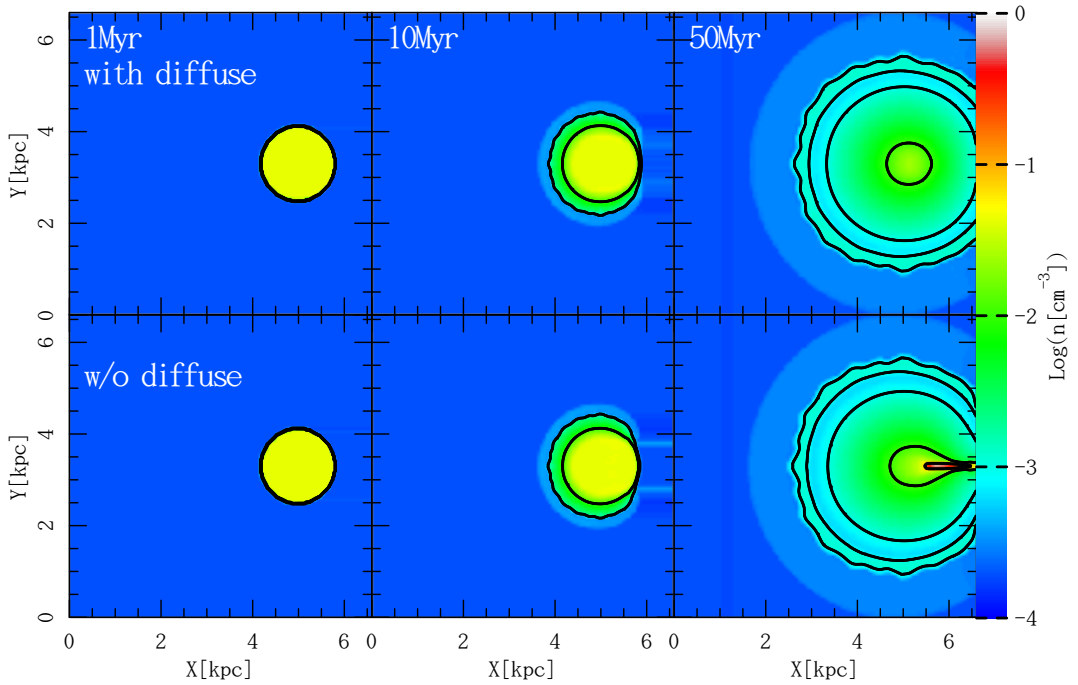

Figure 5.51: Test-7: Same as Figure 5.49 but shows the hydrogen number density maps in the mid-plane of the simulation box.

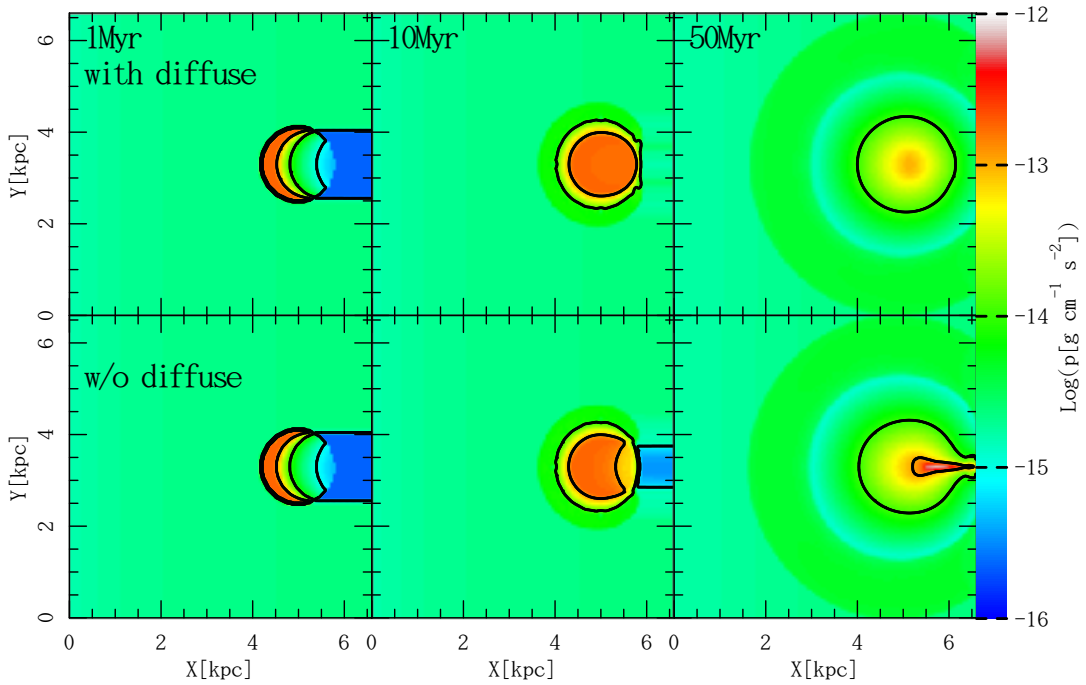

Figure 5.52: Test-7: Same as Figure 5.49 but shows the pressure maps in the mid-plane of the simulation box.

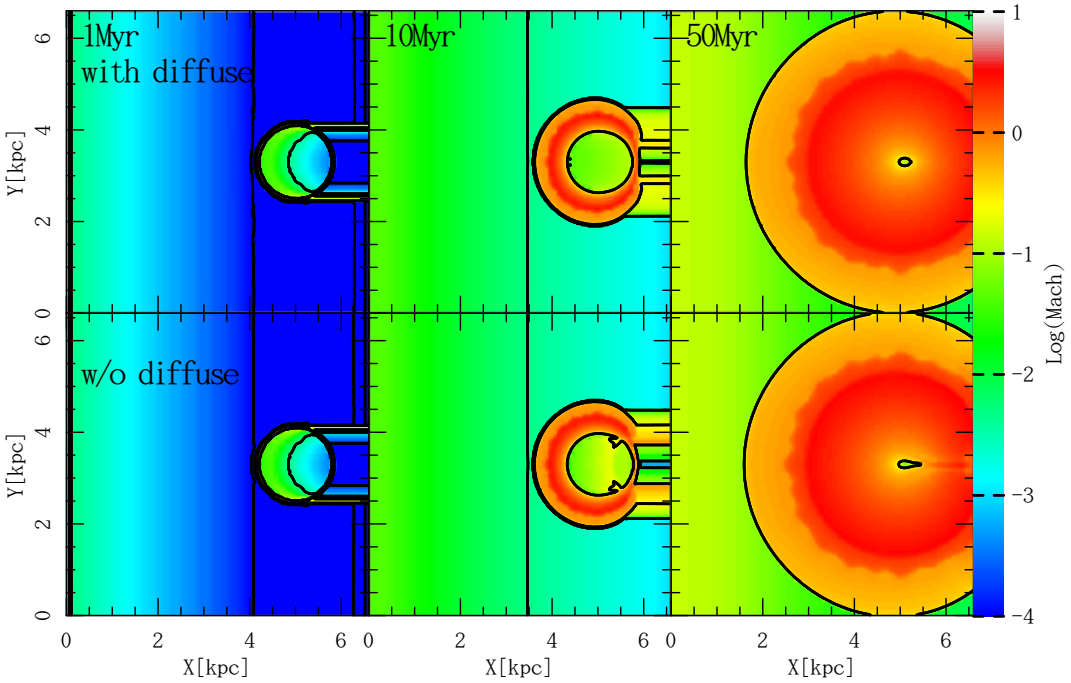

Figure 5.53: Test-7: Same as Figure 5.49 but shows the Mach number maps in the mid-plane of the simulation box.

5.8 Summary

In this chapter, we verify the validity of our RT calculation by comparing the other simulation RT code. The point source RT using on-the-spot approximation by Case-B condition without diffuse RT is proved to be consistent with radiation SPH code by Susa (2006) in Cosmological Radiative Transfer Codes Comparison Project I, II test simulation by Iliev et al. (2006, 2009).

The including diffuse photon RT code not using on-the-spot approximation by Case-A condition is compared by HII region expansion around a point radiating source with effect of recombination radiation computed by our code and the one-dimensional spherical code by Kitayama et al. (2004). We also clarify the condition of the required angular resolution in our RT calculations based on mean free path of the diffuse photons and the mesh spacing.

In generally, the HII expansion with diffuse photon RT calculation is more larger than without diffuse RT due to the recombination photons emitted from the high ionized region around a point sources. The on-the-spot approximation using more RT code is completely ignore the recombination RT if how strongly it's effect. On the other hand, our RT code can be expressed the recombination RT effect. In particular, we show that the recombination RT affects considerably form high dense and high ionized regions. In addition, the diffuse photon erode the shadowing region as behind the dense clump. In Test-3 or Test-7 case, the results with or without diffuse RT vary considerably by this two effect.

In this thesis, we consider diffuse photon as recombination photon. Our RT scheme can extend other continue spectrum transfer as the infrared emission by dust grains of the inter stellar medium. When this implementation, we can calculate the infrared emission form dust grains in a galaxy by three-dimensional ray-tracing radiation transfer simulation.

Chapter 6

Performance

In this chapter, we show the performance of our radiation transfer code. The our radiation transfer calculation code is designed so that it can be run both on Intel multi-core CPUs and GPUs produced by NVIDIA.

6.1 Computing System

The performance is measured on the HA-PACS base-cluster system installed in Center for Computational Sciences, University of Tsukuba. Each computational node of the HA-PACS base-cluster system consists of two sockets of 2.6 GHz Intel Xeon processor E5-2670 with eight cores based on the Sandy-Bridge microarchitecture and four Fermi architecture GPU boards of NVIDIA Tesla M2090 which have 512 CUDA cores and a memory clock is 1.85 GHz, each of which is connected to the CPU sockets through PCI Express Gen2 $\times$ 16 link. Thus, a single computational node provides 2.99 Tflops (0.33 Tflops by CPUs and 2.66 Tflops by GPUs) of computing capability in double precision.

And we use the HA-PACS TCA-cluster for the measurement using Kepler architecture GPUs which is a next generation of Fermi architecture GPU. Each computational node of this system consists of two sockets of 2.6 GHz Intel Xeon processor E5-2670 v2 with ten cores based on the Ivy-Bridge microarchitecture and four Kepler architecture GPU boards of NVIDIA Tesla K20X. NVIDIA Tesla K20X have 2688 CUDA cores and a memory clock is 732 MHz. Thus, a single computational node provides 5.69 Tflops (0.45 Tflops by CPUs and 5.24 Tflops by GPUs) of computing capability in double precision. The TCA-cluster can use a direct GPU communication between other node GPUs. In this thesis, however, we don't use GPU-GPU direct communication. We simply compare the performance of the Fermi and Kepler architecture GPUs. This Kepler architecture GPU has been improved the effective "atomic operations" than Fermi architecture, so it is a very interesting what behaves implementation to eliminate the atomic operation in Seonction 4.1.

We use the `Intel MPI 4.1.3` for compiling CPU code and `CUDA 5.5.22` for compiling GPU code in all measured performance.

6.2 Performance of Implementation GPUs with a Single Node

The upper panel of Figure 6.1 shows wallclock time for a iteration of the diffuse RT calculation on a single node with various numbers of CPU cores and the Fermi architecture GPU boards. The wallclock times are measured for $N_{\rm m} = 64^3$, 128^3 and 256^3. The angular resolution parameter $N_{\rm side}$ is set to $N_{\rm side} = N_{\rm m}^{1/3}/16$ so that $N_{\rm side}\Delta H$ is kept constant. Note that the wallclock times are nearly proportional to $N_{\rm m}^{5/3}$ as theoretically expected. The lower panel of Figure 6.1 shows the performance gain of the diffuse RT calculation with multiple CPU cores and GPU boards relative to the performance with a single CPU core and a single GPU board, respectively. Use of the multiple CPU cores and multiple GPU boards provides the efficient performance gains nearly proportional to the adopted numbers of CPU cores and GPU boards for $N_{\rm m} = 128^3$ and 256^3 except for the fact that those with 16 CPU cores (2 CPU sockets) is not very impressive even for $N_{\rm m} = 256^3$ because of the relatively slow memory access across the CPU sockets. On the other hand, the performance gain for $N_{\rm m} = 64^3$ is somewhat degraded because of the overheads for invoking the multiple threads and communication overhead for data exchange between CPUs and GPUs.

Figure 6.2 shows the performance gain of the diffuse RT calculation on a single node with various number of GPU boards relative to the performance with 16 CPU cores. Use of the multiple GPU boards provides the efficient performance gains nearly proportional to the adopted numbers of GPU boards for all number of mesh grids. The performance gain is nearly three times with a single GPU board and 12 times with four GPU boards in comparison with 16 CPU cores for $N_{\rm m} = 256^3$. However, the performance gains decreases with multiple GPU boards when the number of mesh grids is small for $N_{\rm m} = 64^3$. This is because the communication overhead between CPUs and GPUs is larger than the operation time of diffuse RT calculation on GPUs.

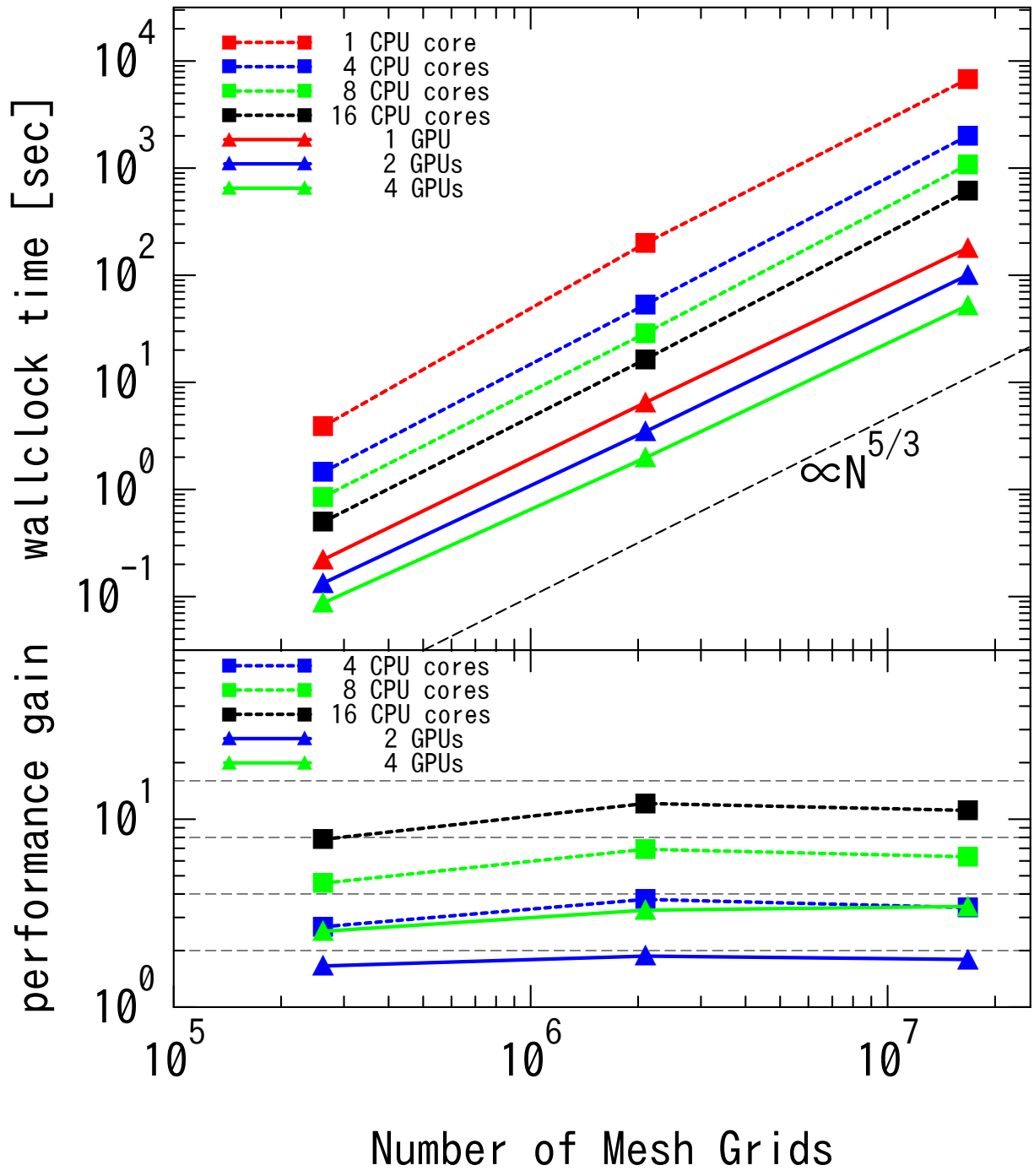

Figure 6.1: Wallclock times of diffuse RT calculation with various numbers of CPU cores and GPU boards for $N_{\rm m} = 64^3$, 128^3 and 256^3 are shown in the upper panel. A dotted line indicate the dependence of computational cost on a number of mesh grids, $\propto N_{\rm m}^{5/3}$. In the lower panel, we present the performance gains of diffuse RT calculation with multiple CPU cores and GPU boards relative to the performance with a single CPU core and GPU board, respectively. Horizontal dotted lines indicates the performance gains of 2, 4, 8 and 16 from bottom to top.

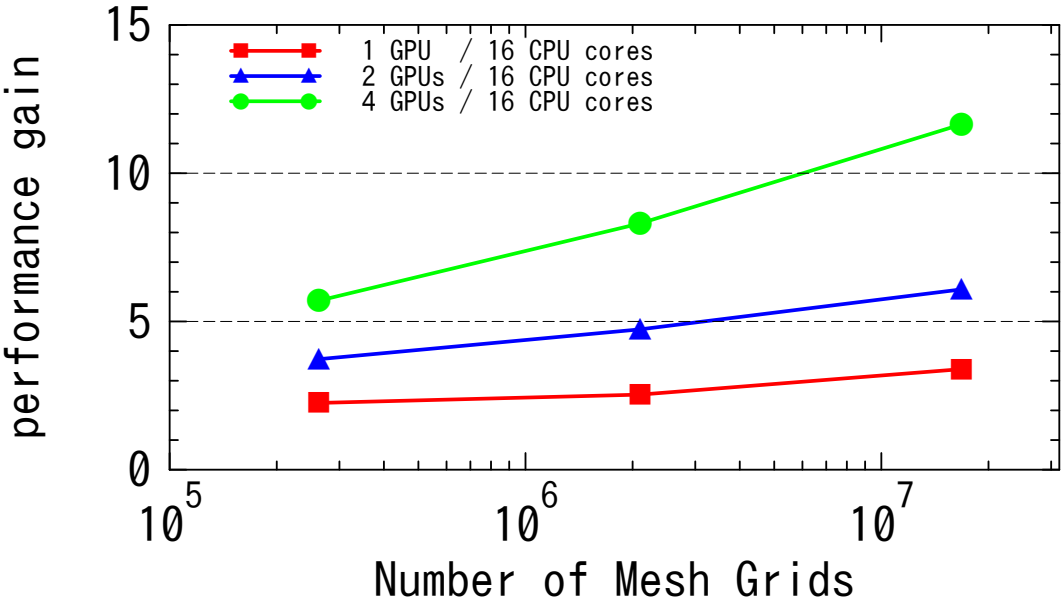

Figure 6.2: Performance gain of diffuse RT calculation of one, two and four GPU boards respect to 16 CPU cores for $N_{\rm m} = 64^3$, 128^3 and 256^3 on a single node.

6.3 Performance of Using the Atomic Operation and Optimized Number of Threads Per a Block

Figure 6.1 is calculated by Fermi architecture GPUs with 8 threads per a block in `CUDA`. This thread number is less than the warp size as 32 threads per a block. In generally, when the number of threads is less than the warp size, several cuda cores do not work, therefore, the computational efficiency decreases. However the diffuse RT calculation has some conditional branch, in this case, the computational efficiency may deteriorate in order to follow the wrong branch in a warp unit. If the number of working cores is less than a warp size, it is expected that the probability to follow the wrong branch decrease. We verify the most better number of threads per a block for diffuse RT calculation. Figure 6.3 shows wallclock time for a iteration of the diffuse RT calculation on a single node with four GPU boards of Fermi architecture and various numbers of mesh grid and with and without atomic operations. The wallclock times are measured for the number of threads 1 – 512. Here, each $N_{\mathrm{side}}\Delta H$ are constant. First, we verify the relationship of using atomic operations. The wallclock times without atomic operations are better than the times with atomic operations in any number of mesh grids. Therefore, the calculation of diffuse RT is possible to improve the computational efficiency by removing the atomic operations. It is successful in 3 times better by removing the atomic operations in the same number of threads. Next, we consider relations of the number of threads per a block without atomic operations case. It shows that a performance on a single node is best when the number of threads is 8, 16, 8 for $N_{\mathrm{m}} = 64^3$, $N_{\mathrm{m}} = 128^3$ and $N_{\mathrm{m}} = 256^3$, respectively. Thus, the computational efficiency increases because the impact of reducing the conditional branch by limiting working CUDA cores less than the warp size can surpass to the overhead of unnecessary conditional branch in the diffuse RT calculation.

In Fermi architecture GPUs, it is possible to improve the computational efficiency by removing the atomic operations and optimized number of threads per a block. Next, we verify the Kepler architecture GPUs which seems has been greatly improved of the atomic operations. Figure 6.4 is same as Figure 6.3 but used Kepler architecture GPUs. As a result, the optimized number of threads per a block works effectively as well as Fermi architecture GPUs, and the threads of performance peaks are 64, 8 and 16 in $N_{\mathrm{m}} = 64^3$, 128^3 and 256^3, respectively. Compared to Fermi architecture GPUs, A degree of degradation is a little when the number of threads per a block is increased than a warp size. In addition, the relationship of using atomic operations is reversed. The computational efficiency without atomic operation deteriorate in regardless of the number of mesh grids. Probably, Kepler architecture GPU can use effectively a L1 cache or shared memory contained in each block for atomic operations and it is very complex to program by oneself. The performance gain with atomic operation is nearly 1.9 times for the removing atomic operations.

Consequently, it is necessary to use the atomic operations properly in GPU architecture of using system. The implementation of removing atomic operations is effective in the poor system of the atomic operations. The many-core processors appeared in recent years is not necessarily to have been optimized, so this implementation can be used to such cases. For number of threads suitable for calculation, there is an optimum number by the GPU architecture or calculation per a node. It will not exceed the size of the warp for this calculation of diffuse RT.

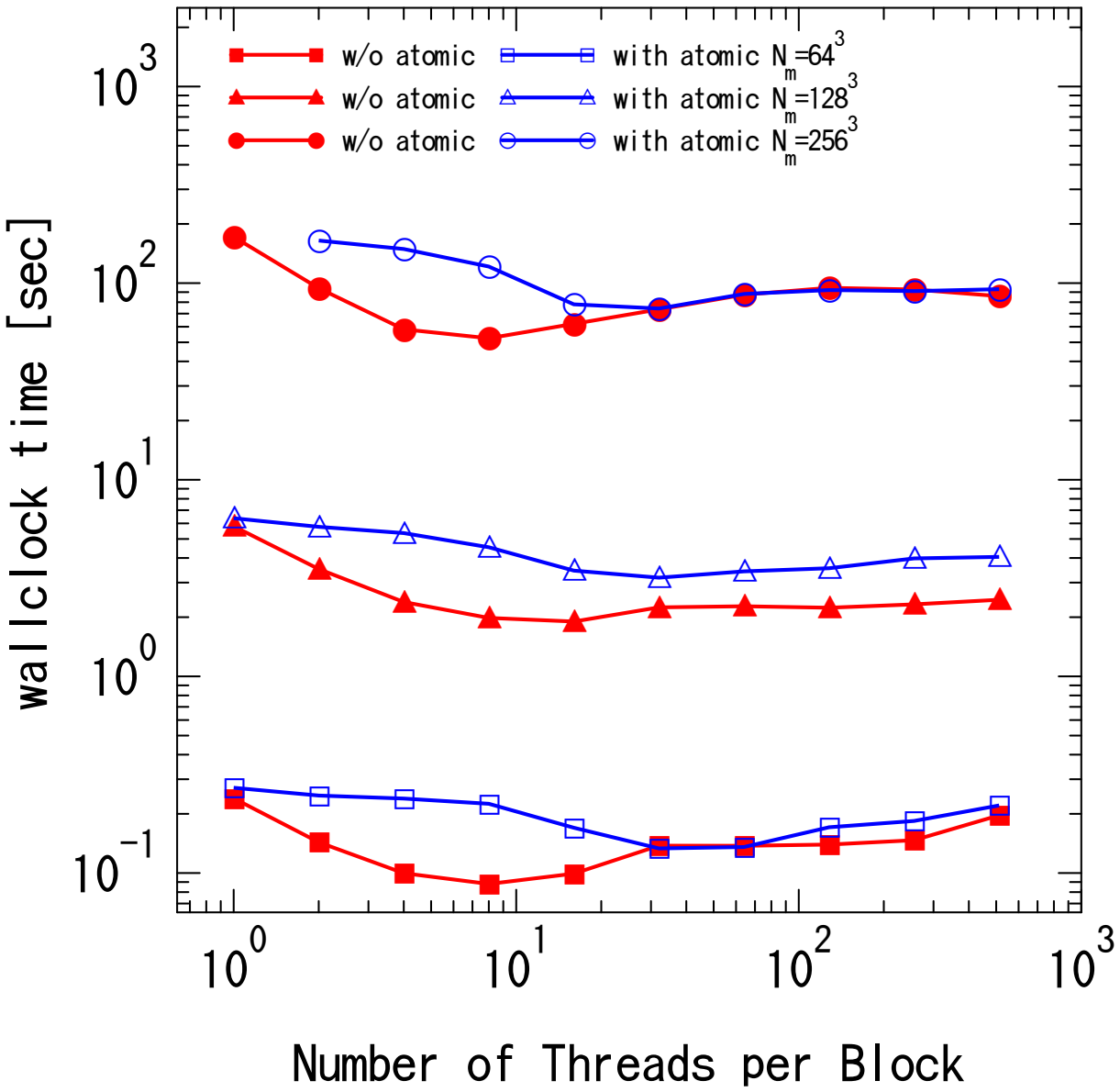

Figure 6.3: Wallclock time of the diffuse RT calculation with four Fermi architecture GPUs for the threads of number per a block. Red line is the calculation without atomic operation and Blue line is with the atomic operations. The symbole of square, triangle and circle are $N_{\rm m} = 64^3$, 128^3 and 256^3.

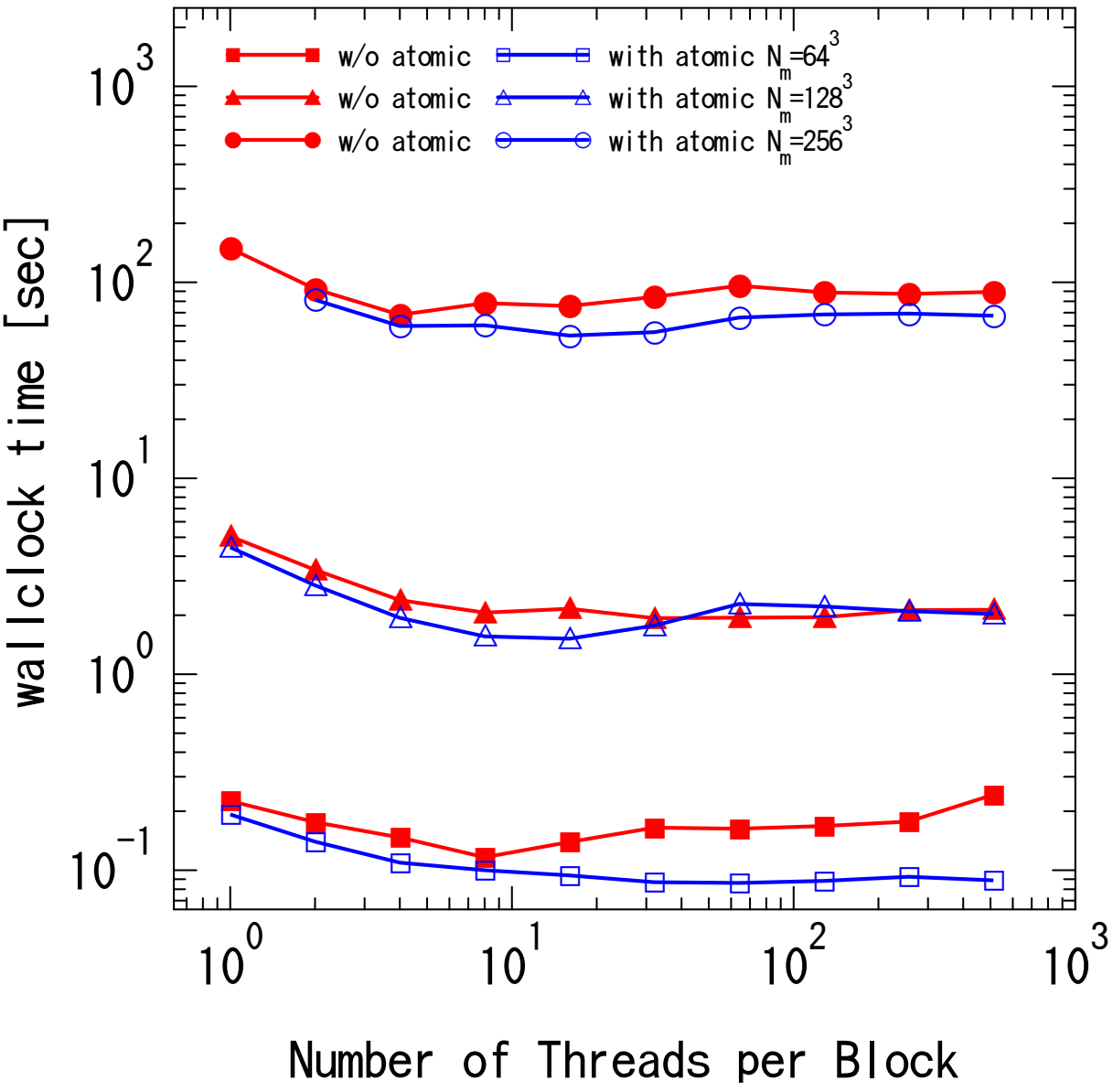

Figure 6.4: The same of 6.3 but use four Kepler architecture GPUs.

6.4 Performance of Implementation GPUs with Multiple Node

The upper panel of Figure 6.5 shows the wallclock time of diffuse RT calculation performed on a single and multiple computational nodes with and without Fermi architecture GPU boards, where we invoke one MPI process on each computational node. In the runs without GPUs, each MPI process invokes 16 `OpenMP` threads, while in the runs with GPUs, we utilize four GPU boards on each computational node. We measure the wallclock time consumed for a single iteration of diffuse RT calculation for 64^3–1024^3 mesh grids on 1–64 computational nodes. The lower panel depicts the performance gain of the runs with 8 and 64 computational nodes relative to those with 1 and 8 computational nodes, respectively, where the ideal performance gain of 2, 4 and 8 is shown by a dotted line. As for the runs without the use of GPUs, the parallel efficiency is reasonable when $N_{\rm m}/N_{\rm node} \geq 64^3$, where $N_{\rm node}$ is the number of computational nodes in use. For a given number of computational nodes, the runs with the use of GPUs have poorer performance gains than those without the use of GPUs mainly due to the communication overhead between CPUs and GPUs. Such communication overhead is, however, proportional to the number of light-rays getting through the surface of the decomposed computational domains, $\propto N_{\rm m}^{2/3}$ and has weaker dependence on the number of mesh grids than the computational costs, $\propto N_{\rm m}^{5/3}$. Therefore, it can be easily concealed for a sufficient number of mesh grids, and we have good parallel efficiency for $N_{\rm m}/N_{\rm node} \geq 128^3$.

Figure 6.6 shows the performance gain of the diffuse RT calculation on various number of nodes with four GPU boards per a node relative to the performance with 16 CPU cores per a node. Use of the GPUs provides the efficient performance gains nearly 10 times better than the run without GPUs for $N_{\rm m}/N_{\rm node} \geq 256^3$. The number of mesh grids of a node is also the same, the MPI communication overhead is increased when the number of nodes is large. Figure 6.7 shows the fraction of MPI communication time in 8 and 64 nodes. When the number of mesh grids is small, the MPI communication time is larger than the operation time. On the other hand, the number of mesh grids is larger, the majority is operation time in each nodes. However, the fraction of MPI communication time is more than 20% in 8 nodes and more than 40% in 64 nodes. And the diffuse photon calculation with GPUs has the communication between CPUs and GPUs for MPI communication. The communications of CPUs to GPUs and GPUs to CPUs appear each time of MPI communications. If our RT code is used the GPUs direct communication between each nodes, the performance is possibly improved because the overhead of communication between CPUs and GPUs for MPI communication is considerably larger.

Finally, we discuss the total calculation time of a point source RT and diffuse RT. Figure 6.8 shows the wallclock time and the performance gain of the total calculation performed of diffuse and point source RT with a point source on a single and multiple computational nodes with and without Fermi architecture GPU boards. The dashed line indicates an analytic scaling of computational cost for the RT calculation of diffuse RT, $\propto N_{\rm m}^{5/3}$ and point source in fixed the number of point source, $\propto N_{\rm m}^{4/3}$. In this case, the wallclock time of diffuse RT is nearly three times larger than the computation wallclock time point source RT. Therefore, the total wallclock time is the same trend as the wallclock time of diffuse RT. The run with GPUs can be in accelerated nearly 10 times faster than the run without GPUs for large number of mesh grids $N_{\rm m} \geq 512$.

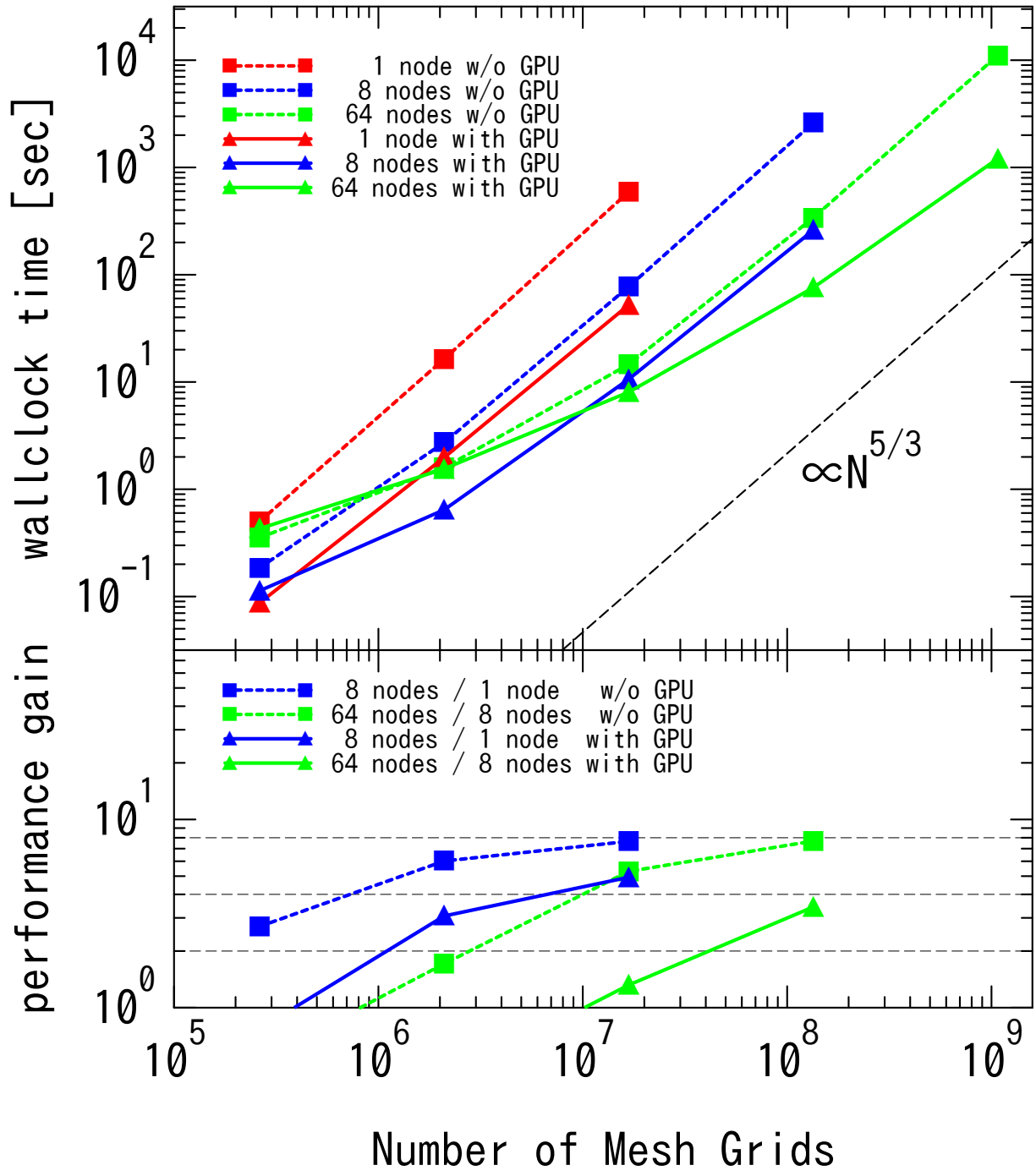

Figure 6.5: Wallclock times for diffuse RT calculation with various number of mesh grids computed with 1, 8 and 64 nodes are shown in the upper panel. The results with and without the use of four GPU boards are depicted. The dashed line indicates an analytic scaling of computational cost for the RT calculation of diffuse RT, $N_{\rm m}^{5/3}$. In the lower panel, we present the performance gains of diffuse RT calculation with multiple nodes 16 CPU cores and four GPU boards relative to the performance with a single node 16 CPU cores and four GPU boards, respectively. Horizontal dotted lines indicates the performance gains of 2, 4 and 8 from bottom to top.

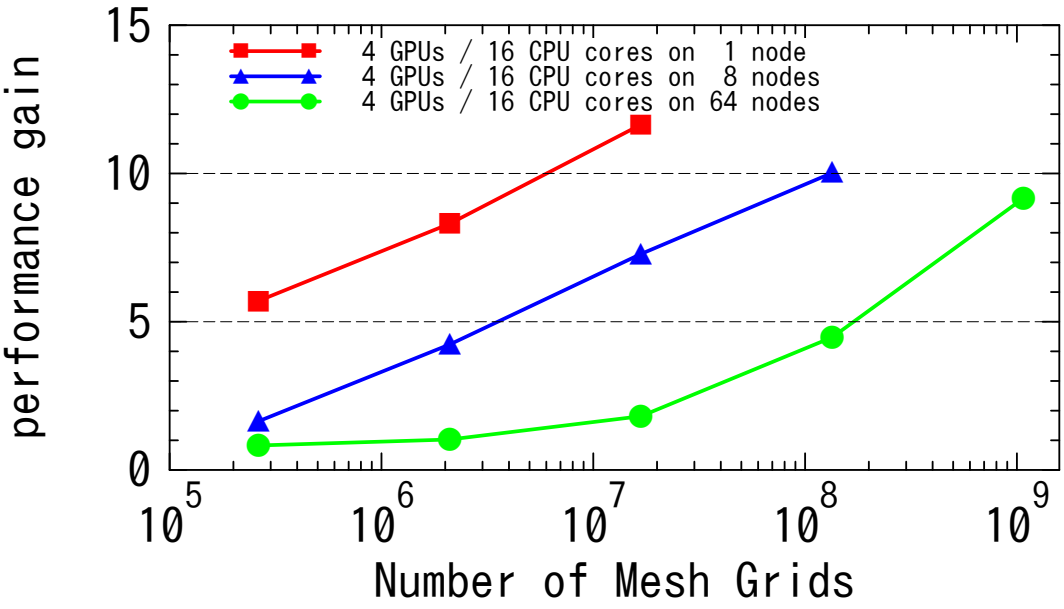

Figure 6.6: Performance gain of diffuse RT calculation of four GPU boards in one, 8 and 64 nodes respect to 16 CPU cores in same number of nodes for $N_{\rm m} = 64^3$, 128^3, 256^3, 512^3 and 1024^3.

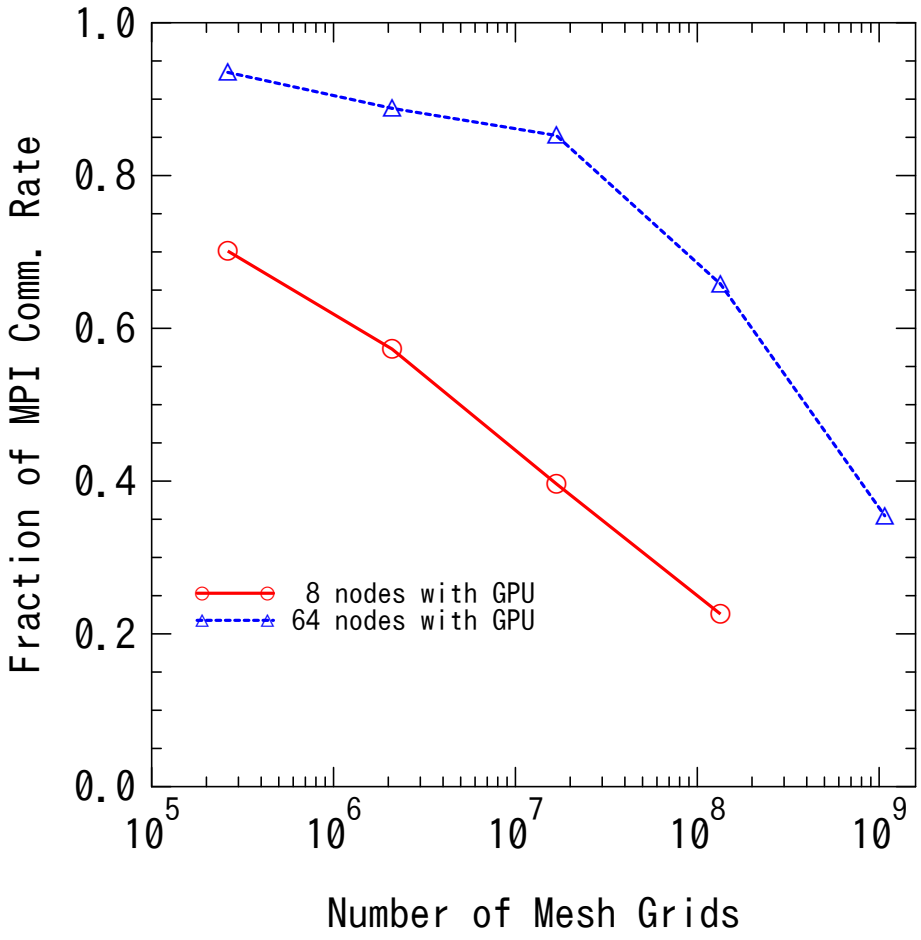

Figure 6.7: Fractions of wallclock times for MPI communication relative to total wallclock time elapsed in the calculations of diffuse radiation transfer.

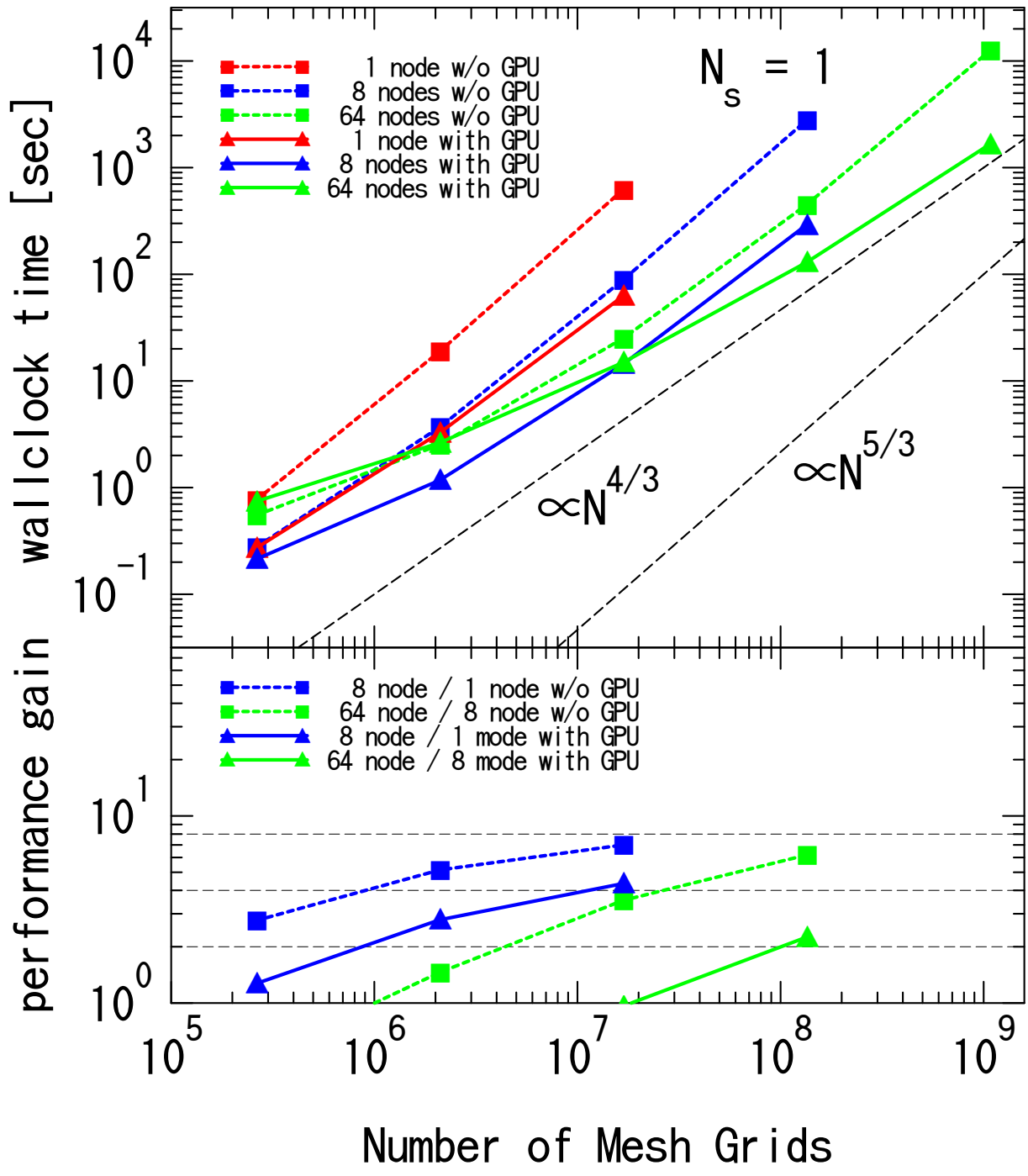

Figure 6.8: Wallclock times for total of diffuse and point source RT calculation with various number of mesh grids computed on 1, 8 and 64 nodes with one point source are shown in the upper panel. The dashed line indicates an analytic scaling of computational cost for the RT calculation of diffuse RT, $N_{\rm m}^{5/3}$ and point source in fixed number of source, $N_{\rm m}^{4/3}$.

6.5 Summary

In this chapter, we present a new implementation of the RT calculation of point sources and diffuse radiation field on three-dimensional mesh grids, which is suitable to be run on recent processors with highly-parallel architecture such as multi-core CPUs and GPUs. The code is designed to be run on both of ordinary multi-core CPUs and GPUs produced by NVIDIA by utilizing the `OpenMP` application programming interface and the `CUDA` programming platform, respectively.

Since our RT calculation is based on the ray-tracing scheme, the RT calculation itself can be carried out concurrently by assigning the RT calculation along each light-ray to individual software threads. To avoid the atomic operations in computing the averaged intensity (equation (2.11)) which can potentially degrade the efficiency of the thread parallelization, we devise a new scheme of the RT calculations in which a set of parallel light-rays are split into 4 groups so that parallel light-rays in each group do not get through any mesh grids more than once. As well as the thread parallelization inside processors or computational nodes, we also parallelize our code on a multi-node system using the MWF scheme developed by Nakamoto et al. (2001).

We show good parallel efficiency of our implementation for intra- and inter-node parallelizations. As for the intra-node parallelization, the performance scales well with the number of CPU cores and GPU boards in use, except for the one in the case that multiple CPU sockets are used as a single shared-memory system. The scalability of the inter-node parallelization with the MWF scheme is also measured for 64^3 to 1024^3 mesh grids on up to 64 computational nodes and it is found that the inter-node parallelization is efficient when we have a sufficient number of mesh grids per node, $N_{\rm m}/N_{\rm node} \geq 128^3$ and $N_{\rm m}/N_{\rm node} \geq 64^3$ for the runs with and without GPUs, respectively. The ray-grouping technique described in 4.1 is effective and significantly improves the performance of our RT calculations by a factor of more than two, on Fermi architecture GPUs (NVIDIA Tesla M2090). However, Kepler architecture GPUs (NVIDIA Tesla K20X) is a good result of using the atomic operations in the diffuse RT calculation. This reason that the atomic operation of Kepler architecture GPU probably uses full advantage of the quickly access memory as L1 cache or shared memory in unit of a block.

With our implementation presented in this thesis, we are able to perform the diffuse RT calculations in a reasonable wallclock time comparable to that of other physical processes such as hydrodynamical calculations. This means that the diffuse RT calculations can be coupled with hydrodynamic simulations and we are able to conduct radiation hydrodynamical simulations with the effect of diffuse radiation transfer as well as the radiation transfer from point radiating sources in three-dimensional mesh grids.

It should be noted that, though we present the implementations and the performance on the multi-core CPUs and GPUs produced by NVIDIA, our approaches presented in this thesis can be readily applied to other processors with similar architecture, such as the Intel Xeon-Phi processor or GPUs by other vendors. In addition, our approach can be easily extended to adaptively refined mesh grids using the prescription described in Razoumov & Cardall (2005), although we present the implementation for uniform mesh grids in this thesis.

Acknowledgments

I am particularly grateful to my supervisor Kohji Yoshikawa for useful discussion, valuable physical advice, various numerical simulations advice, and strong supports throughout my doctoral program in physics during the last five years. I have greatly benefited from collaborators Takashi Okamoto and Kenji Hasegawa for valuable discussion and improving my work and I would like to express my best gratitude to them. I have had the support and encouragement of Masayuki Umemura, Masao Mori, Nozomu Kawakatsu, Toshihiro Kawaguchi, Ataru Tanikawa, Alexander Y. Wagner, Daisuke Namekata for valuable discussion, improving my work and providing excellent materials. I am very grateful to Yohei Miki, Go Ogiya for advice of the physical and the numerical simulation techniques. Special thanks also to Yu Komatsu and other present and/or past members of astrophysics division. I am very thankful to Masayuki Umemura, Masao Mori, Naohito Nakasato, and Kohji Yoshikawa for their constructive comments that have improved my study and doctoral thesis.

The numerical simulations were performed on HA-PACS system and COMA system, at the Center for Computational Sciences, University of Tsukuba. I am grateful to the HA-PACS and COMA project team for their generous technical assistance. A part of analysis was performed on the gorilla, andromeda, mw and Hexa cluster at Theoretical Astrophysics Group of University of Tsukuba.

Bibliography

[1] Abel, T., Anninos, P., Zhang, Y., & Norman, M. L. 1997, New Astronomy, 2, 181

[2] Abel, T., Norman, M. L., & Madau, P. 1999, The Astrophysical Journal, 523, 66

[3] Anninos, P., Zhang, Y., Abel, T., & Norman, M. L. 1997, New Astronomy, 2, 209

[4] Cen, R. 1992, The Astrophysical Journal Supplement Series, 78, 341

[5] Ciardi, B., Ferrara, A., Marri, S., & Raimondo, G. 2001, Monthly Notices of the Royal Astronomical Society, 324, 381

[6] Dopita, M. A., Krauss, L. M., Sutherland, R. S., Kobayashi, C., & Lineweaver, C. H. 2011, Astrophysics and Space Science, 335, 345

[7] Gnedin, N. Y., & Abel, T. 2001, New Astronomy, 6, 437

[8] González, M., Audit, E., & Huynh, P. 2007, Astronomy and Astrophysics, 464, 429

[9] Gorski, K. M., Hivon, E., Banday, A., et al. 2005, The Astrophysical Journal, 622, 759

[10] Hasegawa, K., & Umemura, M. 2010, Monthly Notices of the Royal Astronomical Society, 407, 2632

[11] Hui, L., & Gnedin, N. Y. 1997, Monthly Notices of the Royal Astronomical Society, 292, 27

[12] Hummer, D. 1994, Monthly Notices of the Royal Astronomical Society, 268, 109

[13] Hummer, D., & Storey, P. 1998, Monthly Notices of the Royal Astronomical Society, 297, 1073

[14] Ikeuchi, S., & Ostriker, J. P. 1986, The Astrophysical Journal, 301, 522

[15] Iliev, I. T., Ciardi, B., Alvarez, M. A., et al. 2006, Monthly Notices of the Royal Astronomical Society, 371, 1057

[16] Iliev, I. T., Whalen, D., Mellema, G., et al. 2009, Monthly Notices of the Royal Astronomical Society, 400, 1283

[17] Inoue, A. K. 2010, Monthly Notices of the Royal Astronomical Society, 401, 1325

[18] Janev, R., Langer, W., Evans Jr, K., & Post Jr, D. 1988, Nuclear Fusion, 28, 529

[19] Kahn, F. 1954, Bulletin of the Astronomical Institutes of the Netherlands, 12, 187

[20] Kitayama, T., Yoshida, N., Susa, H., & Umemura, M. 2004, The Astrophysical Journal, 613, 631

[21] Kunasz, P., & Auer, L. H. 1988, Journal of Quantitative Spectroscopy and Radiative Transfer, 39, 67

[22] Liou, M.-S. 1996, Journal of computational Physics, 129, 364

[23] Maselli, A., Ferrara, A., & Ciardi, B. 2003, Monthly Notices of the Royal Astronomical Society, 345, 379

[24] Mellema, G., Iliev, I. T., Alvarez, M. A., & Shapiro, P. R. 2006, New Astronomy, 11, 374

[25] Miralda-Escudé, J. 2003, The Astrophysical Journal, 597, 66

[26] Nakamoto, T., Umemura, M., & Susa, H. 2001, Monthly Notices of the Royal Astronomical Society, 321, 593

[27] Okamoto, T., Yoshikawa, K., & Umemura, M. 2012, Monthly Notices of the Royal Astronomical Society, 419, 2855

[28] Osterbrock, D. 2006, Ferland 2006,‘ Astrophysics of Gaseous Nebulae and Active Galactic Nuclei, ’ (University Science Books)

[29] Pawlik, A. H., & Schaye, J. 2011, Monthly Notices of the Royal Astronomical Society, 412, 1943

[30] Rahmati, A., Pawlik, A. H., Raičevic, M., & Schaye, J. 2013a, Monthly Notices of the Royal Astronomical Society, 430, 2427

[31] Rahmati, A., Schaye, J., Pawlik, A. H., & Raičevic, M. 2013b, Monthly Notices of the Royal Astronomical Society, 431, 2261

[32] Razoumov, A., & Cardall, C. 2005, Monthly Notices of the Royal Astronomical Society, 362, 1413

[33] Rijkhorst, E.-J., Plewa, T., Dubey, A., & Mellema, G. 2006, Astronomy & Astrophysics, 452, 907

[34] Ryu, D., Ostriker, J. P., Kang, H., & Cen, R. 1993, The Astrophysical Journal, 414, 1

[35] Sokasian, A., Abel, T., & Hernquist, L. E. 2001, New Astronomy, 6, 359

[36] Stone, J. M., Mihalas, D., & Norman, M. L. 1992, The Astrophysical Journal Supplement Series, 80, 819

[37] Susa, H. 2006, Publications of the Astronomical Society of Japan, 58, 445

[38] Van Leer, B. 1979, Journal of computational Physics, 32, 101

[39] Wise, J. H., & Abel, T. 2011, Monthly Notices of the Royal Astronomical Society, 414, 3458

[40] Wyithe, J. S. B., Mould, J., & Loeb, A. 2011, The Astrophysical Journal, 743, 173

[41] Yoshikawa, K., & Sasaki, S. 2006, Publications of the Astronomical Society of Japan, 58, 641